

NASA Contractor Report 4329

1N-02

1633

P135

**Unified Aeroacoustics Analysis
for High Speed Turboprop
Aerodynamics and Noise**

*Volume I—Development of Theory for
Blade Loading, Wakes, and Noise*

D. B. Hanson

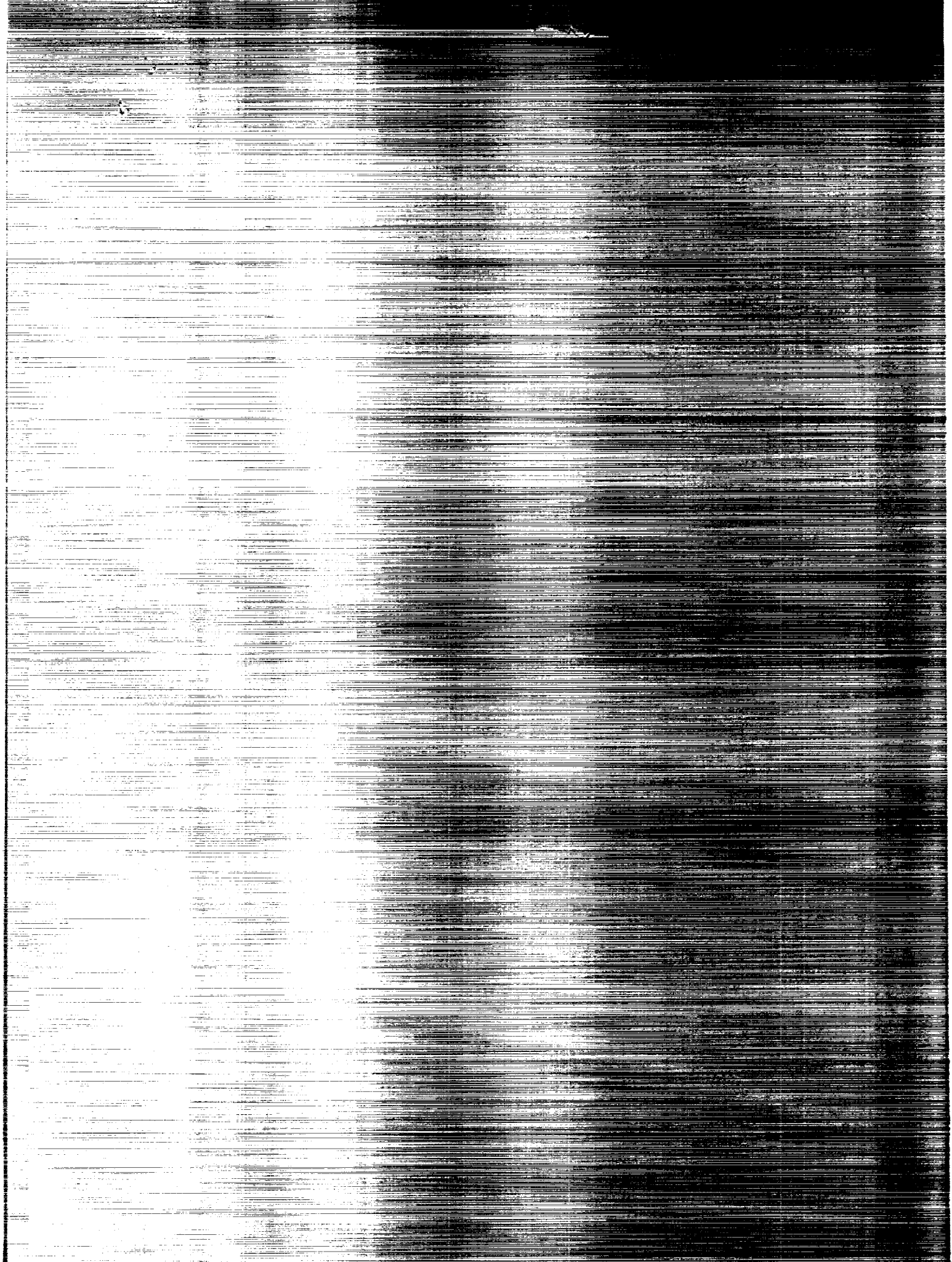
CONTRACT NAS3-23720

MARCH 1991

(NASA-CR-4329) UNIFIED AEROACOUSTICS
ANALYSIS FOR HIGH SPEED TURBOPROP
AERODYNAMICS AND NOISE. VOLUME 1:
DEVELOPMENT OF THEORY FOR BLADE LOADING,
WAKES, AND NOISE Final Report (Hamilton

NP1-19049

Unclas
H1/02 0001633



NASA Contractor Report 4329

Unified Aeroacoustics Analysis for High Speed Turboprop Aerodynamics and Noise

*Volume I—Development of Theory for
Blade Loading, Wakes, and Noise*

D. B. Hanson
*United Technologies Corporation
Hamilton Standard Division
Windsor Locks, Connecticut*

Prepared for
Lewis Research Center
under Contract NAS3-23720



National Aeronautics and
Space Administration
Office of Management
Scientific and Technical
Information Division

1991

TABLE OF CONTENTS

<u>Section No.</u>	<u>Page No.</u>
SUMMARY	1
1.0 INTRODUCTION	2
2.0 BACKGROUND	4
3.0 GENERAL PRESSURE THEORY	7
Differential Equation.....	7
Source Representation	8
Integration of Source Function	11
Normalizations	13
Multiple Blades and Interblade Phase Angle	16
Sum Over Loading Harmonics	18
4.0 NEAR FIELD NOISE PREDICTION FORMULAS	24
Thickness and Steady Non-radial loading	24
Radial Loading - Steady and Unsteady	25
Unsteady Loading - Non-radial	25
General Counter-Rotation Case	26
Special Case-Equal Blade Numbers and Equal RPMs	27
Special Case-Guide Vanes or Other Fixed Inflow Distortion ...	28
5.0 FAR FIELD NOISE PREDICTION FORMULAS	29
Stationary Phase Integral	29
Thickness and Steady Non-radial Loading	33
Radial Loading - Steady and Unsteady	34
Unsteady Loading - Non-radial	36
General Counter-Rotation Case	36
Special Case-Equal Blade Numbers and Equal RPMs	37
Special Case-Guide Vanes or Other Fixed Inflow Distortion ...	38
6.0 SOUND POWER AND WAVE DRAG	39
7.0 DOWNWASH EQUATIONS FOR AIRLOAD CALCULATIONS	45
Acceleration Potential Method	45
Velocity Potential	47
Downwash Velocity	49
Wake and Bound Components of Kernel Function	50
Approach of Field Point to the Vortex Sheets	52
Integral of Body Force Term in Momentum Equation	56
8.0 RELATIONSHIP BETWEEN LIFTING SURFACE THEORY AND CLASSICAL PROPELLER MOMENTUM THEORY	59
Mean Induction for "Thick" Rotor	59
Actuator Disc Results	62
Sample Calculations	64
Comparison with Propeller Momentum Theory and Effect of Non-linearity	65

11 INTENTIONALLY BLANK

PRECEDING PAGE BLANK NOT FILMED

9.0	DISCRETIZATION OF INTEGRAL EQUATION	67
	General Form of Inversion Method	67
	Inversion of Propeller Integral Equation	68
	Comments on Evaluation of Kernel Function	72
10.0	BOUNDARY CONDITIONS AND INVERSION OF INTEGRAL EQUATION	75
	Boundary Conditions	75
	Induction Caused by Blade Thickness	77
11.0	AERODYNAMIC PERFORMANCE	78
	Force Resolution	78
	Vortex Drag	79
	Performance Calculation	81
12.0	FORMULAS FOR WAKE PREDICTIONS	83
13.0	STUDIES WITH 3D LIFT RESPONSE THEORY	85
14.0	CONCLUDING REMARKS	93
15.0	REFERENCES	94
16.0	LIST OF SYMBOLS	97
	FIGURES	102

SUMMARY

This report volume presents a unified theory for aerodynamics and noise of single rotation propellers. Aerodynamic topics include calculation of performance, blade load distribution, non-uniform wake flow fields, and non-uniform upstream (potential) flow fields. Blade loading can be steady or unsteady due to fixed distortion, counter-rotating wakes, or blade vibration. The aerodynamic theory is based on the pressure potential method and is therefore basically linear. However, non-linear effects associated with finite axial induction and blade vortex flow are included via approximate methods. Acoustic topics include radiation of noise caused by blade thickness, steady loading (including vortex lift), and unsteady loading. The loading orientation includes the radial component.

The derivation begins with the development, via the acoustic analogy, of a general expression for disturbance pressure as an integral over the blade surface of the loading and thickness distribution. This immediately provides expressions for near field noise predictions. These expressions are specialized for far field noise calculation using the method of stationary phase. A section on sound power and wave drag is presented to evaluate the contribution of acoustic wave energy to aerodynamic performance loss. For unswept, supersonic tip speed blades, the acoustic power cannot be neglected in comparison with the shaft power.

For steady aerodynamic use, the integral formula for pressure is converted to a formula for downwash at control points on the blade surface as a function of loading and thickness distributions. Since the downwash is considered known from the blade camber and angle of attack distributions, the integral equation must be inverted to find the blade loading. This is accomplished in a manner similar to that of wing methods by discretizing the loading, converting the integral equation to a matrix equation, and inverting the matrix. Induced drag (or vortex drag) is computed in the Trefftz plane. A section is devoted to showing the relationship between this new lifting surface theory and classical propeller momentum theory. When the blade loading has been calculated, the wake and upstream potential field calculations are done using velocity formulas similar to the downwash equations but for field points off the blade.

For unsteady aerodynamic application, the downwash is considered known from the blade vibration. The integral equation is solved for unsteady loading by the same inversion scheme described above. The only numerical results presented in this volume are some verification cases for the 3D unsteady loading theory. Calculations of performance, wakes, and noise are presented in Volume III.

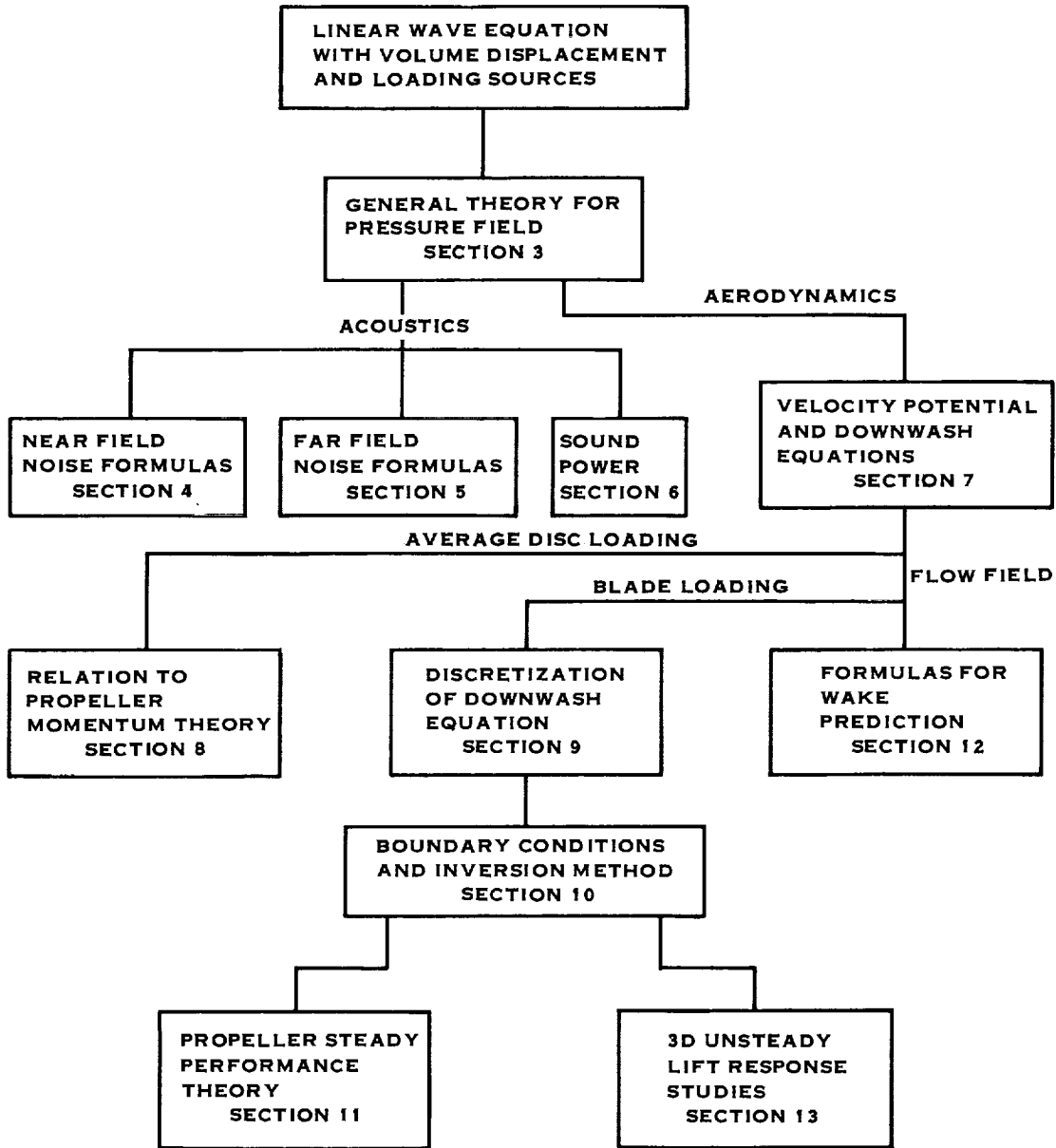
SECTION 1

INTRODUCTION

This report presents results of program for the generation of an accurate, efficient computer prediction code for noise of advanced, single rotation, turbo-props (Prop-Fans) such as the SR3 model shown in Figure 1.1. The code is based on a linearized theory developed at Hamilton Standard in which aerodynamics and acoustics are treated as a unified process. Both steady and unsteady blade loading are treated. Capabilities include prediction of steady airload distributions and associated aerodynamic performance, unsteady blade pressure response to gust interaction or blade vibration, noise fields associated with thickness and steady and unsteady loading, and wake velocity fields associated with steady loading. The code was developed on the Hamilton Standard IBM computer and has now been installed on the Cray XMP at NASA-Lewis.

The work had its genesis in the frequency domain acoustic theory developed at Hamilton Standard in the late 1970's. It was found that the method used for near field noise predictions could be adapted as a lifting surface theory for aerodynamic work via the pressure potential (or acceleration potential) technique that has been used for both wings and ducted turbomachinery. In the first realization of the theory for propellers (prior to the contract), the blade loading was represented in a quasi-vortex lattice form. Under the contract, this was upgraded to true lifting surface loading. Originally, it was believed that a purely linear approach for both aerodynamics and noise would be adequate. However, in the course of the contract, two sources of non-linearity in the steady aerodynamics became apparent and were found to be a significant factor at takeoff conditions. The first is related to the fact the steady axial induced velocity may be of the same order of magnitude as the flight speed and the second is the formation of leading edge vortices which increase lift and redistribute loading. The contract was amended to deal with both of these phenomena.

The final report is divided into 5 volumes as outlined in the Abstract. This volume (Volume I) gives the theoretical derivations and background for the aerodynamics and acoustics of rotating, unducted blades. Verification by comparison with test data is the subject of Volume III, however, this volume does include some verification by comparison with related theories. In particular, the relationship to classical propeller theories is established and treatment of high order singularities is compared with that in an analogous compressor method. The volume is divided into 13 sections, each depending on previous material. However, for readers interested in specific topics, not all of the sections need to be understood. A guide to the report sections is provided on the next page to help in understanding the flow of the derivations.



SECTION 2

BACKGROUND

This section presents a brief overview of some of the analytical methods that can be used for propeller aerodynamics and acoustics. Advantages of the pressure potential method are explained and some of its relevant history is reviewed.

There is a broad spectrum of methods that could be applied to the propeller problem and each has advantages ranging from economy on one end of the scale to accuracy at the other end. At the top end of the scale, the Euler and Navier-Stokes methods that are currently under development for Prop-Fans may, at some time, be used routinely for propeller acoustics. Indeed, Euler aerodynamic methods are currently being used to provide airloading as input for acoustic theories (ref. 1) with considerable success. The main drawback to this approach is the long computer running time for fully converged aerodynamic results. Calculations for steady airloading are rapidly becoming manageable but it appears that affordable unsteady propeller aerodynamic calculations with these fully numerical schemes are still some time in the future.

The use of an Euler calculation for a direct acoustic prediction might seem like a tractable approach for the near field. However, attempts so far (ref. 2) have suffered from poor grid resolution. Grid points must be packed closely near the blade surface for good loading results. If shock waves are to be followed out into the acoustic field, then close packing is needed there also. The result is a requirement for more grid points than are currently possible.

Potential field methods are based on less complete versions of the fluid dynamic equations but are of interest because powerful solution techniques are available. In particular, Green's function methods provide solutions for all space without the requirement for finite volume meshes. They deal with radiating waves naturally and can thus be used successfully for both aerodynamics and acoustics. Potential equations fall into the categories of velocity potential and pressure (or acceleration) potential. The major difficulty with velocity potential theory is that sources must be placed on both the blades and on their wakes. This leads to extra computational complexity, particularly for Prop-Fan cruise conditions with subsonic roots and supersonic tips. With the pressure potential formulation, however, sources need only be placed on the lifting surfaces and not on the wakes. Furthermore, the mixed subsonic, supersonic condition can be handled with Fourier transform methods. The pressure potential does lead to higher order singularities, but these can be handled analytically resulting in a practical computational method.

Pressure potential methods have been in use for many years for wing steady and unsteady aerodynamics and are treated in standard text books. For example, Bisp-linghoff, Ashley, and Halfman (ref. 3) explain the method in some detail for both incompressible and compressible flow. Also, Bisplinghoff and Ashley (ref.4) reduced the method to operator form for aeroelastic applications. In simplest terms, the pressure potential method works as follows. An analytical expression is found for the pressure field p around the wing or body of interest. The gradient of p is then used in the momentum equation

$$\frac{Dv}{Dt} = \frac{1}{\rho}(F - \nabla p)$$

where the left side represents the acceleration of a fluid particle and F is the body force, if any, acting on it. To find velocity, the acceleration of the particle is integrated from some place where the velocity is presumed known, typically upstream infinity. Body forces are avoided by dealing with particles that don't quite come into contact with the wing. (Flow at the wing is handled by a limiting process.) Linearization enters the problem in 3 significant areas. First, the pressure field is usually found by a solution of the linear wave equation. This means that bow and trailing shocks are approximated by Mach waves; attached, mid-chord shocks are not represented. The second linearization is in setting the density ρ to its ambient value ρ_0 . This is justified because the above equation is first order in the disturbance pressure so that disturbances in density would bring in second order quantities. The third entry of linearization is in approximating the particle trajectory by its undisturbed path. This seems to be satisfactory for wings because there is little fluid deflection until the particles are very near the leading edge. (The same is not necessarily true of propellers.) The pressure potential method has generated countless papers and computer programs for wing computation. The paper by Landahl and Stark (ref. 5) gives an excellent review of the subject.

The pressure potential method has also been applied to ducted rotors. The analyses by Namba (ref. 6) and by Lordi and Homicz (ref. 7) follow the general recipe given above, but with vast differences in the details. Namba's theory was used for aerodynamics and acoustics, whereas Lordi and Homicz applied theirs only to computation of blade loading. Their work is particularly interesting, however, in that it brings new insight on the role of body forces and high order singularities. These analyses use Green's functions for constant diameter, hard walled ducts and thus do not permit the kind of contracting inflow that characterizes propellers. Instead they do produce a pressure jump at the rotor that persists to downstream infinity.

For propellers, the earliest application of the pressure potential method seems to be that of Kondo (ref. 8) who worked out a version of the steady flow equations during the World War II. His expressions were not written out explicitly and apparently have never been coded for computers. Much later Tsakonas and his co-workers at the Stevens Institute of Technology developed an incompressible pressure potential method (ref. 9) for marine propellers that has been used for steady performance and for unsteady blade loading. Their integral equation is equivalent to that of the present report in the limit of zero Mach number.

The evolution of the present work has been as follows. A helicoidal surface theory (ref. 10) was derived for prediction of propeller noise caused by thickness and steady loading. This was written directly in the time domain and worked quite well for ordinary propellers even with supersonic tips. However, the combination of swept blades and supersonic tips lead to waveform predictions with a jagged character caused by numerical difficulties associated with retarded source location and numerical differentiation. These numerical problems were overcome by changing to a frequency domain approach which eliminated the need to deal with retarded source calculations. The first 2 papers using this method were restricted to the far field and to steady loading (refs 11,12). Near field formulas were then worked out, again for steady loading (refs. 13) . The far field unsteady loading theory (ref. 14) next was presented to deal with unsteadiness caused by interaction between rotors of a counter-rotation propeller. Also, near field equations for noise caused by unsteady loading were derived but not coded or published.

At the same time, it was discovered that the near field equations were suitable

for use in pressure potential aerodynamic analysis. The resulting theory (ref. 15) was presented showing the connection between the aerodynamics and acoustics and how the new theory related to previous theories for propeller noise and hydrodynamics and to theories for wing steady flow and flutter analysis. The first application of the blade loading theory was given in Reference 16. This treated the steady loading problem only and represented the loading in a sort of vortex lattice scheme.

That was the status of the analysis when the current contract work began. The major extensions of the work planned under the original contract included upgrading the loading representation from vortex lattice to true lifting surface, coding the unsteady loading noise and airload theories, adding wake prediction capability, and bringing all of the code together in a unified computer system. The work applies strictly to single rotation propellers although the wake and unsteady lift response capability needed for counter-rotation are included. Also, only linear theory was to be included. This was reasonably satisfactory for the high speed cruise cases where axial induction is small. However, for takeoff cases, it was realized that the large axial induction (compared to the flight speed), violated the linearization assumption described above that permitted integrating the fluid particle acceleration along its undisturbed path. This problem does not occur in textbook wing problems nor in ducted rotor problems where contraction ahead of the rotor cannot occur. It was not anticipated in the propeller problem. The contract was amended to address this problem and a relatively simple scheme was developed. In the process, the connection between the new theory and classical propeller momentum theory was established so that the continuum of methods can be now be understood.

The other non-linear effect that was not anticipated was the appearance of leading edge vortices at takeoff conditions. These correspond to the well known vortices on delta wing aircraft that are helpful in providing extra lift for takeoff and landing at low speeds. The conditions necessary for their formation are sharp leading edges, sweep, and high loading, all of which are present on Prop-Fans at takeoff. It turns out that the presence of leading edge vortices has been known on marine propellers for some time. Kerwin's review article (ref. 17) includes a photograph of a leading edge vortex made visible by cavitation bubbles. A sketch showing their appearance in a water tunnel experiment was presented in Reference 18 and is reproduced in Figure 2. The similarity to typical Prop-Fan geometry is remarkable. It seemed very probable that the same phenomenon was occurring on Prop-Fan blades and some flow visualization experiments were initiated in the United Technologies Acoustic Research Tunnel to demonstrate their presence. The first successful results were via surface oil flow patterns made visible with florescent dye as shown in Figure 3. The streaks show the oil flow to be predominantly in the radial direction under the influence of centrifugal force. However, there is a region where they change direction, as shown in the inset to the figure. This is the region of re-attachment of the leading edge vortex. The wind tunnel experiment was expanded to document the flow patterns over a wide range of operating conditions and the results were released in 1987 (ref. 19). Similar results have now been produced in experiments at NASA-Lewis (ref. 20) and there now seems to be little doubt about the presence of the vortices.

Since the leading edge vortices tend to produce extra lift and redistribute the airloading, the contract was also amended to deal with them. The treatment is via the suction analogy of Polhamus (ref. 21) and Lamar (ref. 22) in which leading edge thrust, which can be computed with a lifting surface panel method, is used to predict the extra leading edge loading associated with the separation and reattachment of the vortices. Application of the suction analogy to propellers is described in Volume III of this report.

SECTION 3

GENERAL PRESSURE THEORY

This section presents a derivation of the general equation for the pressure field of a propeller. The theory is based on the linear wave equation with helically convected thickness and loading sources representing the action of the blades on the air. A solution is achieved using the free-space Green's function and Fourier transforms. The general equation is needed in later sections where working equations that have been coded for near and far field noise prediction are developed. It is also the starting point for the performance analysis in Section 7.

Differential Equation

The linear governing equation for pressure disturbances is

$$\nabla^2 p - \frac{1}{c_o^2} \frac{\partial^2 p}{\partial t^2} = -S(\underline{r}, t) \quad (3.1)$$

where the source function is given by

$$S(\underline{r}, t) = \rho_o \frac{\partial q}{\partial t} - \nabla \cdot \underline{f} \quad (3.2)$$

Equation 3.1 has solution

$$p(\underline{r}, t) = \iint S(\underline{r}_o, \tau) \frac{\delta(t - \tau - R/c_o)}{4\pi R} d\underline{r}_o d\tau \quad (3.3)$$

where the distance between the field point \underline{r} and the source point \underline{r}_o is

$$R = |\underline{r} - \underline{r}_o| \quad (3.4)$$

The equations above can be found in many standard references including, for example, Goldstein (ref. 23). In the source term, q is the volume displacement/unit time/unit volume and \underline{f} is the force/unit volume acting on the fluid. In Goldstein's book q represents an actual volume injection but here we use it to represent the volume displacement effect of the blades; the resulting pressure waves are traditionally called thickness noise. Similarly, \underline{f} was derived as a volume source but is used herein to represent the blade loading in terms of surface pressure. The associated radiation is called loading noise.

In Equation 3.3, $\delta/4\pi R$ is the free space Green's function representing spherically propagating wavelets from the source. The double integral sums the source contributions from all space and time and the integration limits, which are not specified in Equation 3.3, cover all contributing regions. The problem to be treated here involves blades that are translating and rotating through the fluid. Other treatments of related problems use coordinate systems translating with the propeller (the aircraft system) or both translating and rotating with it (the blade system). Equation 3.1, however, is written for a coordinate system fixed in the fluid so that, at the beginning of the analysis, we will be dealing with the transient problem of a propeller fly-by. Because of the Fourier methods used, it will be seen that this leads to a simplified theoretical development and, in the final pressure equation, the field point may be moved to either the aircraft coordinate system or the blade coordinate system via a trivial transformation. Furthermore, using this approach, the only Mach number that appears is that associated with forward flight, which applies at all stations on the blade. Blade fixed systems

have to deal with varying Mach number along the radius and a change in the type of differential equation for supersonic section speeds. This requires some sort of a patch in solutions at the sonic radius.

Previous treatments by the author of the propeller aero-acoustic problem were based on the acoustic analogy equation, which can also be found in Goldstein (ref. 23). This brings in the surfaces explicitly; however, it was found when the boundary conditions are linearized through the thin blade approximation, that the distinction between the acoustic analogy and Equation 3.1 vanishes. Thus, the simpler approach is taken here.

Source Representation

Before Equation 3.3 can be integrated, the source term S will be represented in propeller terminology starting with the sketch in Figure 4. On the left is shown a cylindrical coordinate system centered on the propeller axis of rotation with the pitch change axis (PCA) coincident with $x=0$, $\phi=0$ at time $t=0$. ϕ is positive in the direction of rotation regardless of the direction of rotation. The sketch at the top shows a blade (say blade number 0) intersected by a cylindrical surface of radius r . If this surface were cut and rolled out flat, it would have the appearance of the sketch at the bottom in Figure 4. It is most convenient to formulate the source description in coordinates γ, ξ aligned with the direction of advance of the airfoil section at each radius. Thus, the helicoidal surface ($\xi=0$) swept out by the pitch change axis advancing at speed V and rotating at angular speed Ω is analogous to the reference plane used in wing lifting surface methods. Once the source is formulated in these coordinates, the description will be converted to conventional cylindrical coordinates before the integration of Equation 3.3. This will avoid any problems which might arise from the use of the γ, ξ, r system, which is non-orthogonal.

Thickness Source - At time $t=0$, the rate of volume displacement per unit span is given by $Uh'(\gamma)$. h is the airfoil section thickness distribution shown in Figure 4 at radius r and U is the section helical advance speed. The prime on h denotes differentiation with respect to the argument. At times other than $t=0$, motion of the source in the negative γ direction results in an argument shift yielding $Uh'(\gamma+Ut)$. The line of action of the source is placed on the offset surface via the delta function $\delta(\xi+FA)$ where FA is the face alignment. Thus, the rate of volume displacement can be written

$$q = \delta(\xi + FA) Uh'(\gamma+Ut) \quad (3.5)$$

or equivalently

$$q = \delta(\xi + FA) \frac{\partial}{\partial t} h(\gamma+Ut) \quad (3.6)$$

so that the complete thickness source description in γ, ξ coordinates is

$$\rho_0 \frac{\partial q}{\partial t} = \rho_0 \delta(\xi + FA) \frac{\partial^2}{\partial t^2} h(\gamma+Ut) \quad (3.7)$$

The thickness distribution is represented in terms of its transform via the following Fourier transform pair.

$$\psi_v(k_\gamma) = \int_{-\infty}^{\infty} h(\gamma) e^{ik_\gamma \gamma} d\gamma \quad (3.8)$$

$$h(\gamma) = \frac{1}{2\pi} \int_{-\infty}^{\infty} \psi_v(k_\gamma) e^{-ik_\gamma \gamma} dk_\gamma \quad (3.9)$$

Inserting Equation 3.9 into Equation 3.7 and performing the time derivative gives

$$\rho_o \frac{\partial q}{\partial t} = - \frac{\rho_o U^2}{2\pi} \delta(\xi+FA) \int k_\gamma^2 \psi_v(k_\gamma) e^{-ik_\gamma(\gamma+Ut)} dk_\gamma \quad (3.10)$$

To express Equation 3.10 in cylindrical coordinates, consider the $r=\text{constant}$ surface to be unwrapped onto a plane. Then the γ, ξ system can be rotated into x, ϕ using the relations

$$\gamma = -\frac{V}{U} x - \frac{\Omega r}{U} r\phi \quad (3.11)$$

$$\xi = \frac{\Omega r}{U} x - \frac{V}{U} r\phi \quad (3.12)$$

where the coefficients V/U and $\Omega r/U$ are tied to the advance triangle shown in Figure 4. The inverses of these equations are shown for future reference

$$r\phi = -\frac{\Omega r}{U} \gamma - \frac{V}{U} \xi \quad (3.11a)$$

$$x = -\frac{V}{U} \gamma + \frac{\Omega r}{U} \xi \quad (3.12a)$$

For the delta function in Equation 3.10, we first note that it is even with respect to argument and then substitute Equation 3.12 for ξ

$$\begin{aligned} \delta(\xi+FA) &= \delta\left[\frac{Vr}{U}\left(\phi - \frac{\Omega x}{V} - \frac{U}{Vr}FA\right)\right] \\ &= \frac{U}{Vr} \delta\left(\phi - \frac{\Omega x}{V} - \frac{U}{Vr}FA\right) \end{aligned} \quad (3.13)$$

The second line in Equation 3.13 follows from the integral properties of any function, say $f(ax)$: $\int f(ax) dx = 1/a \int f(x) dx$. Now, with the substitution of Equation 3.11 for γ , the thickness source has the form

$$\begin{aligned} \rho_o \frac{\partial q}{\partial t} &= \frac{-\rho_o U^3}{2\pi Vr} \delta\left(\phi - \frac{\Omega x}{V} - \frac{U}{Vr}FA\right) \\ &\times \int k_\gamma^2 \psi_v(k_\gamma) e^{ik_\gamma\left(\frac{V}{U}x + \frac{\Omega r}{U}r\phi\right)} e^{-ik_\gamma Ut} dk_\gamma \end{aligned} \quad (3.14)$$

But the source exists only on $\phi = \Omega x/V + (U/Vr)FA$ so that this can be substituted for ϕ in the exponential. The result, after recognizing that

$$U^2 = V^2 + \Omega^2 r^2 \quad (3.15)$$

defining

$$\sigma = U/V \quad (3.16)$$

and

$$K_x = \sigma k_\gamma \quad (3.17)$$

and expanding the delta function via

$$\delta(\alpha) = \frac{1}{2\pi} \sum_{n=-\infty}^{\infty} e^{in\alpha} \quad (3.18)$$

is

$$\rho_o \frac{\partial q}{\partial t} = - \frac{\rho_o V^2}{4\pi^2 r} \sum_{n=-\infty}^{\infty} \left\{ e^{in\phi} \times \int_0^{\infty} K_x^2 \psi_v \left(\frac{K_x}{\sigma} \right) e^{i(K_x - \frac{n\Omega}{V})x} e^{i(\frac{\Omega r}{U} K_x - \frac{nU}{Vr})FA} e^{-iK_x Vt} dK_x \right\} \quad (3.19)$$

where K_x is the ordinary x wavenumber. Equation 3.19 is the complete space-time description of the rotating thickness source in cylindrical coordinates. It can be verified that Equation 3.19 is time independent in the blade coordinate system x_1, ϕ_1 by substituting $x=x_1+Vt$ and $\phi=\phi_1+\Omega t$ and verifying that time drops out of the right hand side.

Loading Source - The effect of loading is handled in similar fashion. Force per unit volume f_j is expressed in terms of the surface force per unit area \hat{f}_j according to

$$f_j = - \delta(\xi+FA) \hat{f}_j(\gamma+Ut) e^{-i\omega_o t} \quad (3.20)$$

where, again, the delta function places the load on the blade surface. $j=1,2,3$ denotes the x, ϕ, r force components and the exponential accounts for the fact that the force may be harmonic at frequency ω_o . The significance of the minus sign in Equation 3.20 is that f_j represents force on the fluid and \hat{f}_j represents force on the blades. The force transforms are defined in parallel with the thickness transform in Equations 3.8 and 3.9.

$$\psi_j(k_\gamma) = \int \hat{f}_j(\gamma) e^{ik_\gamma \gamma} d\gamma \quad (3.21)$$

$$\hat{f}_j(\gamma) = \frac{1}{2\pi} \int \psi_j(k_\gamma) e^{-ik_\gamma \gamma} dk_\gamma \quad (3.22)$$

and the same operations applied to the thickness source lead to

$$f_j = \frac{-1}{4\pi^2 r} \sum e^{i(n\phi - \omega_o t)} \int \psi_j \left(\frac{K_x}{\sigma} \right) e^{i(K_x - \frac{n\Omega}{V})x} \times e^{i(\frac{\Omega r}{U} K_x - \frac{nU}{Vr})FA} e^{-iK_x Vt} dK_x \quad (3.23)$$

By applying the divergence operator in cylindrical coordinates,

$$\nabla \cdot \underline{f} = \frac{\partial f_x}{\partial x} + \frac{1}{r} \frac{\partial f_\phi}{\partial \phi} + \frac{1}{r} \frac{\partial}{\partial r} (r f_r) \quad (3.24)$$

the loading source becomes

$$\nabla \cdot \underline{f} = \frac{-1}{4\pi^2 r} \sum e^{in\phi} \left\{ \left[i \left(K_x - \frac{n\Omega}{V} \right) \psi_x + \frac{in}{r} \psi_\phi \right] e^{i(\frac{\Omega r}{U} K_x - \frac{nU}{Vr})FA} + \frac{\partial}{\partial r} \left[\psi_r e^{i(\frac{\Omega r}{U} K_x - \frac{nU}{Vr})FA} \right] \right\} e^{i(K_x - \frac{n\Omega}{V})x} e^{-i(K_x V + \omega_o)t} dK_x \quad (3.25)$$

The source function is put into final form for integration by shifting the origin of the K_x variable by ω_o/V and defining the unsteady loading order q according to

$$\omega_o = q\Omega \quad (3.26)$$

The result, including thickness and loading effects, expressed in source coordinates r_o, ϕ_o, x_o, τ , is

$$S(\underline{r}_o, \tau) = \frac{-1}{4\pi^2 r_o} \sum e^{in\phi_o} \int \psi_n \left(\frac{K_x - q\Omega/V}{\sigma_o} \right) e^{i(K_x - \frac{n+q}{V}\Omega)x_o} e^{-iK_x V\tau} dK_x \quad (3.27)$$

where

$$\psi_n = \left[\rho_o V^2 K_x^2 \psi_v - i \left(K_x - \frac{n+q}{V}\Omega \right) \psi_x - \frac{in}{r_o} \psi_\phi \right] e^{i\phi_{FA}} - \frac{\partial}{\partial r_o} \left[\psi_r e^{i\phi_{FA}} \right] \quad (3.28)$$

and

$$\phi_{FA} = \left(\frac{\Omega r_o}{U} K_x - \frac{nU_o}{Vr_o} - \frac{q\Omega^2 r_o}{VU_o} \right) FA \quad (3.29)$$

is the phase shift due to face alignment or offset of the blade section from the pitch change axis.

Integration of Source Function

We are now ready to insert the source function, just derived into the Green's function integral, Equation 3.3, and to perform the τ , x_o , and ϕ_o integrations noting that the volume element is

$$d\underline{r}_o = r_o d\phi_o dr_o dx_o \quad (3.30)$$

The τ integral can be done immediately. The result, after shifting the origin of the x_o integration by x , is

$$p(\underline{r}, t) = \frac{-1}{16\pi^3} \iiint e^{in\phi_o} \times \int \psi_n \left(\frac{K_x - q\Omega/V}{\sigma_o} \right) e^{i(K_x - \frac{n+q}{V}\Omega)x} e^{-iK_x Vt} I d\phi_o dK_x dr_o \quad (3.31)$$

where

$$I = \int_{-\infty}^{\infty} \frac{e^{iK_x M_x \sqrt{R_o^2 + x_o^2}}}{\sqrt{R_o^2 + x_o^2}} e^{i(K_x - \frac{n+q}{V}\Omega)x_o} dx_o \quad (3.32)$$

in which we have defined

$$R = \sqrt{R_o^2 + x_o^2} \quad (3.33)$$

with

$$R_o^2 = r^2 + r_o^2 - 2rr_o \cos(\phi - \phi_o) \quad (3.34)$$

Integral I is evaluated in the appendix to this section with the result that

$$I = i\pi \sum_{m=-\infty}^{\infty} J_m(r_o K_r) H_m^{(1)}(r K_r) e^{im(\phi - \phi_o)} \quad (3.35)$$

where J_m is an ordinary Bessel function, $H_m^{(1)}$ is a Hankel function of the first kind, and K_r is the radial wavenumber. The notations $r_<$ and $r_>$ denote the lesser or greater of r and r_o .

$$K_r = \sqrt{K_x^2 M_x^2 - (K_x - \frac{n+q}{V}\Omega)^2} \quad (3.36)$$

with branch cuts shown in Figure 5. K_r can also be expressed as

$$K_r = |K_r| e^{i\theta} \quad (3.37)$$

where the angle

$$\theta = \frac{\theta^+ + \theta^- + \pi}{2} \quad (3.38)$$

and the branch points are

$$k^+ = \frac{(n+q)\Omega/V}{1+M_x} \quad \text{and} \quad k^- = \frac{(n+q)\Omega/V}{1-M_x} \quad (3.39)$$

It will be shown later that these correspond to outgoing waves.

We now return to Equation 3.35 and substitute it into Equation 3.31. The ϕ_o integral is found to be

$$\int_0^{2\pi} e^{i(n-m)\phi_o} d\phi_o = 2\pi\delta_{mn} \quad (3.40)$$

The Kroneker delta enables the m-summation so that the pressure simplifies to

$$p(\underline{r}, t) = \frac{-i}{8\pi} \sum_{n=-\infty}^{\infty} e^{in\phi} \int_{r_h}^{r_t} \int_{-\infty}^{\infty} \psi_n \left(\frac{K_x - q\Omega/V}{\sigma_o} \right) e^{i(K_x - \frac{n+q}{V}\Omega)x} e^{-iK_x Vt} \\ \times J_n(r_{<}K_r) H_n^{(1)}(r_{>}K_r) dK_x dr_o \quad (3.41)$$

In Equation 3.41, the arguments of the J and H functions are complex. For numerical evaluation it is more convenient to deal with real arguments. With the branches shown in Figure 5 the JH combination can be interpreted as follows for K_x on the real axis.

Whenever $K_r^2 < 0$, including the case where $n+q=0$, then

$$J_n(r_{<}K_r) H_n^{(1)}(r_{>}K_r) = -i \frac{2}{\pi} I_n(r_{<}|K_r|) K_n(r_{>}|K_r|) \quad (3.42)$$

where I_n and K_n are modified Bessel functions. In this range of K_x , the wave pattern decays exponentially with increasing radius. Note that K 's with various subscripts are used here with different meanings. To assist in interpretation, they are defined when they first appear in the text and can also be found in the symbol list given in Section 16.

For $K_r^2 > 0$, waves are propagating and we use

$$J_n(r_{<}K_r) H_n^{(1)}(r_{>}K_r) = J_n(r_{<}|K_r|) H_n^{(1)}(r_{>}|K_r|) \quad \text{for } n+q > 0 \quad (3.43)$$

and

$$J_n(r_{<}K_r) H_n^{(1)}(r_{>}K_r) = -J_n(r_{<}|K_r|) H_n^{(2)}(r_{>}|K_r|) \quad \text{for } n+q < 0 \quad (3.44)$$

This is as far as the integrations can be carried analytically. The remaining wavenumber integration, radial integration, and harmonic summation must be performed numerically. As will be seen later, the shapes of the chordwise pressure and thickness distributions will be chosen so that the source transform ψ_n can be pre-computed and stored in numerical or analytical form.

Equation 3.41 is the pressure field of a one-bladed rotor represented in the r, ϕ, x coordinate system fixed in the fluid. Before proceeding to deal with multi-blade effects, we will demonstrate the change in form for observers in the aircraft-

fixed frame and in the blade-fixed frame. The x , ϕ , t information is contained exclusively in the exponential combination

$$E = n\phi + \left(K_x - \frac{n+q}{V} \Omega \right) x - K_x Vt \quad (3.45)$$

Most of the acoustic analysis that follows will be for an observer in the aircraft-fixed coordinate system. His axial position x_1 with respect to the plane of rotation is related to x by

$$x = x_1 + Vt \quad (3.46)$$

With this substitution, the exponential becomes

$$E = n\phi - (n+q)\Omega t + \left(K_x - \frac{n+q}{V} \Omega \right) x_1 \quad (3.47)$$

Here, the transient effect, $K_x Vt$ has vanished so that the translating observer senses only periodic components with frequencies given by $(n+q)\Omega$, as required from physical considerations. If the observer is now moved onto the rotating blade via the transformation

$$\phi = \phi_1 + \Omega t \quad (3.48)$$

then the exponential becomes

$$E = n\phi_1 - q\Omega t + \left(K_x - \frac{n+q}{V} \Omega \right) x_1 \quad (3.49)$$

so that the only frequency sensed by the blade-fixed observer is the source frequency $q\Omega$.

Normalizations

Up to this point, the development has been in terms of dimensional variables because they provide a better physical understanding of the problem. However, computer program code and input are best written in non-dimensional (or scale-independent) variables. Conversions of the radiation equation and source functions to non-dimensional terms are handled in this section.

Source and field point radius ratios are defined as

$$z_0 = r_0/r_T \quad \text{and} \quad z = r/r_T \quad (3.50)$$

and ratios of tip speed and section helical speed to flight speed are given by

$$a = \Omega r_T / V, \quad \sigma = U/V = \sqrt{1+a^2 z^2}, \quad \sigma_0 = U_0/V = \sqrt{1+a^2 z_0^2} \quad (3.51)$$

Also, the wavenumber integration variable is rescaled using

$$K_x r_T = a\omega \quad (3.52)$$

With these changes, we can write for the translating observer

$$p(\underline{r}, t) = \sum_{n=-\infty}^{\infty} \hat{P}_n e^{i[n\phi - (n+q)\Omega t]} \quad (3.53)$$

where

$$\hat{P}_n = \frac{-ia}{8\pi} \iint \psi_n \left[\frac{a}{\sigma_o r_t} (\omega - q) \right] e^{ia(\omega - n - q)x_1 / r_t} \times J_n(az_c K) H_n^{(1)}(az_c K) d\omega dz_0 \quad (3.54)$$

The $\hat{\cdot}$ on P_n signifies that, for the moment, we are dealing with a one bladed rotor. The square root in the normalized radial wavenumber

$$K = \sqrt{M_x^2 \omega^2 - (\omega - n - q)^2} \quad (3.55)$$

has the same interpretation given above in conjunction with Figure 5 regarding branches of the square root. The branch points are now

$$k^+ = \frac{q+n}{1+M_x} \quad \text{and} \quad k^- = \frac{q+n}{1-M_x} \quad (3.56)$$

Normalization of the source function ψ_n brings in the effect of sweep explicitly as a phase lag. We define a non-dimensional shape factor $F_x(X)$ for the chordwise distribution of axial force per unit area on the blade as sketched at the top in Figure 6. Regarding notation, note that the subscript x denotes axial component whereas X is the chordwise ordinate running from $-1/2$ at the leading edge to $1/2$ at the trailing edge. With normalization based on local section helical speed, the dimensional and non-dimensional quantities are related by

$$\hat{f}_x = \frac{1}{2} \rho_o U_o^2 F_x \left(\frac{\gamma - MCA}{b} \right) \quad (3.57)$$

where b is blade chord. When this is substituted into the definition of the chordwise loading transform given by Equation 3.21 and the integration variable is shifted and rescaled by

$$X = (\gamma - MCA)/b \quad (3.58)$$

the result is

$$\psi_x(k_\gamma) = \frac{1}{2} \rho_o U_o^2 b e^{ik_\gamma MCA} \int F_x(X) e^{ik_\gamma b X} dX \quad (3.59)$$

Then, by recalling the changes of variable given by Equations 3.17 and 3.52 and defining the non-dimensional source transform

$$\Psi_x(k_x) = \int_{-1/2}^{1/2} F_x(X) e^{ik_x X} dX \quad (3.60)$$

we arrive at the relationship

$$\psi_x \left[\frac{a}{\sigma_o r_t} (\omega - q) \right] = \frac{1}{2} \rho_o U_o^2 b e^{i\phi_s} \Psi_x(k_x) \quad (3.61)$$

where the upper case Ψ is used uniquely for normalized source functions. The phase lag due to sweep is

$$\phi_s = \frac{2a(\omega - q)}{\sigma_o} \frac{MCA}{D} \quad (3.62)$$

and the non-dimensional chordwise wavenumber

$$k_x = \frac{2a(\omega - q)}{\sigma_o} B_D \quad (3.63)$$

where B_D is the local chord to diameter ratio b/D . Recall that b is measured at constant radius. For Ψ_ϕ and $\hat{\Psi}_r$, the above derivation carries through with only a subscript change.

For the thickness source, the non-dimensional thickness distribution is given by $H(X)$ at the bottom in Figure 6 so that the actual thickness can be written

$$h(\gamma) = b t_b H\left(\frac{\gamma - MCA}{b}\right) \quad (3.64)$$

where t_b is the section thickness to chord ratio and $t_b b$ is the maximum thickness. Substitution into Equation 3.8 and proceeding as with the loading source normalization leads to

$$\psi_v = b^2 t_b e^{i\phi_s} \Psi_v(k_x) \quad (3.65)$$

with the normalized thickness transform

$$\Psi_v(k_x) = \int_{-1/2}^{1/2} H(X) e^{ik_x X} dX \quad (3.66)$$

Combination of the above results with Equation 3.28 leads to

$$\psi_n = \rho_o U_o^2 e^{i\phi_{FA}} e^{i\phi_s} \Psi_n(k_x) \quad (3.67)$$

where

$$\Psi_n(k_x) = k_x^2 t_b \Psi_v(k_x) + i\Psi_F(k_x) + B_D \hat{\Psi}_r(k_x) \frac{\partial}{\partial z_o}(\cdot) \quad (3.68)$$

and

$$\Psi_F = -a(\omega - n - q) B_D \Psi_x - \frac{n}{z_o} B_D \Psi_\phi \quad (3.69)$$

combines the axial and tangential force components. The partial derivative at the end of Equation 3.68 is in anticipation of an integration by parts when the source function is inserted in the radial integral. The empty parentheses (\cdot) denote the, as yet undefined, material that the derivative will operate on.

An alternative form for the combination of non-radial force components can be written in terms of lift and drag coefficients. Here, the reference directions for lift and drag are perpendicular and parallel to the local section advance direction as defined by the velocity triangle in Figure 4. This is analogous to the definition used in wing lifting surface theories where lift acts normal to the flight (or advance) direction, and is distinct from the definition used in lifting line theories where the equivalent 2D lift effect is tilted back by the induced flow angle. Lift and drag are related to thrust and torque via a rotation of coordinates by the advance angle in the following equations

$$\Psi_x = \frac{\Omega r_o}{U_o} C_L \Psi_L - \frac{V}{U_o} C_D \Psi_D \quad (3.70)$$

$$\Psi_\phi = -\frac{V}{U_o} C_L \Psi_L - \frac{\Omega r_o}{U_o} C_D \Psi_D \quad (3.71)$$

Sign conventions have been chosen so that lift and drag are positive in the usual sense. The Ψ 's for thrust and torque are related to forces on the blades so that the usual thrust would result in a positive Ψ_x and the usual torque would result in a negative Ψ_ϕ . In terms of the x wave number given above and a newly defined y wavenumber, the alternative form for Ψ_F is

$$\Psi_F = \frac{1}{2} k_y C_L \Psi_L + \frac{1}{2} k_x C_D \Psi_D \quad (3.72)$$

where

$$k_y = \frac{-2}{\sigma_o} \left[(\omega - n - q) a^2 z_o - \frac{n}{z_o} \right] B_D \quad (3.73)$$

Note that, in this representation, the integrated section lift and drag are specified by C_L and C_D and the shapes of lift and drag distributions are given by f_L and f_D . These shape functions have unit area so that the Ψ 's are defined by

$$\Psi_L(k_x) = \int f_L(X) e^{ik_x X} dx \quad (3.74)$$

$$\Psi_D(k_x) = \int f_D(X) e^{ik_x X} dx \quad (3.75)$$

With the newly defined source function in Equations 3.67-68, the pressure harmonic in Equation 3.54 can be replaced by

$$\hat{P}_n = \frac{-ia \rho_o c_o^2}{8\pi} \int_{z_h}^1 M_r^2 \int_{-\infty}^{\infty} e^{i\phi_{osx}} \Psi_n(k_x) J_n(az_{<}K) H_n^{(1)}(az_{>}K) d\omega dz_o \quad (3.76)$$

where ϕ_{osx} is the combined phase due to offset (Equation 3.29), sweep (Equation 3.62), and observer axial position

$$\phi_{osx} = \phi_{FA} + \phi_s + \phi_x \quad (3.77)$$

and the phase associated with the axial position of the observer is

$$\phi_x = a(\omega - n - q)x_1/r_T \quad (3.78)$$

Multiple Blades and Interblade Phase Angle

In the previous section Equations 3.53 and 3.76 were derived to represent the pressure field of a rotor with one blade. To deal with the multiblade case, it is assumed that the rotor comprises B blades that are identical and equally spaced around the axis. In the case of steady loading, the loading is assumed to be identical on each blade. In the unsteady case, the loading waveforms on all blades are identical but shifted in time. Thus, by proper choice of parameters, the loading on the blades of a 2-bladed rotor could be in phase or out of phase with each other. In general, the blade loading will be permitted arbitrary frequency, specified by q (not necessarily an integer multiple of the rotation frequency) and an interblade phase angle, specified by the circumferential order k of the distortion pattern (i. e., the number of nodal diameters). As will be seen, this will provide the generality to deal with unsteady loading caused by interference with fixed or rotating distortion. The fixed distortion could be caused by fuselage effects or angular inflow. The rotating distortion could be caused by blades of an upstream counter rotating rotor with a different number of blades and a different RPM. Furthermore, the loading could be induced by vibratory blade motion at an integer or non-integer multiple of the shaft rotation frequency. The extra blades are accounted for by simply adding their pressure fields according to linear superposition. The blades are identified by the counter b_2 starting at 0 for the base blade and running in the direction of rotation to $B-1$. Two effects must be included before the fields are added: the blades have different points of action and they have different phases. Equation 3.53 showed that the ϕ, t dependence of the pressure field for blade 0 is given by the exponential

$$e^{i[n\phi - (n+q)\Omega t]} \quad (3.79)$$

Moving that blade to the angular position $2\pi b_2/B$ produces an effect equivalent to moving the observer to minus that angle. Thus, to account for the point of action effect, ϕ in Equation 3.79 must be replaced by $\phi - 2\pi b_2/B$. For the phase effect, we state that the loading on blade b_2 leads that on blade 0 by an amount $2\pi k b_2/B$ where $2\pi k/B$ is the interblade phase angle and k is the number of nodal diameters in the unsteady loading pattern. The sign convention for the phase lead corresponds to the fact that, for interference with fixed distortion, a blade with the higher index b_2 encounters the distortion first. Thus, to account for interblade phase angle, we add $-2\pi k b_2/B$ to the exponential in Equation 3.53. With both effects accounted for, the result is

$$e^{i[n(\phi - 2\pi b_2/B) - (n+q)\Omega t - 2\pi k b_2/B]} \quad (3.80)$$

Thus, for blade b_2 , the phase factor

$$e^{-i2\pi(n+k)b_2/B} \quad (3.81)$$

must be inserted in Equation 3.53. Adding the pressure fields of the blades results in

$$p_2(t) = \sum_{b_2=0}^{B-1} \sum_{n=-\infty}^{\infty} \hat{P}_{n,k} e^{i[n\phi - (n+q)\Omega t]} e^{-i2\pi(n+k)b_2/B} \quad (3.82)$$

where the subscript on p_2 is to distinguish this multiblade expression from the earlier expression for a one bladed rotor. The subscript 2 is also needed in a later section where it will relate to the rear rotor of a counter-rotation system.

Equation 3.82 can be rewritten

$$p_2(t) = \sum_{n=-\infty}^{\infty} \hat{P}_{n,k} e^{i[n\phi - (n+q)\Omega t]} \sum_{b_2=0}^{B-1} e^{-i2\pi(n+k)b_2/B} \quad (3.83)$$

The sum on b_2 is 0 unless $(n+k)/B$ is an integer. When $(n+k)/B$ is an integer, say m , then the sum is equal to B and the double sum can be written

$$p_2(t) = B \sum_{m=-\infty}^{\infty} \hat{P}_{mB-k,k} e^{i[(mB-k)\phi - (mB-k+q)\Omega t]} \quad (3.84)$$

This combination will occur so often in the acoustic and aerodynamic analysis that we will write

$$p_2(t) = B \sum_{m=-\infty}^{\infty} \hat{P}_{n,k} e^{i[n\phi - (n+q)\Omega t]} \quad (3.85)$$

where it is to be understood that $n=mB-k$. Finally, we absorb the B into the harmonic definition so that the $\hat{}$ on P_n can be dropped and the complete expression for the pressure field in fuselage coordinates becomes

$$p_2(t) = \sum_{m=-\infty}^{\infty} P_{n,k} e^{i[n\phi - (n+q)\Omega t]} \quad (3.86)$$

with

$$P_{n,k} = \frac{-iaB \rho_o c_o^2}{8\pi} \int_{z_h}^1 M_r^2 \int_{-\infty}^{\infty} e^{i\phi_{osx}} \Psi_n(k_x) J_n(az_{<}K) H_n^{(1)}(az_{>}K) dw dz_0 \quad (3.87)$$

A brief discussion of the modal behavior implied by Equation 3.84 is in order. The exponential is

$$E = (mB - k)\phi - (mB - k + q)\Omega t \quad (3.88)$$

which clearly represents a mode with $mB-k$ lobes in the circumferential direction and a frequency $(mB-k-q)\Omega/2\pi$ as observed in the fuselage coordinate system. The mode is spinning about the propeller axis at a rate that can be deduced by noting that the zero phase point from Equation 3.88 has angular location

$$\phi_{\text{const}} = \frac{mB-k+q}{mB-k} \Omega t \quad (3.89)$$

so that the modal spin rate is given by the same expression without the t . The mode can spin faster or slower than the rotor speed and in the same or opposite direction. Specific cases for fixed and counter-rotation distortion have been discussed in Reference 14.

In the blade frame, $\phi = \phi_1 + \Omega t$ and the exponential becomes

$$E = (mB-k)\phi_1 - q\Omega t \quad (3.90)$$

again indicating that $q\Omega$ is the only frequency observed in blade coordinates.

Sum Over Loading Harmonics

In this section, we bring in the effect of multiple loading harmonics and establish criteria for converting the double sided sums to sums with only positive indices. We also verify that the pressure formulas yield real results despite a great deal of complex arithmetic. The multiple loading harmonics are treated in the context of interaction with another rotor. The reason for this is that it leads to perfectly general results, since arbitrary loading frequencies can be generated by varying the speed and number of blades on the upstream rotor. For example, stopping the front rotor and setting its number of blades to 1 gives results applicable to fixed flow distortion. This report deals only with the effects of specified unsteady loading or specified air angle harmonics; the methodology to compute this input from front rotor wakes or other distortion fields has not yet been completed.

To distinguish the 2 rotors, the front and rear will be labeled 1 and 2, respectively. The following equations are written for the pressure field of the rear rotor only because one generally thinks of wakes from the front rotor impinging on the rear to cause unsteady loading and noise. Of course, the front rotor also experiences unsteady loading in the counter-rotation case and the reader can supply formulas for this by switching indices. The angular speeds and blade counts of the 2 rotors will be denoted Ω_1 and Ω_2 and B_1 and B_2 . When these are not subscripted, they apply to the rear rotor.

In the above derivation unsteady loading occurred at only one frequency ω_0 . For example, the loading in blade-fixed coordinates for the x force component was

$$\hat{f}_x(\gamma) e^{-i\omega_0 t} \quad (3.91)$$

where ω_0 was set equal to $q\Omega$. This can be generalized to represent the unsteady loading waveform as a harmonic series. The spatial frequencies in the wake from the

front rotor are kB_1 where k takes on all integer values. The relative speed of the 2 rotors is $\Omega_1 + \Omega_2$ so that the frequencies sensed by the rear rotor are $(\Omega_1 + \Omega_2)kB_1$. Thus, the waveform for the x component of loading can be written

$$\hat{f}_x(\gamma, t) = \sum_{k=-\infty}^{\infty} \hat{f}_{xk}(\gamma) e^{-i(\Omega_1 + \Omega_2)kB_1 t} \quad (3.92)$$

We are interested in real loading only. This is assured by insisting that

$$\hat{f}_{x(-k)} = \hat{f}_{xk}^* \text{ where the } * \text{ denotes complex conjugate.}$$

From the above it can be seen that noise formulas for the general counter-rotation case are obtained from Equations 3.86 and Equations 3.87 by replacing q , k , and n as follows and summing over the loading harmonic index k .

$$q \rightarrow (1 + \Omega_{12})kB_1 \quad (3.93)$$

$$k \rightarrow kB_1 \quad (3.94)$$

$$n \rightarrow mB_2 - kB_1 \quad (3.95)$$

where we have defined $\Omega_{12} = \Omega_1 / \Omega_2$. The result is

$$p_2(t) = \sum_{m=-\infty}^{\infty} \sum_{k=-\infty}^{\infty} P_{n,k} e^{i[n\phi - (n+q)\Omega t]} \quad (3.96)$$

where

$$P_{n,k} = \frac{-iaB\rho_0 c_0^2}{8\pi} \int_{z_h}^1 M_r^2 \int_{-\infty}^{\infty} e^{i\phi_{osx}} \Psi_{n,k}(k_x) J_{|n|}(az_{<}K) H_{|n|}^{(1)}(az_{>}K) d\omega dz_0 \quad (3.97)$$

The absolute value signs can be included or not because of the property that $J_{-n} = (-1)^n J_n$ and $Y_{-n} = (-1)^n Y_n$. The composite source function with k subscripts is

$$\Psi_{n,k}(k_x) = k_x^2 t_b \Psi_v(k_x) + i\Psi_{Fk}(k_x) + B_D \Psi_{rk}(k_x) \frac{\partial}{\partial z_0}(\cdot) \quad (3.98)$$

with

$$\Psi_{Fk} = -a(\omega - n - q)B_D \Psi_{xk} - \frac{n}{z_0} B_D \Psi_{\phi k} \quad (3.99)$$

or

$$\Psi_{Fk} = \frac{1}{2} k_y C_{Lk} \Psi_{Lk} + \frac{1}{2} k_x C_{Dk} \Psi_{Dk} \quad (3.100)$$

The (\cdot) notation was explained in conjunction with Equation 3.68. Of course there is no sum on k for the thickness source. The wavenumbers and phase lags are collected here for reference:

$$K = \sqrt{M_x^2 \omega^2 - (\omega - n - q)^2} \quad (3.101)$$

$$k_x = \frac{2a}{\sigma_0} (\omega - q) B_D \quad (3.102)$$

$$k_y = -\frac{2}{\sigma_0} \left[(\omega - n - q) a^2 z_0 - \frac{n}{z_0} \right] B_D \quad (3.103)$$

$$\phi_{FA} = \frac{2}{\sigma_0} \left[(\omega - n - q) a^2 z_0 - \frac{n}{z_0} \right] \frac{FA}{D} \quad (3.104)$$

$$\phi_s = \frac{2a}{\sigma_0} (\omega - q) \frac{MCA}{D} \quad (3.105)$$

$$\phi_x = a(\omega - n - q) \frac{x_1}{r_1} \quad (3.106)$$

The notation for phase due to face alignment or offset ϕ_{FA} was ϕ_0 in previous references by Hanson.

Before proceeding with the discussion of folding double sided sums, we have to establish that

$$P_{-n,-k} = [P_{n,k}]^* \quad (3.107)$$

To this end, note that the integrand in Equation 3.97 can be written as the product of a real constant times 3 factors:

$$[e^{i\phi_{osx}}] [\Psi_{nk}(k_x)] [iJ_{|n|}(az_{<}K)H_{|n|}^{(1)}(az_{>}K)] \quad (3.108)$$

If the signs of the n and k indices are changed everywhere and the substitution $\omega \rightarrow -\omega$ is made, it is found that k_x , k_y , q , and all of the ϕ 's also change sign.

Thus, for the first factor in Equation 3.108,

$$e^{i\phi_{osx}} \rightarrow e^{-i\phi_{osx}} = [e^{i\phi_{osx}}]^* \quad (3.109)$$

Also, for real loading it can be shown for the source function in Equation 3.108 that

$$\Psi_{-n,-k} = \Psi_{n,k}^* \quad (3.110)$$

For the third factor, recall that $iJH^{(1)}$ is interpreted as follows

$$iJ_{|n|}(az_{<}|K|)H_{|n|}^{(1)}(az_{>}|K|) \quad \text{for } K^2 > 0, \quad (n+q) > 0 \quad (3.111)$$

$$-iJ_{|n|}(az_{<}|K|)H_{|n|}^{(2)}(az_{>}|K|) \quad \text{for } K^2 > 0, \quad (n+q) < 0 \quad (3.112)$$

$$\frac{2}{\pi} I_{|n|}(az_{<}|K|)K_{|n|}(az_{>}|K|) \quad \text{for } K^2 < 0, \quad \text{all } (n+q) \quad (3.113)$$

Since $H_n^{(2)}(x) = [H_n^{(1)}(x)]^*$ and J_n , I_n , and K_n are real, it follows that whenever $(n+q)$ changes sign the third factor in Equation 3.108 changes to its complex conjugate. From the above plus the fact that

$$\int_{-\infty}^{\infty} f(\omega) d\omega = \int_{-\infty}^{\infty} f(-\omega) d\omega \quad (3.114)$$

for any function, Equation 3.107 is established and permits us to deal with folding of the sums.

The pressure waveform in Equation 3.96 was written in terms of a complex amplitude and an exponential. For this section only, these can be combined into one variable $Q_{n,k}$ as follows

$$Q_{n,k} = P_{n,k} e^{i[n\phi - (n+q)\Omega t]} \quad (3.115)$$

which from Equations 3.93 - 3.95 and Equation 3.115 has the property $Q_{-n,-k} = Q_{n,k}^*$. The waveform can now be written

$$p_2(t) = \sum_{m=-\infty}^{\infty} \sum_{k=-\infty}^{\infty} Q_{n,k} \quad (3.116)$$

The sums can be split as follows

$$p_2(t) = Q_{0,0} + \sum_{m=-1}^{-\infty} Q_{m,0} + \sum_{m=1}^{\infty} Q_{m,0} + \sum_{m=-\infty}^{\infty} \sum_{k=-1}^{\infty} Q_{n,k} + \sum_{m=-\infty}^{\infty} \sum_{k=1}^{\infty} Q_{n,k} \quad (3.117)$$

where the first 3 terms deal with thickness and steady loading and the last 2 deal with unsteady loading. In the second and third terms we change m to -m and in the

third term we change k to $-k$ with the result

$$p_2(t) = Q_{0,0} + \sum_{m=1}^{\infty} (Q_{-n,0} + Q_{n,0}) + \sum_{m=-\infty}^{\infty} \sum_{k=1}^{\infty} (Q_{-n,-k} + Q_{n,k}) \quad (3.118)$$

From the property just established on negative indices, this is

$$p_2(t) = Q_{0,0} + \sum_{m=1}^{\infty} (Q_{n,0}^* + Q_{n,0}) + \sum_{m=-\infty}^{\infty} \sum_{k=1}^{\infty} (Q_{n,k}^* + Q_{n,k}) \quad (3.119)$$

or

$$p_2(t) = Q_{0,0} + 2 \times \text{R.P.} \sum_{m=1}^{\infty} Q_{n,0} + 2 \times \text{R.P.} \sum_{m=-\infty}^{\infty} \sum_{k=1}^{\infty} Q_{n,k} \quad (3.120)$$

where R.P. means "real part of". Thus, on returning to the original notation, the pressure

$$p_2(t) = \sum_{m=-\infty}^{\infty} \sum_{k=-\infty}^{\infty} P_{n,k} e^{i[n\phi - (n+q)\Omega t]} \quad (3.121)$$

can now be expressed in the form

$$p_2(t) = P_{0,0} + 2 \times \text{R.P.} \sum_{m=1}^{\infty} P_{n,0} e^{imB(\phi - \Omega t)} + 2 \times \text{R.P.} \sum_{m=-\infty}^{\infty} \sum_{k=1}^{\infty} P_{n,k} e^{i[n\phi - (n+q)\Omega t]} \quad (3.122)$$

The first term is the time-average pressure, the second is the unsteady pressure due to thickness and steady loading, and the third is the unsteady pressure due to unsteady loading.

An alternative form can be derived by the same method

$$p_2(t) = P_{0,0} + 2 \times \text{R.P.} \sum_{k=1}^{\infty} P_{0,k} e^{-ikB_1(\phi - \Omega_1 t)} + 2 \times \text{R.P.} \sum_{m=1}^{\infty} \sum_{k=-\infty}^{\infty} P_{n,k} e^{i[n\phi - (n+q)\Omega t]} \quad (3.123)$$

In either case, in the double sum, only one of the sums can be folded (eliminating the negative summation indices). The other must run from $-\infty$ to ∞ .

In this section we have derived general expressions for the disturbance pressure in the field caused by a propeller with blade loading and thickness. This is in a form directly applicable to near field noise predictions, as shown in the next section. In later sections the formulas are specialized for far field noise and for aerodynamic applications.

APPENDIX TO SECTION 3

SOURCE INTEGRATION IN AXIAL DIRECTION

Part of the derivation in Section 3 required integrating a Fourier description of the source over the fluid volume. The x_0 component of this integral was given by Equation 3.32, which is repeated here.

$$I = \int_{-\infty}^{\infty} \frac{e^{iK_x M_x \sqrt{R_0^2 + x_0^2}}}{\sqrt{R_0^2 + x_0^2}} e^{i(K_x - \frac{n+q}{V}\Omega)x_0} dx_0 \quad (3A.1)$$

The integral is required for $-\infty < K_x < \infty$ and $-\infty < n+q < \infty$ for $M_x < 1$. This appendix shows how the integral is evaluated for K_x in various ranges and deals with choosing correct branch cuts for the square root that appears in the radial wavenumber.

First, we change the integration variable according to

$$x_0 = R_0 \sinh u \quad (3A.2)$$

which leads immediately to

$$I = \int_{-\infty}^{\infty} e^{iK_x M_x R_0 \cosh u + i(K_x - \frac{n+q}{V}\Omega)R_0 \sinh u} du \quad (3A.3)$$

This is in the form of Heine's formula, which is quoted from Reference 24:

$$i\pi H_0^{(1)}(\sqrt{z^2 - \zeta^2}) = \int_{-\infty}^{\infty} e^{iz \cosh u + i\zeta \sinh u} du \quad (3A.4)$$

which is valid for

$$\text{Im}(z \pm \zeta) > 0 \quad (3A.5)$$

The requirement on the imaginary parts of z and ζ can be satisfied by including a small damping factor ϵ in the first exponential of Equation 3A.3:

$$I = \int_{-\infty}^{\infty} e^{i(K_x + i\epsilon)M_x R_0 \cosh u + i(K_x - \frac{n+q}{V}\Omega)R_0 \sinh u} du \quad (3A.6)$$

For $\epsilon > 0$, Heine's formula gives

$$I = i\pi H_0^{(1)}(R_0 K_r) \quad (3A.7)$$

where

$$K_r = \sqrt{(K_x + i\epsilon)^2 M_x^2 - [K_x - (n+q)\frac{\Omega}{V}]^2} \quad (3A.8)$$

To establish the branch cuts for K_r , note that by factoring the argument of the square root and setting $\beta = \sqrt{1 - M_x^2}$. It can be shown that K_r^2 can be written

$$K_r^2 = -\beta^2 (K_x - k^+) (K_x - k^-) \quad (3A.9)$$

whose zeros are

$$k^+ = \frac{(n+q)\Omega/V}{1+M_x} - i\epsilon \frac{M_x}{1+M_x} \quad (3A.10)$$

and

$$k^- = \frac{(n+q)\Omega/V}{1-M_x} + i\epsilon \frac{M_x}{1-M_x} \quad (3A.11)$$

Now, if we define

$$K_x - k^+ = R^+ e^{i\theta^+} \quad \text{and} \quad K_x - k^- = R^- e^{i\theta^-} \quad (3A.12)$$

we can then write

$$K_r = \beta \sqrt{R^+ R^-} e^{i(\theta^+ + \theta^- + \pi)/2} = |K_r| e^{i\theta} \quad (3A.13)$$

where

$$\theta = \frac{\theta^+ + \theta^- + \pi}{2} \quad (3A.14)$$

The zeros k^+ and k^- are the branch points of the square root and the branch cuts can be taken as sketched in Figure 7. The consequence of choosing $\epsilon > 0$ is that k^+ is always below the real axis and k^- is always above. Thus, if the K_x integration is along the real axis, Equation 3A.5 is always satisfied.

To permit integration over the source angle ϕ_0 in Section 3, the Hankel function in Equation 3A.7 is expanded via the Bessel function addition theorem given in Reference 25 on page 363 with the result

$$I = i\pi \sum_{m=-\infty}^{\infty} J_m(r_c K_r) H_m^{(1)}(r_s K_r) e^{im(\phi - \phi_0)} \quad (3A.15)$$

where r_c and r_s are the smaller and larger of the source radius r_0 and the field point radius r , respectively, in cylindrical coordinates.

We can now safely pass to the limit of zero damping, $\epsilon \rightarrow 0$, in which case Equation 3.A8 becomes

$$K_r^2 = K_x^2 M_x^2 - [K_x - (n+q)\frac{\Omega}{V}]^2 \quad (3A.16)$$

Integral I is well behaved for K_x everywhere in this limit except near the branch points, where it has logarithmic singularities. These can be integrated analytically or can be circumvented by deforming the integration contour for K_x above k^+ and below k^- as shown in Figure 5. Equations 3A.15 and 16 are the results needed to continue the derivation in Section 3 at Equation 3.37.

SECTION 4

NEAR FIELD NOISE PREDICTION FORMULAS

In the preceding section Equations 3.96 to 3.106 and 3.122 were derived as a general representation of the pressure field of propeller due to thickness and loading. In this section the pressure equations are written in various special forms for noise applications. The special forms are 1) for thickness and steady non-radial loading, 2) for radial loading (steady and unsteady), 3) for unsteady loading caused by interference with wakes from any upstream counter-rotation rotor, 4) the same where the 2 rotors have the same numbers of blades and the same RPM, and 5) for unsteady loading cause by interference with fixed (non-rotating) inflow distortion. The special forms are related to equations that have appeared in previous papers by the author. With regard to counter-rotation, the reader is reminded that this report deals with noise and airloading of a single rotor caused by specified non-uniform inflow. The means to compute the non-uniform inflow from front rotor wakes or other distortion fields are not included in this report.

Thickness and Steady Non-Radial Loading

For steady loading, k and q are 0 so that $n=mB$. In this case only the second term from Equation 3.122 is needed

$$p_2(t) = 2 \times R.P. \sum_{m=1}^{\infty} P_{mB} e^{imB(\phi - \Omega t)} \quad (4.1)$$

where $P_{mB} = P_{mB,0}$ can be derived from Equation 3.87 by noting that for acoustic applications the field point radius ratio z will generally be larger than the blade tip radius so that the $z_<$, $z_>$ notation is not necessary:

$$P_{mB} = \frac{-iaB\rho_0 c_0^2}{8\pi} \int_{z_h}^1 M_r^2 \int_{-\infty}^{\infty} e^{i\phi_{osx}} [k_x^2 t_b \Psi_v(k_x) + i\Psi_F(k_x)] \times J_{mB}(az_0 K) H_{mB}^{(1)}(azK) dw dz_0 \quad (4.2)$$

The source transform was given by Equation 3.100:

$$\Psi_F = \frac{1}{2} [k_x C_D \Psi_D(k_x) + k_y C_L \Psi_L(k_x)] \quad (4.3)$$

$C_L = C_{L0}$ and $C_D = C_{D0}$ are the steady lift and drag coefficients. The radial wavenumber from Equation 3.101 is

$$K = \sqrt{M_x^2 \omega^2 - (\omega - mB)^2} \quad (4.4)$$

the composite phase factor, from Equation 3.77, is

$$\phi_{osx} = \phi_{FA} + \phi_s + \phi_x \quad (4.5)$$

where the phase lag due to face alignment and sweep (Equations 3.104 and 3.105) are

$$\phi_{FA} = 2 \left(\frac{a^2 z_0}{\sigma_0} \omega - \frac{mB \sigma_0}{z_0} \right) \frac{FA}{D} \quad (4.6)$$

$$\phi_s = \frac{2a\omega}{\sigma_0} \frac{MCA}{D} \quad (4.7)$$

The phase associated with observer position, from Equation 3.106, is

$$\phi_x = a(\omega - mB) \frac{x_1}{r_T} \quad (4.8)$$

The x and y wavenumbers were given in Equations 3.102 and 3.103:

$$k_x = \frac{2a\omega}{\sigma_o} B_D \quad (4.9)$$

$$k_y = 2 \left[\frac{-a^2 z_o}{\sigma_o} \omega + \frac{mB\sigma_o}{z_o} \right] B_D \quad (4.10)$$

If the wavenumber integration variable is changed via the substitution $\omega = mBk$, then the above equations become the same as those published previously in Reference 13.

Radial Loading - Steady and Unsteady

A formula was presented in Reference 26 for the far field noise due to steady radial loading without giving details of the derivation. Here we present the more general near field formula including both the steady and unsteady effects. The far field results are given in Section 5.

The pressure waveform was given by Equation 3.96, which is repeated here for convenience.

$$P_2(t) = \sum_{m=-\infty}^{\infty} \sum_{k=-\infty}^{\infty} P_{n,k} e^{i[n\phi - (n+q)\Omega t]} \quad (4.11)$$

When only the radial load source from Equation 3.98 is retained from Ψ_n and inserted in Equation 3.97, the pressure harmonic becomes

$$P_{n,k} = \frac{-iaB\rho_o c_o^2}{8\pi} \int_{M_r^2} e^{i\phi_{osx}} B_D \Psi_r(k_x) \frac{\partial}{\partial z_o} \left[J_n(az_{<}K) H_n^{(1)}(az_{>}K) \right] d\omega dz_o \quad (4.12)$$

For noise it is assumed that the field point is always beyond the tip so that $z_{>} = z$ and $z_{<} = z_o$. Then the derivative acts only on the J Bessel function with the result

$$P_{n,k} = \frac{-iaB\rho_o c_o^2}{8\pi} \int_{M_r^2} e^{i\phi_{osx}} k_r \Psi_r(k_x) J_n'(az_{<}K) H_n^{(1)}(az_{>}K) d\omega dz_o \quad (4.13)$$

where

$$k_r = aKB_D \quad (4.14)$$

This result is provided for reference here. It has not been coded.

Unsteady Loading - Non-Radial

This section presents formulas for noise caused by unsteady loading, excluding any radial component. Far field versions of these formulas were presented in Reference 11 and will be given again in Section 5.

Three cases are treated: in the first, the 2 rotors have different speeds and different blade numbers. In the second, the rotors have the same speed and blade numbers and in the last case the front rotor is stopped so that the results apply to an inlet guide vane configuration or the general case of fixed flow distortion. If the first case alone were coded, the second and third could be computed from it simply by using the proper input; however, if only the special cases are needed, the code for them would be somewhat simpler. The following equations are written for the radiation from the rear rotor only but the reader can supply formulas for the front rotor by switching indices. The angular speed and blade count of the front rotor are denoted by Ω_1 and B_1 . For the rear rotor they are denoted by Ω_2 and B_2 or simply Ω and B .

In Section 3, it was seen that noise formulas for the general counter-rotation case are obtained from Equations 3.95 to 3.106 with $q\Omega$ set to $(\Omega_1 + \Omega_2)kB_1$, k set to kB_1 , and n set to $mB_2 - kB_1$. Results are listed below.

General Counter-Rotation Case

$$P_2(t) = \sum_{m=-\infty}^{\infty} \sum_{k=-\infty}^{\infty} P_{n,k} e^{i[(mB_2 - kB_1)\phi - (mB_2 + kB_1\Omega_{12})\Omega_2 t]} \quad (4.15)$$

where the rotor speed ratio $\Omega_{12} = \Omega_1/\Omega_2$ and

$$P_{n,k} = \frac{aB_2\rho_0 c_0^2}{8\pi} \int_{z_h}^1 M_r^2 \int_{-\infty}^{\infty} e^{i\phi_{osx}} \Psi_{FK}(k_x) J_n(az_0 K) H_n^{(1)}(azK) d\omega dz_0 \quad (4.16)$$

$$\Psi_{FK}(k_x) = \frac{1}{2} [k_y C_{LK} \Psi_{LK}(k_x) + k_x C_{DK} \Psi_{DK}(k_x)] \quad (4.17)$$

and

$$K = \sqrt{M_x^2 \omega^2 - (\omega - mB_2 - kB_1\Omega_{12})^2} \quad (4.18)$$

$$n = mB_2 - kB_1 \quad (4.19)$$

$$k_x = \frac{2a}{\sigma_0} [\omega - kB_1(1 + \Omega_{12})] B_D \quad (4.20)$$

$$k_y = \frac{-2}{\sigma_0} \left[(\omega - mB_2 - kB_1\Omega_{12}) a^2 z_0 - (mB_2 - kB_1) \frac{1}{z_0} \right] B_D \quad (4.21)$$

$$\phi_{FA} = \frac{2}{\sigma_0} \left[(\omega - mB_2 - kB_1\Omega_{12}) a^2 z_0 - (mB_2 - kB_1) \frac{1}{z_0} \right] \frac{FA}{D} \quad (4.22)$$

$$\phi_s = \frac{2a}{\sigma_0} [\omega - kB_1(1 + \Omega_{12})] \frac{MCA}{D} \quad (4.23)$$

$$\phi_x = a(\omega - mB_2 - kB_1\Omega_{12}) \frac{x_1}{r_T} \quad (4.24)$$

For the steady loading case, these formulas reduce exactly to those in Equations 4.1 through 4.10 by taking $k=0$ only. From the form of Equation 4.15, it can be seen that sound harmonics appear at frequencies $(mB_2\Omega_2 + kB_1\Omega_1)/2\pi$ where m and k take on all integer values.

Special Case - Equal Blade Numbers and Equal RPM's

In this case we can set $\Omega_1 = \Omega_2 = \Omega$, $B_1 = B_2 = B$. Then, by shifting the origin of the m series and substituting $mB\omega$ for ω , the pressure is found to be

$$P_2(t) = \sum_{m=-\infty}^{\infty} \sum_{k=-\infty}^{\infty} P_{n,k} e^{i[(m-2k)B\phi - mB\Omega t]} \quad (4.25)$$

$$P_{n,k} = \frac{amB^2 \rho_o c_o^2}{8\pi} \int_{z_h}^1 M_r^2 \int_{-\infty}^{\infty} e^{i\phi_o s x} \Psi_{FK}(k_x) J_n(mBaz_o K) H_n^{(1)}(mBaz_o K) dw dz_o \quad (4.26)$$

$$\Psi_{FK}(k_x) = \frac{1}{2} [k_y C_{LK} \Psi_{LK}(k_x) + k_x C_{DK} \Psi_{DK}(k_x)] \quad (4.27)$$

and

$$K = \sqrt{M_x^2 \omega^2 - (\omega - 1)^2} \quad (4.28)$$

$$n = (m - 2k)B \quad (4.29)$$

$$k_x = \frac{2a}{\sigma_o} (mB\omega - 2kB) B_D \quad (4.30)$$

$$k_y = \frac{-2}{z_o \sigma_o} [mB(a^2 z_o^2 \omega - \sigma_o^2) + 2kB] B_D \quad (4.31)$$

$$\phi_{FA} = \frac{2}{z_o \sigma_o} [mB(a^2 z_o^2 \omega - \sigma_o^2) + 2kB] \frac{FA}{D} \quad (4.32)$$

$$k_x = \frac{2a}{\sigma_o} (mB\omega - 2kB) \frac{MCA}{D} \quad (4.33)$$

$$\phi_x = amB(\omega - 1) \frac{x_1}{r_T} \quad (4.34)$$

The frequencies sensed by the fuselage-fixed observer in this case are given by $mB\Omega$, i.e. harmonics of blade passing frequency. Thus, despite the counter-rotation interaction, the frequencies that appear are exactly the same as for a single rotation propeller or a fan with guide vanes. The main benefit of shifting the origin of the m summation is that the argument of the Bessel function becomes independent of k . This takes advantage of the fact that standard Bessel function subroutines return all orders of the function for a specified argument.

Special Case - Guide Vanes or Other Fixed Inflow Distortion

These results are obtained from the general formulas in Equations 4.15 to 4.24 by setting $B_2=B$, $\Omega_{12}=0$, and $B_1=1$. Also, the ω integration is modified as in the preceding formulas.

$$p_2(t) = \sum_{m=-\infty}^{\infty} \sum_{k=-\infty}^{\infty} P_{n,k} e^{i[(mB-k)\phi - mB\Omega t]} \quad (4.35)$$

$$P_{n,k} = \frac{amB^2 \rho_o c_o^2}{8\pi} \int_{z_h}^1 M_r^2 \int_{-\infty}^{\infty} e^{i\phi_{osx}} \Psi_{FK}(k_x) J_n(mBaz_c K) H_n^{(1)}(mBaz_s K) dw dz_o \quad (4.36)$$

$$\Psi_{FK}(k_x) = \frac{1}{2} [k_y C_{Lk} \Psi_{Lk}(k_x) + k_x C_{Dk} \Psi_{Dk}(k_x)] \quad (4.37)$$

and

$$K = \sqrt{M_x^2 \omega^2 - (\omega - 1)^2} \quad (4.38)$$

$$n = mB - k \quad (4.39)$$

$$k_x = \frac{2a}{\sigma_o} (mB\omega - k) B_D \quad (4.40)$$

$$k_y = \frac{-2}{z_o \sigma_o} [mB(a^2 z_o^2 \omega - \sigma_o^2) + k] B_D \quad (4.41)$$

$$\phi_{FA} = \frac{2}{z_o \sigma_o} [mB(a^2 z_o^2 \omega - \sigma_o^2) + k] \frac{FA}{D} \quad (4.42)$$

$$\phi_s = \frac{2a}{\sigma_o} (mB\omega - k) \frac{MCA}{D} \quad (4.43)$$

$$\phi_x = amB(\omega - 1) \frac{x_1}{r_T} \quad (4.44)$$

The formulas above apply to the general fixed inflow distortion case where all of the loading harmonics are generated. For the guide vane case, replace k everywhere by kV , where V is the number of inlet or exit guide vanes (not to be confused with velocity V used elsewhere in this report). Again, note that the only frequencies are given by $mB\Omega$, i.e. BPF and multiples.

SECTION 5

FAR FIELD NOISE PREDICTION FORMULAS

In this section the general formulas of Section 3 (Equations 3.96 to 3.101) are specialized for observers far from the propeller. It is shown that, at large radius, the wavenumber integral of the near field formulas can be done analytically by the method of stationary phase. Then the far field formulas are written out in various forms for the general counter rotation case and for the same special cases treated in Section 4 for near field noise.

Stationary Phase Integral

In Section 3, Equation 3.96 gave the pressure waveform as

$$p_2(t) = \sum_{m=-\infty}^{\infty} \sum_{k=-\infty}^{\infty} P_{n,k} e^{i[n\phi - (n+q)\Omega t]} \quad (5.1)$$

The counter rotation kinematics enter explicitly via the substitutions for n , q , and k given in Equations 3.93 -95. The pressure harmonic is written in the following form

$$P_{n,k} = \frac{-iaB\rho_0 c_0^2}{8\pi} \int_{z_h}^1 M_T^2 I_{n,k} dz_0 \quad (5.2)$$

so that we can concentrate on the wavenumber integral $I_{n,k}$. This has 2 forms, depending on the sign on $n+q$:

$$I_{n,k} = \begin{cases} I_{n,k}^+ & \text{for } n+q > 0 \\ I_{n,k}^- & \text{for } n+q < 0 \end{cases} \quad (5.3)$$

These forms are (see Equations 3.111 and 3.112)

$$I_{n,k}^+ = \int_{w_1}^{w_2} e^{i\phi_{os}} e^{i\phi_x} \Psi_n(k_x) J_{|n|}(az_0|K|) H_{|n|}^{(1)}(az|K|) dw \quad (5.4)$$

and

$$I_{n,k}^- = - \int_{w_2}^{w_1} e^{i\phi_{os}} e^{i\phi_x} \Psi_n(k_x) J_{|n|}(az_0|K|) H_{|n|}^{(2)}(az|K|) dw \quad (5.5)$$

where the integration ranges specified by w_1 and w_2 encompass only the radiating values of the integration variable (where $K^2 > 0$). The offset and sweep phases

$$\phi_{os} = \phi_{FA} + \phi_s \quad (5.6)$$

were given in Equations 3.104 and 3.105 and the phase associated with observer position is

$$\phi_x = a(\omega - n - q)x_1/r_T \quad (5.7)$$

as given by Equation 3.106. The radial wavenumber (Equation 3.101) is

$$K = \sqrt{M_x^2 \omega^2 - (\omega - n - q)^2} \quad (5.8)$$

We will analyze the case for $n+q>0$ in some detail and then simply explain the differences for the $n+q<0$ case. For large field point radius z , the Hankel function can be replaced by its large-argument asymptotic form

$$H_n^{(1)}(y) \rightarrow \sqrt{\frac{2}{\pi y}} e^{i(y - \frac{n\pi}{2} - \frac{\pi}{4})} \quad (5.9)$$

With this substitution for the Hankel function, the wavenumber integral becomes

$$I_{n,k}^+ = \int e^{i(\phi_{os} - \frac{|n|\pi}{2} - \frac{\pi}{4})} \Psi_n(k_x) J_{|n|}(az_o K) \sqrt{\frac{2}{\pi az_o K}} e^{ia[(\omega-n-q)x_1/r_T + zK]} d\omega \quad (5.10)$$

where the branches of the complex square root of K in Equation 5.8 require special consideration as discussed in the appendix to Section 3. For the far field, we will use retarded coordinates for convenience. Thus, as suggested in Figure 8, x_r gives the position of the propeller when it emitted the signal that arrives at the observer when he sees the propeller at x_1 . The 2 variables are related by

$$x_1 = x_r - M_x \sqrt{x_r^2 + y^2} \quad (5.11)$$

We have defined $\sqrt{x_r^2 + y^2}$ as the radiation distance. In terms of the retarded angle θ and the distance parameter

$$\hat{R} = \sqrt{x_r^2 + y^2} / r_T \quad (5.12)$$

the last exponential in $I_{n,k}^+$ can be expressed as $i\hat{R}h(\omega)$ where

$$h(\omega) = aK \sin\theta + a(\omega - n - q)(\cos\theta - M_x) \quad (5.13)$$

so that

$$I_{n,k}^+ = \int g(\omega) e^{i\hat{R}h(\omega)} d\omega \quad (5.14)$$

with

$$g(\omega) = e^{i(\phi_{os} - \frac{|n|\pi}{2} - \frac{\pi}{4})} \Psi_n(k_x) J_{|n|}(az_o K) \sqrt{\frac{2}{\pi a(y/r_T)K}} \quad (5.15)$$

where $y/r_T = z$.

According to the method of stationary phase (see, for example, Jeffreys and Jeffreys, Methods of Mathematical Physics, Cambridge University Press), the integral in Equation 5.14 has the following value in the limit as $\hat{R} \rightarrow \infty$

$$I_{n,k}^+ \rightarrow \sqrt{\frac{2\pi}{|\hat{R}h''(\omega_o)|}} g(\omega_o) e^{i[\hat{R}h(\omega_o) \pm \frac{\pi}{4}]} \quad (5.16)$$

where ω_o is the stationary phase point given by $h'(\omega_o) = 0$ and the \pm sign goes as the sign of $h''(\omega_o)$.

After some straightforward but tedious manipulations, the stationary phase point is found to be

$$\omega_o = \frac{n+q}{1 - M_x \cos\theta} \quad (5.17)$$

and the quantities needed to evaluate $I_{n,k}^+$ in terms of the tip rotational Mach number M_T are

$$aK(\omega_o) = \frac{(n+q)M_T \sin\theta}{1-M_x \cos\theta} \quad (5.18)$$

$$h(\omega_o) = (n+q)M_T \quad (5.19)$$

$$h''(\omega_o) = -\frac{M_T(1-M_x \cos\theta)^3}{(n+q)M_x^2 \sin^2\theta} < 0 \quad (5.20)$$

so that the integral is found to be

$$I_{n,k}^+ = \frac{-i \sin\theta}{a \frac{y}{D} (1-M_x \cos\theta)} e^{i[(n+q)\frac{\Omega r}{c_o} - \frac{|n|\pi}{2}]} e^{i\phi_{os}} \times \Psi_n(k_x) J_{|n|}[az_o K(\omega_o)] \quad (5.21)$$

For the case where $n+q < 0$, we pick up the derivation at Equation 5.9 with the substitution for the Hankel function of the second kind

$$H_n^{(2)}(y) \rightarrow \sqrt{\frac{2}{\pi y}} e^{-i(y - \frac{n\pi}{2} - \frac{\pi}{4})} \quad (5.22)$$

into Equation 5.5. The stationary phase derivation leads to the same results as in Equations 5.17 - 5.20 with the exception of a sign change in Equation 5.18 and a $>$ sign in Equation 5.20. The result is that a combined form can be written for both I's:

$$I_{n,k} = \frac{-i \sin\theta}{a \frac{y}{D} (1-M_x \cos\theta)} e^{i[(n+q)\frac{\Omega r}{c_o} - \text{sign}(n+q)\frac{|n|\pi}{2}]} e^{i\phi_{os}} \times \Psi_n(k_x) J_{|n|} \left[\frac{|n+q|z_o M_T \sin\theta}{1-M_x \cos\theta} \right] \quad (5.23)$$

Substitution into Equation 5.2 gives the general far field pressure harmonic for all $n+q$ as follows.

$$P_{n,k} = \frac{-\rho_o c_o^2 B \sin\theta e^{i[(n+q)\frac{\Omega r}{c_o} - \text{sign}(n+q)\frac{|n|\pi}{2}]}}{8\pi \frac{y}{D} (1-M_x \cos\theta)} \times \int_{z_h}^1 M_T^2 e^{i\phi_{os}} \Psi_n(k_x) J_{|n|} \left[\frac{|n+q|z_o M_T \sin\theta}{1-M_x \cos\theta} \right] dz_o \quad (5.24)$$

where the wavenumbers are

$$k_x = \frac{2a}{\sigma_o} \left(\frac{n+q}{1-M_x \cos\theta} - q \right) B_D \quad (5.25)$$

$$k_y = \frac{-2}{z_o \sigma_o} \left[\frac{a^2 z_o^2 (n+q) M_x \cos\theta}{1-M_x \cos\theta} - n \right] B_D \quad (5.26)$$

and in $\phi_{os} = \phi_{FA} + \phi_s$, the phase lags due to offset and sweep are

$$\phi_{FA} = \frac{2}{z_0 \sigma_0} \left[\frac{a^2 z_0^2 (n+q) M_x \cos \theta}{1 - M_x \cos \theta} - n \right] \frac{FA}{D} \quad (5.27)$$

$$\phi_s = \frac{2a}{\sigma_0} \left(\frac{n+q}{1 - M_x \cos \theta} - q \right) \frac{MCA}{D} \quad (5.28)$$

At the end of Section 3, a discussion was devoted to establishing that

$$P_{-m, -k} = P_{n, k}^* \quad (5.29)$$

to verify that the equation derived for the pressure caused by a real blade loading is real and so that formulas for folding one of the sums in Equation 5.1 could be established. Here, we want to verify that this property has been correctly preserved in the passage to the far field. To accomplish this, first note from Equations 3.93 - 95 that, when m and k change sign, so do n and q . Also, in Section 3 it was shown that $\Psi_{-n} = \Psi_n^*$. Then, since ϕ_{os} changes sign with n and q , it is clear that Equation 5.29 holds. Furthermore, it can be seen when $P_{n, k}$ is substituted into Equation 5.1 for the radiated pressure field, that the exponential

$$e^{i(n+q)\frac{n}{c_0}(r - c_0 t)} \quad (5.30)$$

appears for all n and q . This is the required behavior representing outgoing waves for every harmonic mode.

Equation 5.24 is the general expression for the far field pressure harmonic in terms of the general mode index n and the frequency ratio q . To predict waveforms, $P_{n, k}$ can be used either in Equation 5.1 or in Equation 3.122, which is repeated here for convenience.

$$p_2(t) = P_{0,0} + 2 \times \text{R.P.} \sum_{m=1}^{\infty} P_{n,0} e^{imB(\phi - \Omega t)} + 2 \times \text{R.P.} \sum_{m=-\infty}^{\infty} \sum_{k=1}^{\infty} P_{n,k} e^{i[n\phi - (n+q)\Omega t]} \quad (5.31)$$

In the next sections, radiation formulas are displayed explicitly in terms of rotor blade numbers and speeds via the substitutions in Equations 3.93 - 95.

Thickness and Steady Non-Radial Loading

For this case k and q are 0 and we need only the second term from Equation 5.31:

$$p_2(t) = 2 \times \text{R.P.} \sum_{m=1}^{\infty} P_m e^{imB(\phi - \Omega t)} \quad (5.32)$$

where the harmonic $P_m = P_{n,0}$ is

$$P_m = \frac{-\rho_o c_o^2 B \sin \theta e^{imB[\frac{\Omega r}{c_o} - \frac{\pi}{2}]}}{8\pi \frac{y}{D} (1 - M_x \cos \theta)} \times \int_{z_h}^1 M_r^2 e^{i\phi_{os}} \Psi_{mB}(k_x) J_{mB} \left[\frac{mBz_o M_r \sin \theta}{1 - M_x \cos \theta} \right] dz_o \quad (5.33)$$

and the source term is

$$\Psi_{mB} = k_x^2 t_b \Psi_v + \frac{i}{2} [k_x C_D \Psi_D + k_y C_L \Psi_L] \quad (5.34)$$

The x and y wavenumbers are

$$k_x = \frac{2a}{\sigma_o} \frac{mB}{1 - M_x \cos \theta} B_D \quad (5.35)$$

$$k_y = \frac{2mB}{z_o \sigma_o} \left[\frac{1 - \sigma_o^2 M_x \cos \theta}{1 - M_x \cos \theta} \right] B_D \quad (5.36)$$

and the phase lags due to sweep and offset in $\phi_{os} = \phi_{FA} + \phi_s$ are

$$\phi_s = \frac{2a}{\sigma_o} \frac{mB}{1 - M_x \cos \theta} \frac{MCA}{D} \quad (5.37)$$

$$\phi_{FA} = - \frac{2mB}{z_o \sigma_o} \left[\frac{1 - \sigma_o^2 M_x \cos \theta}{1 - M_x \cos \theta} \right] \frac{FA}{D} \quad (5.38)$$

These are equivalent to the far field formulas originally presented in References 11 and 12. Note, however, that there has been a change in sign in the definition of k_y . This is a change in sign convention only, not an error. In the references just mentioned there was considerable discussion of the effect of geometry, including particularly sweep, on noise.

Radial Loading - Steady and Unsteady

Theory for this loading term was presented by the author in Reference 26 for steady loading only. The general unsteady loading harmonic can be written down immediately from Equation 5.1 and 3.98 in which the radial source component of $\Psi_{n,k}$ is

$$B_D \hat{\Psi}_{rk}(k_x) \frac{\partial}{\partial z_o}(\cdot) \quad (5.39)$$

which acts on the Bessel function, symbolized by the empty parentheses. When this is inserted into Equation 5.24, the pressure harmonic is found to be

$$P_{n,k} = \frac{-\rho_o c_o^2 B \sin \theta e^{i[(n+q)\frac{\Omega r}{c_o} - \text{sign}(n+q)\frac{|n|\pi}{2}]}}{8\pi \frac{Y}{D}(1-M_x \cos \theta)} \times \int_{z_h}^1 M_r^2 e^{i\phi_{os}} B_D \hat{\Psi}_{rk}(k_x) \left[\frac{|n+q|M_T \sin \theta}{1-M_x \cos \theta} \right] J'_{|n|} \left[\frac{|n+q|z_o M_T \sin \theta}{1-M_x \cos \theta} \right] dz_o \quad (5.40)$$

This has never been coded because unsteadiness in the radial loading source has not been evaluated. However, for the steady effect, the result can be written down immediately:

$$P_m = \frac{-\rho_o c_o^2 B \sin \theta e^{imB[\frac{\Omega r}{c_o} - \frac{\pi}{2}]}}{8\pi \frac{Y}{D}(1-M_x \cos \theta)} \times \int_{z_h}^1 M_r^2 e^{i\phi_{os}} M_r k_x \sin \theta (1/2) \hat{\Psi}_r(k_x) J'_{mB} \left[\frac{mBz_o M_T \sin \theta}{1-M_x \cos \theta} \right] dz_o \quad (5.41)$$

Up to this point in the derivation, $\hat{\Psi}_r$ has represented a radial force distributed over the blade surface. If now we say that the radial loading the source acts only at the tip, then $\hat{\Psi}_r$ can be replaced as follows

$$\hat{\Psi}_r = \delta(r_o - r_T) C_R r_T \Psi_r = \delta(z_o - 1) C_R \Psi_r \quad (5.42)$$

C_R is a coefficient of radial force defined on the next page. When Equation 5.42 is substituted into Equation 5.41, the result is

$$P_m = \frac{-\rho_o c_o^2 B \sin \theta e^{imB[\frac{\Omega r}{c_o} - \frac{\pi}{2}]}}{8\pi \frac{Y}{D}(1-M_x \cos \theta)} \times M_r^2 e^{i\phi_{os}} M_r k_x \sin \theta \frac{C_R}{2} \Psi_r(k_x) J'_{mB} \left[\frac{mB M_T \sin \theta}{1-M_x \cos \theta} \right] \quad (5.43)$$

where k_x and k_y and the ϕ 's are the same as in the preceding section. This formula was presented in Reference 26 in conjunction with discussions of the radial loading associated with formation of a tip vortex.

In Equation 5.43, the interpretations of C_R and Ψ_r are as follows. Say that $s(\gamma_o)$ is the radial force per unit length distributed along the tip chord line. Chordwise distance is measured approximately here along the helical advance coordinate γ_o , which was used in Section 3. The radial force coefficient C_R is defined according to

$$s(\gamma_o) = (\rho_o U_T^2 / 2) r_T S[(\gamma_o - \text{MCA}) / b] C_R \quad (5.44)$$

where MCA is the mid chord alignment, or sweep, at the tip. The function S gives the shape of the chordwise distribution and is normalized to unit area according to

$$\int_{\text{chord}} S(\gamma_o / b) d(\gamma_o / b) = 1 \quad (5.45)$$

Thus, the integrated radial force is $(\rho_o U_T^2 / 2) b r_T C_R$ where U_T is the tip helical speed.

Unsteady Loading - Non-Radial

In this section, formulas are presented for calculation of noise caused by interaction of a rotor with the unsteady flow field of another rotor or with a fixed (non-rotating) distortion pattern. The 3 cases treated are the same as those in Section 4 for near-field noise. These are given by Equation 5.1 and 5.24 with q , k , and n specified by Equations 3.93 - 95 and the non-radial source term $\Psi_{n,k} \rightarrow i\Psi_{Fk}$. As in Section 4, the reader is reminded that this report deals with the counter-rotation problem only up to the point of computing unsteady loading and noise caused by specified non-uniform inflow. The means to compute the non-uniform inflow from wakes of an upstream rotor or other flow field distortion are not included herein.

General Counter-Rotation Case

$$p_2(t) = \sum_{m=-\infty}^{\infty} \sum_{k=-\infty}^{\infty} P_{n,k} e^{i[(mB_2 - kB_1)\phi - (mB_2 + kB_1\Omega_{12})\Omega_2 t]} \quad (5.46)$$

where the rotor speed ratio $\Omega_{12} = \Omega_1/\Omega_2$ and

$$P_{n,k} = \frac{-i\rho_o c_o^2 B_2 \sin\theta e^{i[(mB_2 + kB_1\Omega_{12})\frac{\Omega r}{c_o} - \text{sign}(mB_2 + kB_1\Omega_{12})|mB_2 - kB_1|\pi/2]}}{8\pi \frac{Y}{D} (1 - M_x \cos\theta)} \times \int_{z_h}^1 M_r^2 e^{i\phi_{os}} \Psi_{Fk}(k_x) J_{|mB_2 - kB_1|} \left[\frac{|mB_2 + kB_1\Omega_{12}| z_o M_T \sin\theta}{1 - M_x \cos\theta} \right] dz_o \quad (5.47)$$

$$\Psi_{Fk}(k_x) = \frac{1}{2} [k_y C_{Lk} \Psi_{Lk}(k_x) + k_x C_{Dk} \Psi_{Dk}(k_x)] \quad (5.48)$$

and
$$k_x = \frac{2a}{\sigma_o} \left[\frac{mB_2 + kB_1\Omega_{12}}{1 - M_x \cos\theta} - kB_1(1 + \Omega_{12}) \right] B_D \quad (5.49)$$

$$k_y = \frac{-2}{z_o \sigma_o} \left[\frac{a^2 z_o^2 (mB_2 + kB_1\Omega_{12}) M_x \cos\theta}{1 - M_x \cos\theta} - (mB_2 - kB_1) \right] B_D \quad (5.50)$$

$$\phi_{FA} = \frac{2}{z_o \sigma_o} \left[\frac{a^2 z_o^2 (mB_2 + kB_1\Omega_{12}) M_x \cos\theta}{1 - M_x \cos\theta} - (mB_2 - kB_1) \right] \frac{FA}{D} \quad (5.51)$$

$$\phi_s = \frac{2a}{\sigma_o} \left[\frac{mB_2 + kB_1\Omega_{12}}{1 - M_x \cos\theta} - kB_1(1 + \Omega_{12}) \right] \frac{MCA}{D} \quad (5.52)$$

From the form of Equation 5.46, it can be seen that sound harmonics appear at frequencies $(mB_2\Omega_2 + kB_1\Omega_1)/2\pi$ where m and k take on all integer values. For the steady loading case, these formulas reduce exactly to those in Equations 5.32 through 5.38 by taking $k=0$ only. Also, by the use of the formulas $J_{-n}(z) = (-1)^n J_n(z)$ and $J_n(-z) = (-1)^n J_n(z)$, Equation 5.47 can be shown to be equivalent to the forms given in various AIAA papers by Hanson (eg. reference 14), which do not employ the absolute value signs on the mode order and Bessel function arguments.

Special Case - Equal Blade Numbers and Equal RPM's

In this case we can set $\Omega_1 = \Omega_2 = \Omega$, $B_1 = B_2 = B$. Then, by shifting the origin of the m series and substituting $mB\omega$ for ω , the pressure is found to be

$$p_2(t) = \sum_{m=-\infty}^{\infty} \sum_{k=-\infty}^{\infty} P_{n,k} e^{i[(m-2k)B\phi - mB\Omega t]} \quad (5.53)$$

$$P_{n,k} = \frac{-i\rho_o c_o^2 B \sin\theta e^{i\left[\frac{mB\Omega r}{c_o} - \text{sign}(m)|m-2k|\pi B/2\right]}}{8\pi \frac{Y}{D} (1-M_x \cos\theta)} \times \int_{z_h}^1 M_r^2 e^{i\phi_{os}} \Psi_{FK}(k_x) J_{|m-2k|B} \left[\frac{|m|Bz_o M_T \sin\theta}{1-M_x \cos\theta} \right] dz_o \quad (5.54)$$

$$\Psi_{FK}(k_x) = \frac{1}{2} [k_y C_{Lk} \Psi_{Lk}(k_x) + k_x C_{Dk} \Psi_{Dk}(k_x)] \quad (5.55)$$

and

$$k_x = \frac{2a}{\sigma_o} \left(\frac{mB}{1-M_x \cos\theta} - 2kB \right) B_D \quad (5.56)$$

$$k_y = \frac{-2}{z_o \sigma_o} \left[\frac{mB(\sigma_o^2 M_x \cos\theta - 1)}{1-M_x \cos\theta} + 2kB \right] B_D \quad (5.57)$$

$$\phi_{FA} = \frac{2}{z_o \sigma_o} \left[\frac{mB(\sigma_o^2 M_x \cos\theta - 1)}{1-M_x \cos\theta} + 2kB \right] \frac{FA}{D} \quad (5.58)$$

$$\phi_s = \frac{2a}{\sigma_o} \left(\frac{mB}{1-M_x \cos\theta} - 2kB \right) \frac{MCA}{D} \quad (5.59)$$

The frequencies sensed by the fuselage-fixed observer in this case are given by $mB\Omega$, i.e. harmonics of blade passing frequency. Thus, despite the counter-rotation interaction, the frequencies that appear are exactly the same as for a single rotation propeller or a fan with guide vanes. The main benefit of shifting the origin of the m summation is that the argument of the Bessel function becomes independent of k . This takes advantage of the fact that standard Bessel function subroutines return all orders of the function for a specified argument.

Special Case - Guide Vanes and Other Fixed Inflow Distortion

These results are obtained from the general formulas in Equations 5.46 to 5.52 by setting $B_2=B$, $\Omega_{12}=0$, and $B_1=1$. Thus, $n=mB-k$, $q=k$, and $n+q=mB$.

$$p_2(t) = \sum_{m=-\infty}^{\infty} \sum_{k=-\infty}^{\infty} P_{n,k} e^{i[(mB-k)\phi - mB\Omega t]} \quad (5.60)$$

$$P_{n,k} = \frac{-i\rho_o c_o^2 B \sin\theta e^{i\left[\frac{mB\Omega r}{c_o} - \text{sign}(m)|mB-k|\pi/2\right]}}{8\pi \frac{y}{D} (1-M_x \cos\theta)} \times \int_{z_h}^1 M_r^2 e^{i\phi_{os}} \Psi_{Fk}(k_x) J_{|mB-k|} \left[\frac{|m|Bz_o M_r \sin\theta}{1-M_x \cos\theta} \right] dz_o \quad (5.61)$$

$$\Psi_{Fk}(k_x) = \frac{1}{2} [k_y C_{Lk} \Psi_{Lk}(k_x) + k_x C_{Dk} \Psi_{Dk}(k_x)] \quad (5.62)$$

and

$$k_x = \frac{2a}{\sigma_o} \left(\frac{mB}{1-M_x \cos\theta} - k \right) B_D \quad (5.63)$$

$$k_y = \frac{-2}{z_o \sigma_o} \left[\frac{mB(\sigma_o^2 M_x \cos\theta - 1)}{1-M_x \cos\theta} + k \right] B_D \quad (5.64)$$

$$\phi_{FA} = \frac{2}{z_o \sigma_o} \left[\frac{mB(\sigma_o^2 M_x \cos\theta - 1)}{1-M_x \cos\theta} + k \right] \frac{FA}{D} \quad (5.65)$$

$$\phi_s = \frac{2a}{\sigma_o} \left(\frac{mB}{1-M_x \cos\theta} - k \right) \frac{MCA}{D} \quad (5.66)$$

The formulas above apply to the general fixed inflow distortion case where all of the loading harmonics are generated. For the guide vane case, replace k everywhere by kV , where V is the number of inlet or exit guide vanes (not to be confused with V used for velocity elsewhere in this report). Again, note that the only frequencies are given by $mB\Omega$, i.e. BPF and multiples.

SECTION 6

SOUND POWER AND WAVE DRAG

Sound power radiated from a propeller might be of interest as an overall measure of the effect of geometry changes on noise. However, because of the subjective nature of noise, this is a somewhat academic application. A more practical application is in the area of performance. Sound power is related to wave drag. Consider the sketch in Figure 9 showing a propeller in flight surrounded by a cylindrical surface S . The surface S comprising 2 discs, S_1 and S_3 , and the curved surface, S_2 the curved surface, S_2 is reminiscent of figures used in aerodynamics text books for pressure drag analysis (e.g. Ashley and Landahl (ref. 27, page 174). The momentum flux through S_2 corresponds to radiating energy and wave drag; the flux through S_3 is related to energy in the trailing vortex system and is used to compute vortex drag. (Other names for vortex drag are drag-due-to-lift and induced drag.) In this section, we derive the formula for sound power (or wave power) passing through S_2 and compare it to the shaft power. We also examine the spectrum of sound power and find that it is smeared in frequency bands centered on the blade passing harmonics, as would be expected from Doppler considerations. The width of the bands increases with flight Mach number.

The derivation herein is an extension of the analysis in chapter 11 of Morse and Ingard's book (ref.28) which deals with power from oscillating point dipoles in straight line motion. In the present analysis, the cylindrical surface S_2 of radius r is constructed with its axis coincident with the propeller axis and flight path. The sound power Π is the integral over the surface of the radial component of the acoustic energy flux averaged over time:

$$\Pi = \int_{-\infty}^{\infty} \int_0^{2\pi} \frac{1}{T} \int_0^T p u_r dt r d\phi dx \quad (6.1)$$

where u_r is the radial velocity component which will be obtained from the acoustic pressure p via the momentum equation. The averaging time T need not be specified, since it will be found to drop out of the analysis. An important feature of the Morse and Ingard analysis is that Equation 6.1 is written in the fluid-fixed coordinate system, removing ambiguities in the interpretation of sound power that could be introduced by using moving coordinates. This approach is retained in the present analysis.

To evaluate Equation 6.1, we obtain a suitable expression for p , then derive an expression for u_r from it, and finally perform the ϕ , x , and t integrations analytically. The expression for pressure, obtained from Equations 3.96 with steady terms only and 4.2 is, for the observer translating with the propeller,

$$p(t) = \frac{-iaB\rho_o c_o^2}{8\pi} \sum_{m=-\infty}^{\infty} e^{imB(\phi - \Omega t)} \int_{z_h}^1 M_r^2 \int_{-\infty}^{\infty} e^{i\phi_{os}} e^{i\phi_x} \Psi_{mB}(k_x) J_{mB}(az_o K) H_{mB}^{(1)}(azK) d\omega dz_o \quad (6.2)$$

where

$$\phi_x = a(\omega - mB) \frac{x_1}{r_T} \quad (6.3)$$

$$K = \sqrt{M_x^2 \omega^2 - (\omega - mB)^2} \quad (6.4)$$

$$\Psi_{mB} = k_x^2 t_b \Psi_v + \frac{i}{2} [k_y C_L \Psi_L + k_x C_D \Psi_D] \quad (6.5)$$

The wavenumbers are

$$k_x = \frac{2a\omega}{\sigma_o} B_D \quad (6.6)$$

$$k_y = \frac{2}{z_o\sigma_o} (-a^2 z_o^2 \omega + mB\sigma_o^2) B_D \quad (6.7)$$

and in $\phi_{os} = \phi_{FA} + \phi_s$ the phase lags due to offset and sweep are

$$\phi_{FA} = \frac{2}{z_o\sigma_o} (a^2 z_o^2 \omega - mB\sigma_o^2) \frac{FA}{D} \quad (6.8)$$

$$\phi_s = \frac{2a\omega}{\sigma_o} \frac{MCA}{D} \quad (6.9)$$

The Hankel function

$$H_{mB}^{(1)}(azK) = \begin{cases} H_{mB}^{(1)}(az|K|) & \text{for } m > 0 \\ -H_{mB}^{(2)}(az|K|) & \text{for } m < 0 \end{cases} \quad (6.10)$$

To return to the fluid-fixed coordinate system, we simply substitute $x_1 = x - Vt$ as was discussed in conjunction with Equation 3.46. In the new expression for pressure, we also split the upper and lower halves of the series so that the Hankel functions can be displayed explicitly.

$$p(t) = \frac{-iaB\rho_o c_o^2}{8\pi} \left\{ \sum_{m=1}^{\infty} e^{imB\phi} \int_{M_r^2}^{\omega_2} e^{i\phi_{os}} e^{i[a(\omega-mB)\frac{x}{r_T} - \omega\Omega t]} \Psi_{mB} J_{mB} H_{mB}^{(1)} d\omega dz_o \right. \\ \left. - \sum_{m=-1}^{-\infty} e^{imB\phi} \int_{M_r^2}^{\omega_1} e^{i\phi_{os}} e^{i[a(\omega-mB)\frac{x}{r_T} - \omega\Omega t]} \Psi_{mB} J_{mB} H_{mB}^{(2)} d\omega dz_o \right\} \quad (6.11)$$

where the wavenumber integration is restricted to the range corresponding to radiating waves via

$$\omega_1 = \frac{mB}{1+M_x} \quad \text{and} \quad \omega_2 = \frac{mB}{1-M_x} \quad (6.12)$$

The second series can be rewritten by substituting m for $-m$ and ω for $-\omega$ with the result

$$p(t) = \frac{-iaB\rho_o c_o^2}{8\pi} \left\{ \sum_{m=1}^{\infty} e^{imB\phi} \int_{M_r^2}^{\omega_2} e^{i\phi_{os}} e^{i[a(\omega-mB)\frac{x}{r_T} - \omega\Omega t]} \Psi_{mB} J_{mB} H_{mB}^{(1)} d\omega dz_o \right. \\ \left. - \sum_{m=1}^{\infty} e^{-imB\phi} \int_{M_r^2}^{\omega_1} e^{-i\phi_{os}} e^{-i[a(\omega-mB)\frac{x}{r_T} - \omega\Omega t]} \Psi_{mB}^* J_{mB} H_{mB}^{(2)} d\omega dz_o \right\} \quad (6.13)$$

The negative Bessel function orders are eliminated because Bessel functions and Hankel functions are odd in order. Also, the source transform with negative argument and index results in the complex conjugate, as shown.

To find the corresponding form for the radial component of velocity, we integrate the linearized momentum equation

$$\rho_o \frac{\partial u_r}{\partial t} = - \frac{\partial p}{\partial r} \quad (6.14)$$

with the result

$$u_r = \frac{-1}{\rho_o r_T} \int \frac{\partial p}{\partial z} dt \quad (6.15)$$

Since z appears only in the Hankel function and t appears only in an exponential, the operations are easily performed on Equation 6.13 to obtain the working form for the radial velocity:

$$u_r(t) = \frac{-Bc_o}{8\pi M_x} \left\{ \sum_{m=1}^{\infty} e^{imB\phi} \int_{M_r^2}^{w_2} \int_{w_1}^{w_2} e^{i\phi_{os}} e^{i[a(\omega-mB)\frac{x}{r_T}-\omega\Omega t]} \frac{1}{\omega} \Psi_{mB} J_{mB} \frac{\partial}{\partial z} H_{mB}^{(1)} d\omega dz_o \right. \\ \left. + \sum_{m=1}^{\infty} e^{-imB\phi} \int_{M_r^2}^{w_2} \int_{w_1}^{w_2} e^{-i\phi_{os}} e^{-i[a(\omega-mB)\frac{x}{r_T}-\omega\Omega t]} \frac{1}{\omega} \Psi_{mB}^* J_{mB} \frac{\partial}{\partial z} H_{mB}^{(2)} d\omega dz_o \right\} \quad (6.16)$$

We are now prepared to perform the integration in Equation 6.1 using Equation 6.13 for p and Equation 6.16 for u_r . To keep the m 's and ω 's separate, we place primes on m and ω in the equation for u_r . We also adopt a special notation of P 's and U 's that combine the constants plus all of the terms under each integral except for the exponentials. With this shorthand, the power can be written

$$\Pi = \frac{1}{T} \int_0^T \int_{-\infty}^{\infty} \int_0^{2\pi} \left\{ \left[\sum_{m=1}^{\infty} e^{imB\phi} \iint P_m^{(1)}(\omega, z_o) e^{i[a(\omega-mB)\frac{x}{r_T}-\omega\Omega t]} d\omega dz_o \right. \right. \\ \left. \left. - \sum_{m=1}^{\infty} e^{-imB\phi} \iint P_m^{(2)}(\omega, z_o) e^{-i[a(\omega-mB)\frac{x}{r_T}-\omega\Omega t]} d\omega dz_o \right] \right. \\ \left. \times \left[\sum_{m=1}^{\infty} e^{im'B\phi} \iint U_{m'}^{(1)}(\omega', z_o) e^{i[a(\omega'-m'B)\frac{x}{r_T}-\omega'\Omega t]} d\omega' dz_o \right. \right. \\ \left. \left. + \sum_{m=1}^{\infty} e^{-im'B\phi} \iint U_{m'}^{(2)}(\omega', z_o) e^{-i[a(\omega'-m'B)\frac{x}{r_T}-\omega'\Omega t]} d\omega' dz_o \right] \right\} r d\phi dx dt \quad (6.17)$$

The integrand is the product of 2 series in the first square brackets and 2 more series in the second square brackets. When these are multiplied, 4 terms result. For the ϕ integration, the product of the first series from each pair produces

$$\int_0^{2\pi} e^{i(m+m')\phi} d\phi \quad (6.18)$$

which is 0 since both m and m' take on only positive values. The same remark applies to the product of the second series from each pair. However, for the cross term, we have

$$\int_0^{2\pi} e^{i(m-m')\phi} d\phi \quad (6.19)$$

This is 2π for $m'=m$ and 0 otherwise. With this integration completed and the summations simplified, we find

$$\begin{aligned} \Pi = \frac{2\pi r}{T} \int_0^T \int_{-\infty}^{\infty} \sum_{m=1}^{\infty} \left\{ \left[\iint P_m^{(1)}(\omega, z_0) e^{i(a\omega \frac{x}{r_T} - \omega \Omega t)} d\omega dz_0 \right] \left[\iint U_m^{(2)}(\omega', z_0) e^{-i(a\omega' \frac{x}{r_T} - \omega' \Omega t)} d\omega' dz_0 \right] \right. \\ \left. - \left[\iint P_m^{(2)}(\omega, z_0) e^{-i(a\omega \frac{x}{r_T} - \omega \Omega t)} d\omega dz_0 \right] \left[\iint U_m^{(1)}(\omega', z_0) e^{i(a\omega' \frac{x}{r_T} - \omega' \Omega t)} d\omega' dz_0 \right] \right\} dx dt \end{aligned} \quad (6.20)$$

This can be rearranged by moving the ω integrals outside the z_0 integrals and moving the x integration inside:

$$\begin{aligned} \Pi = \frac{2\pi r}{T} \int_0^T \sum_{m=1}^{\infty} \left\{ \iint \int_{-\infty}^{\infty} e^{ia(\omega - \omega') \frac{x}{r_T}} dx e^{-i(\omega - \omega') \Omega t} \left[\int P_m^{(1)}(\omega, z_0) dz_0 \right] \left[\int U_m^{(2)}(\omega', z_0) dz_0 \right] d\omega d\omega' \right. \\ \left. - \iint \int_{-\infty}^{\infty} e^{-ia(\omega - \omega') \frac{x}{r_T}} dx e^{i(\omega - \omega') \Omega t} \left[\int P_m^{(2)}(\omega, z_0) dz_0 \right] \left[\int U_m^{(1)}(\omega', z_0) dz_0 \right] d\omega d\omega' \right\} dt \end{aligned} \quad (6.21)$$

The x integrations each yield $(2\pi r_T/a)\delta(\omega - \omega')$ so that the ω' integration becomes trivial. Furthermore, the integrand is then time independent so that the time integration $(1/T) \int dt = 1$ and we now have

$$\begin{aligned} \Pi = \frac{4\pi^2 r r_T}{a} \sum_{m=1}^{\infty} \left\{ \int_{\omega_1}^{\omega_2} \left[\int P_m^{(1)}(\omega, z_0) dz_0 \right] \left[\int U_m^{(2)}(\omega, z_0) dz_0 \right] d\omega \right. \\ \left. - \int_{\omega_1}^{\omega_2} \left[\int P_m^{(2)}(\omega, z_0) dz_0 \right] \left[\int U_m^{(1)}(\omega, z_0) dz_0 \right] d\omega \right\} \end{aligned} \quad (6.22)$$

We can now return to the original notation, eliminating the P's and U's:

$$\begin{aligned} \Pi = \frac{i\rho_0 c_0^3 B^2 r r_T}{16M_x} \sum_{m=1}^{\infty} \int_{\omega_1}^{\omega_2} \frac{1}{\omega} \left\{ H_{mB}^{(1)} \frac{\partial}{\partial z} H_{mB}^{(2)} \left[\int M_r^2 e^{i\phi} \Psi_{mB} J_{mB} dz_0 \right] \left[\int M_r^2 e^{-i\phi} \Psi_{mB}^* J_{mB} dz_0 \right] \right. \\ \left. - H_{mB}^{(2)} \frac{\partial}{\partial z} H_{mB}^{(1)} \left[\int M_r^2 e^{-i\phi} \Psi_{mB}^* J_{mB} dz_0 \right] \left[\int M_r^2 e^{i\phi} \Psi_{mB} J_{mB} dz_0 \right] \right\} d\omega \end{aligned} \quad (6.23)$$

At the analogous point in the Morse and Ingard derivation for translating point dipoles, asymptotic forms for the Hankel functions were used to pass to the far field. However, this is not necessary if we note that the Hankel functions appear in a combination that can be evaluated using the Wronskian relationship

$$\begin{aligned} W[H_n^{(1)}(x), H_n^{(2)}(x)] &= H_n^{(1)}(x) \frac{\partial}{\partial x} H_n^{(2)}(x) - H_n^{(2)}(x) \frac{\partial}{\partial x} H_n^{(1)}(x) \\ &= \frac{-4i}{\pi x} \end{aligned} \quad (6.24)$$

The final result for sound power is

$$\Pi = \frac{\rho_o c_o^3 B^2 r_T^2}{4\pi M_x} \sum_{m=1}^{\infty} \int_{\omega_1}^{\omega_2} \frac{1}{\omega} \left| \int_{z_h}^1 M_r^2 e^{i\phi} \sigma_{\Psi_{mB}}(k_x) J_{mB}(az_o K) dz_o \right|^2 d\omega \quad (6.25)$$

After a somewhat complex derivation, this is a remarkably simple result. The formula is easily programmed and can be evaluated quickly even on personal computers, if desired.

Various reference powers or normalization schemes could be used for the sound power in Equation 6.25. However, since the prime motivation for investigating sound power has been to understand its relation to performance, it makes sense to use the same reference as in the definition of propeller (shaft) power coefficient:

$$C_P = \frac{SHP}{\rho_o N^3 D^5} \quad (6.26)$$

Thus, the coefficient of sound power becomes

$$C_{SP} = \frac{\Pi}{\rho_o N^3 D^5} \quad (6.27)$$

With this definition, we have

$$C_{SP} = \frac{\pi^2 B^2}{16a^3} \sum_{m=1}^{\infty} \int_{\omega_1}^{\omega_2} \frac{1}{\omega} \left| \int_{z_h}^1 \sigma_o^2 e^{i\phi} \sigma_{\Psi_{mB}}(k_x) J_{mB}(az_o K) dz_o \right|^2 d\omega \quad (6.28)$$

This can be compared with shaft power coefficients, which are typically of order 1.

Equation 6.25 is in an undesirable form for calculations for low flight Mach number, i.e. as $M_x \rightarrow 0$. A simple change of variables can be used to provide a suitable form and, at the same time, serve as a partial verification of the power formula. If the substitution

$$\omega = \frac{mB}{1 - M_x \cos \theta} \quad (6.29)$$

is made, we find that

$$K = \frac{mB M_x \sin \theta}{1 - M_x \cos \theta} \quad (6.30)$$

which approaches $mB M_x \sin \theta$ as $M_x \rightarrow 0$. Thus, the Bessel function argument

$$az_o K \rightarrow mB z_o M_x \sin \theta \quad (6.31)$$

For small M_x , the differential

$$d\omega \rightarrow -mBM_x \sin\theta \, d\theta \quad (6.32)$$

in which the M_x cancels the $1/M_x$ in the constant of Equation 6.25. The integration limits ω_1 and ω_2 become π and 0. Thus, with the substitution for ω , the expression for sound power at low Mach number becomes

$$\Pi = \frac{\rho_o c_o^3 B^2 r_T^2 M_T^4}{4\pi} \sum_{m=1}^{\infty} \int_0^{\pi} \left| \int_{z_h}^1 z_o^2 \Psi_{mB} e^{i\phi_{os}} J_{mB}(mBz_o M_T \sin\theta) \, dz_o \right|^2 \sin\theta \, d\theta \quad (6.33)$$

Mach number cancels from the expression at low Mach number, and the integrals are obviously finite.

To check the above result, we have used the expression from elementary acoustics books for sound power of stationary sources

$$\Pi = \frac{1}{\rho_o c_o} \int_0^{2\pi} \int_0^{\pi} \overline{p^2} \, r^2 \sin\theta \, d\theta \, d\phi \quad (6.34)$$

where p is the far-field pressure and the overbar denotes the time average. The reader can verify that, when Equation 5.33 with $M_x=0$ is substituted for p , Equation 6.33 is the result. This is not a complete verification of the general results of this section, but it does provide some confidence that the algebra was done correctly.

SECTION 7

DOWNWASH EQUATIONS FOR AIRLOAD CALCULATION

This is the first of several sections on theory for aerodynamic blade loading and propeller performance. The main task of this section is to develop an equation giving steady or unsteady downwash at the blade lifting surfaces as an integral of the blade loading in the form of a standard lifting surface kernel function equation:

$$\frac{w}{V} = \alpha(x,y) = \iint \Delta C_p(x_o, y_o) K(x,y; x_o, y_o) dx_o dy_o \quad (7.1)$$

Here ΔC_p is the coefficient of lift pressure, which is to be found, and α is the downwash angle, which must match the known angle between the blade camber surface and the blade section advance direction. In the lifting surface context, lift is that force component acting normal to the local blade section advance direction in analogy with wing methods. This is distinct from the system used in lifting line methods where the equivalent 2-dimensional lift vector is tilted back by the induced flow angle. K is the kernel function giving the downwash per unit loading. It has various forms depending on the problem being solved. For subsonic wings the well known kernel is

$$K = \frac{1}{8\pi(y-y_o)^2} \left[1 + \frac{x-x_o}{\sqrt{(x-x_o)^2 + \beta^2(y-y_o)^2}} \right] \quad (7.2)$$

x_o and y_o are the streamwise and transverse source coordinates in the wing surface and x and y are the corresponding field point coordinates. Equation 7.2 and its supersonic counterpart are presented in Reference 4 with a discussion of application methods. The propeller kernel is more complicated but is analogous in that 2 terms appear, one of which is independent of the streamwise coordinate and the other of which contains the streamwise coordinate and the compressibility effect (here via the β). Later sections show how these integral equations can be inverted to determine airloading as a function of the blade boundary conditions.

Acceleration Potential Method

The derivation of this section is an extension of the pressure potential method given in standard textbooks such as Bisplinghoff, Ashley, and Halfman (ref. 3). It is basically an integration of the momentum equation

$$\frac{Dv}{Dt} = \frac{1}{\rho} (\underline{F} - \nabla p) \quad (7.3)$$

which relates the disturbance pressure, body force, and velocity. Dv/Dt is the acceleration following a fluid particle. \underline{F} is the body force, which doesn't ordinarily enter in wing theory because the air particles pass over or under the wing. For propellers, the particles pass through the disc so that the role of the body force might seem different in this case. However, from the sketch in Figure 10 it can be seen that a particle whose acceleration is being integrated also passes over or under the blade, not through it. (The particle motion shown in the figure is shown as undeflected by the blade loading for simplicity. This undeflected path is also used for the integration described below.) Therefore, the body force is not needed if only the downwash is to be calculated. As with wing theory, the downwash

equations are not valid on the wake sheet, but can be evaluated in the limit as the field point approaches the sheet. For a complete treatment of the propeller theory, the body force is useful in finding the axial induction and relating it to classical propeller momentum theory. It also helps in interpreting the above-mentioned limiting process and therefore is included in the analysis.

Our use of Equation 7.3 involves linearization at various points in the derivation. First, we will use an expression for the disturbance pressure derived in Section 3 based on the linear wave equation. Second, the density ρ is set equal to its ambient value ρ_0 . This is justified because F and p are first order disturbance quantities. Perturbations of ρ would introduce second order quantities in the momentum equation. This is discussed more formally in Reference 3. Third, in the integration of Equation 7.3, the particle is followed along undisturbed streamlines as in wing methods and explained in the next paragraph. This is a good approximation for typical cruise conditions where the axial induction is small compared to the flight speed. However, for takeoff and climb conditions, the approximation is not acceptable and a non-linear modification must be made as explained in Section 8.

Integration of Equation 7.3 could proceed by using the expression for disturbance pressure given by Equations 3.96 and 3.97, taking its gradient, and performing the integral. However, it is more convenient to integrate the pressure and take its gradient afterwards. We write the functional dependence of the pressure as $p(x, r, \phi, t)$ in a coordinate system translating but not rotating with the propeller. (In this and following sections where we are dealing with propeller aerodynamics, as opposed to acoustics, the sign convention for x will be changed from that in the previous sections to positive downstream.) The quantity

$$\psi(x, r, \phi, t) = \frac{-1}{\rho_0} p(x, r, \phi, t) \quad (7.4)$$

is commonly called the acceleration or pressure potential. If we write Φ as the disturbance velocity potential, then

$$\frac{D}{Dt} \Phi(x, r, \phi, t) = \psi(x, r, \phi, t) \quad (7.5)$$

because taking the gradient of both sides returns Equation 7.3. The integration is from upstream infinity $(-\infty, r, \phi)$ to the field point (x, r, ϕ) occupied by the particle at time t . A dummy time variable τ is used for the integration to follow the particle. Thus, at any τ prior to t , the particle was located at $[x-V(t-\tau), r, \phi]$. The integral of Equation 7.5 is

$$\Phi(x, r, \phi, t) = \int_{-\infty}^t \psi(x-V(t-\tau), r, \phi, \tau) d\tau \quad (7.6)$$

The integration variable is changed from τ to $x' = x - V(t - \tau)$ so that

$$\Phi(x, r, \phi, t) = \frac{1}{V} \int_{-\infty}^x \psi(x', r, \phi, t - \frac{x-x'}{V}) dx' \quad (7.7)$$

Bringing the V out from under the integral is a significant linearization that will be modified in Section 8. Evaluation of Equation 7.7 and the associated downwash velocity comprises the remainder of this section.

Velocity Potential

From now on we will deal with only one loading harmonic at a time. The unsteady loading frequency is $q\Omega/2\pi$ and the harmonic loading index k gives the interblade phase angle $2\pi k/B$ as explained in conjunction with Equation 3.80. For the harmonic with index k , Equations 3.96 and 3.97 can be combined to give

$$p_k = \frac{aB\rho_o V^2}{8\pi} \sum_{m=-\infty}^{\infty} e^{i[n(\phi-\Omega t)-q\Omega t]} \int_{z_h}^1 \sigma_o^2 \int_{-\infty}^{\infty} e^{i\phi_{FA}} e^{i\phi_x} e^{i\phi_s} \Psi_{Fk}(k_x) J_n(az_{<}K) H_n^{(1)}(az_{>}K) d\omega dz_o \quad (7.8)$$

We are analyzing only the effect of the non-radial loading source so that the source transform $\Psi_{nk}=i\Psi_F$. Recall that the radial wavenumber is

$$K = \sqrt{M_x^2 \omega^2 - (\omega - n - q)^2} \quad (7.9)$$

where the branches of the square root are explained in conjunction with Equation 3.36. ϕ_{FA} is the phase lag associated with the offset or Face Alignment of the blade section at radius ratio z_o and ϕ_x is the phase associated with the axial position of the field point, which was given by Equation 3.106. However, with the new sign convention for axial position, this becomes

$$\phi_x = -a(\omega - n - q) \frac{x}{r_T} \quad (7.10)$$

In the harmonic summation, the effects of multiple blades and arbitrary interblade phase angle are accounted for by summing on m but recognizing that the mode order is

$$n = mB - k \quad (7.11)$$

as explained in Section 3.

At this point it is desirable to eliminate the source transform and return to a direct representation of the lift pressure in terms of the coefficient $\Delta C_p(\gamma_o, z_o)$, where γ_o is the coordinate measured along the section advance direction as shown in Figure 4. Within the linearization approximation, γ_o is also the chordwise distance variable. Since we are dealing with only the lift component of the blade force at this point, Equations 3.72 and 3.74 show that

$$\Psi_{Fk}(k_x) = \frac{1}{2} k_y C_{Lk} \int f_L(X) e^{ik_x X} dX \quad (7.12)$$

where the chordwise wavenumber is

$$k_x = \frac{2a(\omega - q)}{\sigma_o} B_D \quad (7.13)$$

X is the non-dimensional chordwise distance measured from mid-chord which can be returned to the γ_o system by Equation 3.58 to give

$$\Psi_{Fk} = \frac{1}{2} k_y \frac{r_T}{b} \int C_{Lk} f_L \left(\frac{\gamma_o - MCA}{b} \right) e^{i \frac{a(\omega - q)}{\sigma_o} \frac{\gamma_o}{b}} d \left(\frac{\gamma_o}{r_T} \right) e^{-i\phi_s} \quad (7.14)$$

If we define a new non-dimensional distance based on tip radius

$$\Gamma_o = \gamma_o / r_T \quad (7.15)$$

we find, recalling $C_{Lk} f_L = \Delta C_p$, that

$$\Psi_{FK}(k_x) e^{i\phi_s} = \frac{-1}{2z_o \sigma_o} K_{\xi 0} \int \Delta C_p(\gamma_o, z_o) e^{i \frac{a(\omega-q)}{\sigma_o} \Gamma_o} d\Gamma_o \quad (7.16)$$

We have defined a new wavenumber corresponding to k_y

$$K_{\xi 0} = (\omega - n - q) a^2 z_o^2 - n \quad (7.17)$$

and for future use we also define

$$K_{\xi} = (\omega - n - q) a^2 z^2 - n \quad (7.18)$$

$$\bar{K}_{\xi 0} = (-n - q) a^2 z_o^2 - n \quad (7.19)$$

and

$$\bar{K}_{\xi} = (-n - q) a^2 z^2 - n \quad (7.20)$$

Substitution of Equation 7.16 into 7.8 gives the final form for the pressure harmonic

$$p_k = \frac{-aB\rho_o V^2}{16\pi} \sum_{m=-\infty}^{\infty} e^{i[n(\phi - \Omega t) - q\Omega t]} \int_{z_h}^1 \int_{-\infty}^{\infty} \frac{\sigma_o \Delta C_p}{z_o} \int_{-\infty}^{\infty} K_{\xi 0} J_n(az_z K) H_n^{(1)}(az_z K) e^{i\phi_{FA}} \times e^{i \frac{a(\omega-q)}{\sigma_o} \Gamma_o} e^{-ia(\omega-n-q) \frac{x}{r_T}} d\omega d\Gamma_o dz_o \quad (7.21)$$

Now in applying Equations 7.4 and 7.7 to find the velocity potential, note that the operations are only on the x and t variables in Equation 7.21. Since these are only in exponentials, we can extract them temporarily:

$$E = e^{-i[(n+q)\Omega t + a(\omega-n-q) \frac{x}{r_T}]} \quad (7.22)$$

With the change of variables required by Equation 7.7, this becomes

$$E = e^{i[-(n+q)\Omega t + (n+q) \frac{\Omega x}{V} - a\omega \frac{x'}{r_T}]} \quad (7.23)$$

leaving us with the improper integral

$$I = \int_{-\infty}^x e^{-i \frac{a\omega x'}{r_T}} dx' \quad (7.24)$$

The standard method for evaluating this kind of integral is to add some damping in the exponent to suppress the oscillations at $-\infty$, evaluate the integral analytically, and then take the limit as the damping goes to zero. The result is given by Champeney (ref. 29), for example. In the present notation,

$$I = \frac{V}{\Omega} \left[\pi \delta(\omega) + \frac{i}{\omega} \right] e^{-i \frac{a\omega x}{r_T}} \quad (7.25)$$

Thus, the effect of the integration in Equation 7.7 is simply to insert the factor $\frac{1}{\Omega} \left[\pi \delta(\omega) + \frac{i}{\omega} \right]$ under the ω integral in Equation 7.21. The velocity potential is obtained by including the factor $-1/\rho_o$ from Equation 7.4 and performing the ω integration that is facilitated by $\delta(\omega)$. The result is the sum of 2 terms as follows.

$$\begin{aligned} \Phi = & \frac{B V r_T}{16} \sum_{m=-\infty}^{\infty} e^{in(\phi + \frac{\Omega x}{V} - \Omega t)} \iint \frac{\sigma_o \Delta C_p}{z_o} \bar{K}_{\xi 0} \bar{K}_{\xi} \mathcal{J}H_n(0) e^{i\phi_{FA}} e^{iaq(\frac{x}{r_T} - \frac{r_o}{\sigma_o})} d\Gamma_o dz_o \\ & + \frac{i B V r_T}{16 \pi} \sum_{m=-\infty}^{\infty} e^{in(\phi + \frac{\Omega x}{V} - \Omega t)} \iint \frac{\sigma_o \Delta C_p}{z_o} K_{\xi 0} \mathcal{J}H_n(\omega) e^{i\phi_{FA}} \frac{1}{\omega} e^{-ia(u-q)(\frac{x}{r_T} - \frac{r_o}{\sigma_o})} d\omega d\Gamma_o dz_o \end{aligned} \quad (7.26)$$

where we have introduced the shorthand notation

$$\mathcal{J}H_n(\omega) = J_n(az_{<}K) H_n^{(1)}(az_{>}K) \quad (7.27)$$

The frequency factor $e^{-iq\Omega t}$, that is common to both the loading and downwash, has been dropped from the expression for velocity potential in the remaining text, and is now implicit.

Downwash Velocity

The desired downwash velocity w/U is obtained by differentiating Φ in a direction normal to the helicoidal sheet according to

$$\alpha = \frac{w}{U} = \frac{1}{U} \frac{\partial \Phi}{\partial \xi} = \frac{1}{U} \left[\frac{\partial \Phi}{\partial x} \frac{\partial x}{\partial \xi} + \frac{\partial \Phi}{\partial \phi} \frac{\partial \phi}{\partial \xi} \right] \quad (7.28)$$

The partial derivatives for the chain rule can be evaluated from Equations 3.11a and 3.12a with the result

$$\alpha = \frac{-1}{\sigma U} \left[az \frac{\partial \Phi}{\partial x} + \frac{1}{z r_T} \frac{\partial \Phi}{\partial \phi} \right] \quad (7.29)$$

The operations are straightforward and produce

$$\begin{aligned} \alpha = & \frac{B}{8\pi z \sigma^2} \sum_{m=-\infty}^{\infty} e^{in\hat{\phi}} \iint \frac{\sigma_o \Delta C_p}{z_o} \bar{K}_{\xi 0} \bar{K}_{\xi} I_n(|n+q|az_{<}) K(|n+q|az_{>}) e^{iaq\Delta x} d\Gamma_o dz_o \\ & - \frac{B}{16\pi z \sigma^2} \sum_{m=-\infty}^{\infty} e^{in\hat{\phi}} \iint \frac{\sigma_o \Delta C_p}{z_o} K_{\xi 0} K_{\xi} \mathcal{J}H_n(\omega) \frac{1}{\omega} e^{-ia(u-q)\Delta x} d\omega d\Gamma_o dz_o \end{aligned} \quad (7.30)$$

$\hat{\phi}$ is the angle between the advance helicoid of the load point and the advance

helicoid of the field point:

$$\hat{\phi} = \phi + \frac{\Omega x}{V} - \Omega t - \frac{2\sigma_0}{z_0} \frac{FA}{D} = \phi_1 + \frac{\Omega x}{V} - \frac{2\sigma_0}{z_0} \frac{FA}{D} \quad (7.31)$$

and Δx is the axial distance from the load point to the field point x .

$$\Delta x = \frac{x}{r_T} - \frac{\Gamma_0}{\sigma_0} - \frac{2az_0}{\sigma_0} \frac{FA}{D} \quad (7.32)$$

Equation 7.30 can now be written as an integral equation in the form of Equation 7.1:

$$\alpha = \iint \Delta C_p(\gamma_0, z_0) \bar{K} d\Gamma_0 dz_0 \quad (7.33)$$

where the kernel function is

$$\begin{aligned} \bar{K} = & \frac{B\sigma_0}{8\pi\sigma^2 z z_0} \sum_{m=-\infty}^{\infty} e^{in\hat{\phi}} e^{iaq\Delta x} \bar{K}_{\xi 0} \bar{K}_{\xi} I_n(|n+q|az_z) K(|n+q|az_s) \\ & - \frac{B\sigma_0}{16\pi\sigma^2 z z_0} \sum_{m=-\infty}^{\infty} e^{in\hat{\phi}} e^{iaq\Delta x} \int_{-\infty}^{\infty} K_{\xi 0} K_{\xi} JH_n(\omega) \frac{1}{\omega} e^{-ia\omega\Delta x} d\omega \end{aligned} \quad (7.34)$$

Equations 7.33 and 7.44 are the downwash equations in their most general form giving the induced flow angle α as an integral of the lift pressure coefficient ΔC_p . For steady flow, $q=k=0$, the 2 terms of Equation 7.34 correspond exactly to the 2 terms of the wing kernel in Equation 7.2. The first term is independent of streamwise position x and is incompressible, i.e. the speed of sound doesn't appear via M_x or β . The second term gives the x dependence and has the compressibility information via M_x in the definition of K in Equations 7.9 and 7.27. Equation 7.34 is valid at any field point $\hat{\phi}, r, x$ except on the advance surfaces behind the point where the loading begins (normally the leading edge). On the advance surfaces, the kernel has the same singularities as the wing kernel of Equation 7.2. These singularities are not apparent from the form of Equation 7.34 but arise from the non-convergence of the m -series. Dealing with the singularities is the main challenge in applying the propeller kernel. For accurate results, they must be exposed and treated rigorously. Methods for dealing with the leading singularity are described next.

Wake and Bound Components of the Kernel Function

The 2 terms that have appeared in both the wing kernel and the propeller kernel include a second order singularity in the spanwise coordinate. That is, when the field point (y in Equation 7.2, z in Equation 7.34) approaches the load point (y_0 or z_0), the kernel diverges as $1/(y-y_0)^2$. This behavior is actually only a property of the wake, as will be shown, and thus for our purposes, a better subdivision of the kernel is into a wake term and a bound term rather than the current form. For clarity, this approach will be described first in terms of the wing kernel and then applied to the propeller kernel.

In examining the propeller kernel, the load is placed at the origin so that

Equation 7.2 simplifies to

$$K = \frac{1}{8\pi y^2} \left[1 + \frac{x}{\sqrt{x^2 + \beta^2 y^2}} \right] \quad (7.35)$$

The behavior of this is, of course, quite different far upstream and far downstream. For $x \gg 0$, the second term in the brackets approaches 1 and $K \rightarrow 1/4\pi y^2$. For $x \ll 0$, the 2 terms cancel and $K \rightarrow 0$. For finite x , the term in brackets in Equation 7.35 can be expanded as a binomial series with the result that

$$K \rightarrow \frac{1}{4\pi y^2} - \frac{1}{16\pi} \left(\frac{\beta}{x} \right)^2 + \text{terms of order } \beta^2 y^2 / x^2 \quad x > 0 \quad (7.36)$$

$$K \rightarrow \frac{1}{16\pi} \left(\frac{\beta}{x} \right)^2 + \text{terms of order } \beta^2 y^2 / x \quad x < 0$$

Thus, the singular behavior occurs only downstream of the load, as expected from physical considerations. The $1/y^2$ singularity can be confined to a wake term by adding $\text{sign}(x)$ to the first term in brackets and subtracting it from the second. Since $1 + \text{sign}(x)$ is twice the unit step function $H(x)$, the kernel now divides into a wake term K^w and a bound term K^b

$$K = K^w + K^b \quad (7.37)$$

where

$$K^w = \frac{1}{4\pi y^2} H(x) \quad (7.38)$$

$$K^b = \frac{1}{8\pi y^2} \left[\frac{x}{\sqrt{x^2 + \beta^2 y^2}} - \text{sign}(x) \right] \quad (7.39)$$

For large $|x|$, the bound term approaches $-\beta^2/(16\pi x^2)\text{sign}(x)$ and thus trails no wake, as its name implies. Furthermore, the wake term contains none of the second order singularity.

To use this same method to divide the propeller kernel into a wake term and a bound term, note in Equation 7.34 that the integrand in the second term contains the factor

$$F(\omega) = \frac{1}{\omega} e^{-i a \omega \Delta x} \quad (7.40)$$

where Δx , the non-dimensional axial distance between source point and field point, was given by Equation 7.32. Function F controls the behavior of the ω integral for large x . Also note that the integral of F over ω is proportional to

$$\int_0^{\infty} \frac{\sin a \omega \Delta x}{\omega} d\omega = \frac{\pi}{2} \text{sign}(\Delta x) \quad (7.41)$$

giving us a means to eliminate the wake behavior from the second term in \bar{K} . Specifically, we subtract $\bar{K}_{\xi 0} \bar{K}_{\xi} \mathcal{J}_n(0) F(\omega)$ from the integrand in the second term of Equation 7.34 and add its integral to the first term. The integral produces $\text{sign}(\Delta x)$ with a coefficient exactly equal to the first term in Equation 7.34. This yields a unit step function in the same manner as the wing kernel so that the kernel for the propeller can be written

$$\bar{K} = \bar{K}^w + \bar{K}^b \quad (7.42)$$

where

$$\bar{K}^w = \frac{B\sigma_o}{4\pi\sigma^2 z z_o} H(\Delta x) \sum_{m=-\infty}^{\infty} e^{in\hat{\phi}} e^{iaq\Delta x} \bar{K}_{\xi 0} \bar{K}_{\xi} I_n(|n+q|az_c) K(|n+q|az_s) \quad (7.43)$$

and

$$\bar{K}^b = \frac{-B\sigma_o}{16\pi\sigma^2 z z_o} \sum_{m=-\infty}^{\infty} e^{in\hat{\phi}} e^{iaq\Delta x} \int_{-\infty}^{\infty} [K_{\xi 0} K_{\xi} \mathcal{J}_n(\omega) - \bar{K}_{\xi 0} \bar{K}_{\xi} \mathcal{J}_n(0)] \frac{e^{-ia\omega\Delta x}}{\omega} d\omega \quad (7.44)$$

This is the final form of the propeller kernel before discretizing in Section 9. Like the wing kernel in Equations 7.38 and 7.39, the wake term is incompressible. Also, it can be seen that far downstream, \bar{K}^w is independent of x except for a convected wave in the unsteady case. The bound term contains the compressibility effects, as mentioned above.

Approach of Field Point to the Vortex Sheets

We still need to deal with the singular behavior of the kernel as the field point approaches the advance helicoid downstream of the load points. To simplify the discussion, we do this in the context of steady loading, i.e. for $q=k=0$, however, the same process applies to the unsteady load case. Also, it is instructive to determine the result that would have been established if the body force had been included in the integration of the momentum equation. This helps interpret the singular behavior of the kernel and also is needed in relating the circumferentially averaged results to classical propeller momentum theory.

To rewrite Equations 7.43 and 7.44, we eliminate the K 's defined in Equations 7.19 and 7.20 so as to expose the summation index explicitly. The steady loading kernel terms then become

$$\bar{K}^{sw} = \frac{B\sigma_o^3}{4\pi z z_o} H(\Delta x) \sum_{m=-\infty}^{\infty} n^2 e^{in\hat{\phi}} I_n(|n|az_c) K(|n|az_s) \quad (7.45)$$

$$\bar{K}^{sb} = \frac{-B\sigma_o}{16\pi\sigma^2 z z_o} \sum_{m=-\infty}^{\infty} e^{in\hat{\phi}} \int_{-\infty}^{\infty} [K_{\xi 0} K_{\xi} \mathcal{J}_n(\omega) - \bar{K}_{\xi 0} \bar{K}_{\xi} \mathcal{J}_n(0)] \frac{e^{-ia\omega\Delta x}}{\omega} d\omega \quad (7.46)$$

where the s in the K superscript denotes steady loading. These expressions are further modified by taking advantage of symmetry in n in the wake kernel and by separating the $n=0$ term in the bound kernel.

$$\bar{K}^{sw} = \frac{B\sigma_o^3}{2\pi z z_o} H(\Delta x) \sum_{m=1}^{\infty} n^2 \cos(n\hat{\phi}) I_n(naz_z) K(naz_z) \quad (7.47)$$

$$\bar{K}^{sb} = \bar{K}_0^{sb} + \bar{K}_{n0}^{sb} \quad (7.48)$$

where

$$\bar{K}_0^{sb} = \frac{B\sigma_o a^4 z z_o}{4\pi^2 \sigma^2} \int_0^{\infty} \omega I_0(a\beta\omega z_z) K_0(a\beta\omega z_z) \sin(a\omega\Delta x) d\omega \quad (7.49)$$

and

$$\bar{K}_{n0}^{sb} = \frac{-B\sigma_o}{16\pi\sigma^2 z z_o} \sum_{m=-\infty}^{\infty} e^{in\hat{\phi}} \int_{-\infty}^{\infty} [K_{\xi_0} K_{\xi} JH_n(\omega) - \bar{K}_{\xi_0} \bar{K}_{\xi} JH_n(0)] \frac{e^{-i a \omega \Delta x}}{\omega} d\omega \quad (7.50)$$

The prime on \sum' signifies that the $m=0$ term is not included in the sum.

In the last 4 equations, the summations are obviously harmonic series in the circumferential angle $\hat{\phi}$ with harmonic order $n=mB$. In the bound kernel, \bar{K}_0^{sb} , as the zeroth term in the series, represents the circumferential average induction and \bar{K}_{n0}^{sb} represents blade-to-blade variation. In the wake term \bar{K}^{sw} , however, we note that there is no zeroth element. This appears to suggest that there is no mean swirl or axial induction in the wake, which is obviously incorrect. Formal evaluation of the circumferential average of the wake term would require the integration:

$$\bar{K}_0^{sw} = \frac{1}{2\pi} \int_0^{2\pi} \bar{K}^{sw} d\hat{\phi} \quad (7.51)$$

The key to the apparent paradox is that the wake kernel is singular on the wake surfaces, and without the correct limiting process, cannot be integrated through the full range 0 to 2π in the obvious way.

Before proceeding, we will verify that the behavior of the wake term for $\hat{\phi}=0$ in Equation 7.47 is correct in comparison with the wing kernel behavior in Equation 7.38. This is accomplished by replacing I_n and K_n in Equation 7.47 by the first terms in their large-argument asymptotic forms from Reference 25:

$$I_n(naz) \rightarrow \frac{1}{\sqrt{2\pi n}} \frac{e^{n\lambda}}{(1+a^2 z^2)^{1/4}} \quad \text{and} \quad K_n(naz) \rightarrow \sqrt{\frac{\pi}{2n}} \frac{e^{-n\lambda}}{(1+a^2 z^2)^{1/4}} \quad (7.52)$$

where

$$\lambda = \sqrt{1+a^2 z^2} + \ln \frac{az}{1+\sqrt{1+a^2 z^2}} \quad (7.53)$$

This leads to the sum

$$\bar{K}^{sw} \rightarrow \frac{B^2 \sigma_o^3}{4\pi z z_o \sqrt{\sigma \sigma_o}} H(\Delta x) \sum_{m=1}^{\infty} m e^{-mB|\lambda-\lambda_o|} \quad (7.54)$$

which is a standard form yielding

$$\bar{K}^{sw} \rightarrow \frac{B^2 \sigma_o^3}{4\pi z z_o \sqrt{\sigma \sigma_o}} H(\Delta x) \frac{e^{-B|\lambda-\lambda_o|}}{(1-e^{-B|\lambda-\lambda_o|})^2} \quad (7.55)$$

When this is expanded about $z-z_0$, the leading term is found to be $H(\Delta x)/[4\pi(z-z_0)^2]$. This is exactly the same as the leading term in the wing kernel singularity (Equation 7.36), as might be expected from physical considerations, and can be considered a limited verification of Equation 7.47.

For the integral of the second order singularity, just exposed, we must take the Mangler principal value as discussed by Ashley and Landahl²⁷. The method we will use is different from most of these and was partially inspired by an analysis of Goodman (Reference 30) of marine propeller wakes. We return to the integral equation (7.33) and insert the wake kernel to get the wake term of the downwash associated with steady loading

$$\alpha^{sw} = \iint \Delta C_p(\gamma_0, z_0) \tilde{K}^{sw} d\Gamma_0 dz_0 \quad (7.56)$$

$$= \frac{B}{2\pi z} \int_{z_h}^1 \frac{\sigma_0^2}{z_0} S(z_0) \sum_{m=1}^{\infty} n^2 \cos(n\hat{\phi}) I_n(naz_<) K_n(naz_>) dz_0 \quad (7.57)$$

where

$$S(z_0) = \int \sigma_0 \Delta C_p(\gamma_0, z_0) H(\Delta x) d\Gamma_0 \quad (7.58)$$

is the radial distribution of the loading source. We now eliminate the $z_<$, $z_>$ notation and split the z_0 integration into its upper and lower portions. If we consider only the contributions of loading in a band of radii from z_1 to z_2 spanning the field point z , the downwash is

$$\begin{aligned} \alpha_{12}^{sw} = & \frac{B}{2\pi z} \sum_{m=1}^{\infty} n^2 \cos(n\hat{\phi}) \left[K_n(naz) \int_{z_1}^z \frac{\sigma_0^2}{z_0} S(z_0) I_n(naz_0) dz_0 \right. \\ & \left. + I_n(naz) \int_z^{z_2} \frac{\sigma_0^2}{z_0} S(z_0) K_n(naz_0) dz_0 \right] \end{aligned} \quad (7.59)$$

Next, we recall that the differential equation defining modified Bessel functions can be written

$$w(z) = \frac{z}{z^2+n^2} \frac{d}{dz} (z \frac{dw}{dz}) \quad (7.60)$$

In applying this to Equation 7.59 some cancellation occurs leaving

$$\begin{aligned} \alpha_{12}^{sw} = & \frac{B}{2\pi z} \sum_{m=1}^{\infty} \cos(n\hat{\phi}) \left[K_n(naz) \int_{z_1}^z S(z_0) \frac{d}{dz_0} z_0 \frac{dI_n(naz_0)}{dz_0} dz_0 \right. \\ & \left. + I_n(naz) \int_z^{z_2} S(z_0) \frac{d}{dz_0} z_0 \frac{dK_n(naz_0)}{dz_0} dz_0 \right] \end{aligned} \quad (7.61)$$

The reason for obtaining this form is to permit integration by parts, the result of which is

$$\begin{aligned}
\alpha_{12}^{s w} = & \frac{B}{2\pi z} \sum_{m=1}^{\infty} \cos(n\hat{\phi}) \left\{ S(z) \text{naz} [K_n(\text{naz}) I_n'(\text{naz}) - I_n'(\text{naz}) K_n(\text{naz})] \right. \\
& + \text{naz}_2 S(z_2) I_n(\text{naz}) K_n'(\text{naz}_2) - \text{naz}_1 S(z_1) K_n(\text{naz}) I_n'(\text{naz}_1) \\
& \left. - K_n(\text{naz}) \int_{z_1}^z \text{naz}_o \frac{dS(z_o)}{dz_o} I_n'(\text{naz}_o) dz_o - I_n(\text{naz}) \int_z^{z_2} \text{naz}_o \frac{dS(z_o)}{dz_o} K_n'(\text{naz}_o) dz_o \right\}
\end{aligned} \tag{7.62}$$

The first line comes from the integrated terms evaluated at the field point z ; the second line comes from these terms evaluated at the extremes of the integration range; and the last line contains the remaining integrals.

The first line can be simplified by noting that the expression in square brackets is the Wronskian $W[K_n(x), I_n(x)] = 1/x$. In anticipation of the final result, this term will be called α_0^{sw} so that

$$\alpha_{12}^{s w} = \alpha_0^{sw} + \alpha_{n0}^{sw} \tag{7.63}$$

where

$$\alpha_0^{sw} = \frac{B}{2\pi z} S(z) \sum_{m=1}^{\infty} \cos(mB\hat{\phi}) \tag{7.64}$$

and

$$\begin{aligned}
\alpha_{n0}^{sw} = & \text{naz}_2 S(z_2) I_n(\text{naz}) K_n'(\text{naz}_2) - \text{naz}_1 S(z_1) K_n(\text{naz}) I_n'(\text{naz}_1) \\
& - K_n(\text{naz}) \int_{z_1}^z \text{naz}_o \frac{dS(z_o)}{dz_o} I_n'(\text{naz}_o) dz_o - I_n(\text{naz}) \int_z^{z_2} \text{naz}_o \frac{dS(z_o)}{dz_o} K_n'(\text{naz}_o) dz_o
\end{aligned} \tag{7.65}$$

The more interesting term here is α_0^{sw} with its non-decaying cosine series. Because of its importance, two independent ways of interpreting this term will be given. The simpler scheme is to rewrite the series as follows.

$$\sum_{m=1}^{\infty} \cos(mB\hat{\phi}) = \frac{1}{2} \sum_{m=-\infty}^{\infty} \cos(mB\hat{\phi}) - \frac{1}{2} \tag{7.66}$$

The double sided series is related to the delta function series

$$\sum_{m=-\infty}^{\infty} \cos(m\hat{\phi}) = 2\pi \delta(\hat{\phi}) \tag{7.67}$$

Since this is 0 everywhere except at $\hat{\phi} = 0$, it is also 0 in the limit as $\hat{\phi}$ approaches 0. Similar analysis of the series in Equation 7.66 shows that it too is 0 except for $\hat{\phi} = 0, 2\pi/B, 4\pi/B, \text{etc.}$, which is to say on the trailing vortex sheets. Since it was emphasized above that the downwash formulas are valid in the limit as the field point approaches the vortex sheets, we conclude that the correct value for the sum in Equations 7.64 and 7.66 is $-1/2$. Thus,

$$\alpha_0^{sw} = \frac{-B}{4\pi z} S(z) \tag{7.68}$$

The conclusion of this analysis of Equation 7.64 is that an expression with only oscillating terms and no mean value is correctly interpreted as having a mean value and no oscillation! In fact, this term represents the mean (circumferentially averaged) swirl and axial induction in the wake that seemed to be missing and thus resolves the paradox described in conjunction with Equations 7.48 and 7.51. The significance of the minus sign in Equation 7.68 is that the downwash for positive blade loading is, in fact, down. Comparison of this expression with classical propeller momentum theory will be given in Section 8 and the alternative means of deriving Equation 7.68 will be given in the next subsection. However, first we take time to comment on the results derived so far.

It was stated above that Equations 7.43-45 constitute the final form of the propeller kernel. This is indeed the form used for the discretization described in Section 9. However, both the wake and bound terms of the kernel are singular where the load point radius z_0 and field point radius z are equal. The leading singularity in the wake term has just been discussed and it is clear that Equation 7.44 is not suitable for numerical work for small $z-z_0$. The scheme used in the computer code is to divide the radial integration range into 3 sections: a narrow singular section (typically $\Delta z_0 = .02$) centered on z , an inboard section extending from the root to the singular section, and an outboard section extending from the singular section to the tip. In the singular section a special form is used for the wake portion of the kernel based on the integration by parts scheme presented above. In fact, for best results, another integration by parts is used to deal with a logarithmic singularity driven by the second derivative of $S(z_0)$.

The bound term of the kernel has a logarithmic singularity at $z_0 = z$ that is also manifested in the non-convergence of the harmonic series. This too is dealt with by dividing the radial integration range into three sections. For the singular section, a patch is made to a special form of the wing kernel. The logarithmic singularity is then integrated by analytical curve fitting. The special form of the wing kernel was derived by the same pressure potential method used for the propeller. The resultant form is similar to Equation 7.44 with the Fourier transform but without the summation.

Integral of Body Force Term in Momentum Equation

We now return to the singular behavior of the wake term and approach it by a different method. This is a variation of the scheme used by Lordi and Homicz (Reference 7) in their pressure potential analysis of ducted rotor flow. They studied the singularity using the velocity potential rather than the downwash expression, but the concept is similar. The idea is to include the body force term in integration of the momentum equation. When this is done, it is found that the singularities of the force term and those of the pressure term cancel exactly, as will be seen.

Representation of the body force for steady loading was given by Equation 3.20 (with $\omega_0 = 0$) in coordinates fixed in the fluid. The lift component is

$$f_L = - \delta(\xi+FA) \hat{f}_L(\gamma+Ut) \quad (7.69)$$

f_L is the force per unit volume on the fluid whereas \hat{f}_L is the force per unit area on the helicoidal surface. γ is the coordinate running backward along the helical advance path as shown in Figure 4 so that $\gamma+Ut$ represents the blade section motion. For convenience in manipulation, Equation 7.69 can be expressed as a delta function integral as follows.

$$f_L = - \delta(\xi+FA) \int \hat{f}_L(\gamma_o) \delta(\gamma-\gamma_o+Ut) d\gamma_o \quad (7.70)$$

By using the same changes of variable that were described in conjunction with Equations 3.13 to 3.15, the volume force can be re-expressed as

$$f_L = - \frac{\sigma}{F} \delta(\phi - \frac{\Omega x}{V} - \frac{U}{V} FA) \int \hat{f}_L(\gamma_o) \delta(-\sigma x - \frac{\Omega r}{V} FA - \gamma_o + Ut) d\gamma_o \quad (7.71)$$

When this is changed to fuselage-fixed coordinates via $x=x_1+Vt$ and then the sign convention for x is changed to positive downstream via $x_1 \rightarrow -x$, time drops out, leaving

$$f_L = - \frac{\sigma}{F} \delta(\hat{\phi}) \int \hat{f}_L(\gamma_o) \delta(\sigma x - \frac{\Omega r}{V} FA - \gamma_o) d\gamma_o \quad (7.72)$$

where $\hat{\phi}$ was given by Equation 7.31. By expanding the first delta function in a series and applying the property $\delta(ax) = \delta(x)/a$ to the second delta function, this can be further modified to read

$$f_L = - \frac{B}{2\pi r} \sum_{m=-\infty}^{\infty} e^{imB\hat{\phi}} \int \hat{f}_L(\gamma_o) \delta(\Delta x) d\Gamma_o \quad (7.73)$$

The number of blades effect has been accounted for with the appearance of the B as a coefficient and in $n=mB$ as in Section 3. In coefficient form, the lift force per unit area

$$\hat{f}_j(\gamma_o) = \frac{1}{2} \rho_o U^2 \Delta C_p(\gamma_o) \quad (7.74)$$

If we call the associated force/unit volume f_L , then the acceleration due to the body force becomes

$$\frac{1}{\rho_o} f_L = \frac{-BU^2}{4\pi r} \sum_{m=-\infty}^{\infty} e^{imB\hat{\phi}} \int \Delta C_p(\gamma_o) \delta(\Delta x) d\Gamma_o \quad (7.75)$$

This was the term avoided in Equation 7.3 by integrating above or below the airfoil as suggested by Figure 10. But, Equation 7.75 can now easily be integrated using the method of following the particle outlined at the beginning of this section. Since f_L is the force normal to the helicoidal lifting surface, its integral is the disturbance velocity normal to the surface, w . Expressed as an angle, the result is

$$\frac{w}{U} = \alpha = \frac{-B}{4\pi z} \sum_{m=-\infty}^{\infty} e^{imB\hat{\phi}} \int \sigma \Delta C_p(\gamma_o) H(\Delta x) d\Gamma_o \quad (7.76)$$

Since the integral in this equation is the source S defined by Equation 7.58, the downwash due to the body force can be rewritten as

$$\alpha = \frac{-B}{4\pi z} S(z) \left[1 + 2 \sum_{m=1}^{\infty} \cos(mB\hat{\phi}) \right] \quad (7.77)$$

Now it can be seen that, when the downwash caused by the body force is added to that caused by the pressure term in the momentum equation, the series in Equation 7.64 is cancelled term by term for $m=1$ to ∞ . Only the zeroth term in Equation 7.77 remains so that the circumferential average term is $-BS(z)/4\pi z$, as was found above by the limiting process.

Both the limiting process and the body force cancellation schemes are valid means for dealing with the singularity at $z_0 = z$ and finding the circumferential average induction. Because of the subtleties involved, it is worthwhile to understand both methods. Furthermore, it will be seen in the next section that the body force method is needed to understand the circumferentially average axial induction and compare it to classical momentum theory.

SECTION 8

RELATIONSHIP BETWEEN LIFTING SURFACE THEORY AND CLASSICAL PROPELLER MOMENTUM THEORY

In the previous section, equations were developed for the downwash normal to the helicoidal advance surface caused by a specified distribution of lift pressure on the surface. This was in complete analogy to the wing downwash equations whose advance surface is a plane aligned with the flight direction. The equations are in the form of a Fourier series whose zeroth term gives the circumferential average of the downwash (or induction) and whose higher terms give the blade-to-blade variation. In this section, we concentrate on the circumferential average terms. They will be formulated to give axial and tangential induced flows as functions of elemental thrust and torque. This is as opposed to the treatment in previous sections that gave downwash as functions of lift force. The purpose of this is to compare the lifting surface theory with classical propeller momentum theory, which deals only with circumferential average effects. In the process, insight is given as to the roles of the various terms, the effect of compressibility, and a method for treating the non-linearity associated with finite axial induction. The derivation is given first for the general case of a rotor with loading distributed along the chord, i.e. a "thick" rotor. The blades can have sweep and offset. Then, for comparison with momentum theory, the loading will be specialized to an actuator disc form.

Mean Induction for "Thick" Rotor

The derivation for the axial and tangential induction components is based on the integration of the linearized momentum equation

$$\frac{Dv}{Dt} = \frac{1}{\rho_0} (\underline{F} - \nabla p) \quad (8.1)$$

The integration procedure is similar to that in Section 7, but different in detail. We use the result, established at the end of Section 7, that the zeroth term of the pressure field can be taken from Equation 7.8 and the zeroth term of the body force can be taken from the original source representation. We start first with the pressure field.

The circumferential average of the pressure is given by the n=0 term of Equation 7.8

$$p = \frac{aB\rho_0}{8\pi} \int_{z_h}^1 U_0^2 \int_{-\infty}^{\infty} e^{i\phi_{FA}} e^{i\phi_x} e^{i\phi_s} \Psi_F(k_x) J_0(az_{<}K) H_0^{(1)}(az_{>}K) d\omega dz_0 \quad (8.2)$$

The radial wavenumber K is pure imaginary for n=0 and q=0

$$K = \sqrt{M_x^2 \omega^2 - \omega^2} = \sqrt{-\beta^2 \omega^2} \quad (8.3)$$

so that the Bessel function product becomes

$$JH = \frac{2}{i\pi} I_0(a\beta z_{<}|\omega|)K_0(a\beta z_{>}|\omega|) \quad (8.4)$$

where I_0 and K_0 are modified Bessel functions, as shown in Section 3. Ψ_F is the Fourier transform representing the axial and tangential force distributions as given by Equation 3.69. It is important to note that, for $n=0$, there is no contribution from the tangential force to the circumferential average of the pressure. As will be seen, the consequence of this is that there is no mean swirl upstream of the rotor. To return to the original force representation from the Fourier transform, Equations 3.69, 3.61, and 3.21 are applied in that order with the result

$$\Psi_F(k_x)e^{i\phi_s} = \frac{-a\omega}{\rho_o U_o^2} \int_{-\infty}^{\infty} \hat{f}_x(\gamma_o)e^{i\frac{a\omega}{\sigma_o}\Gamma_o} d\Gamma_o \quad (8.5)$$

where \hat{f}_x is the distribution over a blade of the axial force per unit blade area. As a Fourier transform, the integration range runs from $-\infty$ to ∞ but, of course, the blade loading is non-zero only between the leading edge and trailing edge. Substitution of this expression into Equation 8.2 gives the pressure field

$$p = \frac{ia^2B}{4\pi^2} \iint \hat{f}_x(\gamma_o) \int \omega I_0(a\beta z_{<}|\omega|)K_0(a\beta z_{>}|\omega|)e^{-ia\omega\Delta x} d\omega d\Gamma_o dz_o \quad (8.6)$$

where Δx , the axial distance between source point and field point, is repeated here from Section 7

$$\Delta x = \frac{x}{r_T} - \frac{\Gamma_o}{\sigma_o} - \frac{2az_o}{\sigma_o} \frac{FA}{D} \quad (8.7)$$

The gradient of p involves derivatives in the x , ϕ , and z directions. But we can see that the gradient in the tangential direction is zero and, in the present linearization, we will ignore the radial gradient. The remaining component, $\hat{i}\partial p/\partial x$, is trivial to find. The operations to compute the axial velocity disturbance associated with the pressure (or bound) term are symbolized by

$$v_{x_o}^b = \int_{-\infty}^x \frac{-1}{\rho_o} \frac{\partial p(x')}{\partial x'} \frac{dx'}{V} \quad (8.8)$$

The V under the integral requires some discussion at this point. It represents the velocity of the particle whose acceleration is being integrated as a function of particle position x' . Equation 8.8 could be integrated numerically by setting $V=V_o+v_{x_o}^b$ and updating V at each step in x' . However, to deal with Equation 8.8 analytically, V is set equal to its "average" for the integration range, namely $\bar{V}(z)$, and brought outside the integral. Interpretation of the word "average" will be given below in the momentum theory discussion.

For the integration in Equation 8.8, there is no contribution at $\omega=0$, as there was for the higher order terms in Section 7, because the limit of the integrand is 0 at $\omega=0$. The impact of differentiating and then integrating with respect to x is simply to change the constant in Equation 8.6 with the following result

$$v_{x0}^b = \frac{-ia^2B}{4\pi^2\rho_0\bar{V}} \iint \hat{f}_x(\gamma_0) \int_{-\infty}^{\infty} \omega I_0(a\beta z_{<}|\omega|) K_0(a\beta z_{>}|\omega|) e^{-ia\omega\Delta x} d\omega d\Gamma_0 dz_0 \quad (8.9)$$

for the velocity disturbance associated the pressure field. From consideration of symmetry in the ω integral, this can be written in pure real form as follows

$$v_{x0}^b = \frac{-a^2B}{2\pi^2\rho_0\bar{V}} \int_{z_h}^1 \int_{-\infty}^{\infty} \hat{f}_x(\gamma_0) \int_0^{\infty} \omega I_0(a\beta z_{<}\omega) K_0(a\beta z_{>}\omega) \sin(a\omega\Delta x) d\omega d\Gamma_0 dz_0 \quad (8.10)$$

To find the velocity disturbance associated with the body force, we pick out the zeroth term from Equation 7.73 and interpret it for both the axial and tangential force components as follows

$$f_x = \frac{B}{2\pi r} \int \hat{f}_x(\gamma_0) \delta(\Delta x) d\Gamma_0 \quad (8.11)$$

and

$$f_\phi = \frac{B}{2\pi r} \int \hat{f}_\phi(\gamma_0) \delta(\Delta x) d\Gamma_0 \quad (8.12)$$

The minus sign that was in Equation 7.73 has been dropped because of the following convention. f_x is the axial force per unit volume acting on the fluid and \hat{f}_x is the axial force per unit area acting on the blade surface. The usual sense of positive thrust for a propeller is associated with a downstream (positive x direction) force on the fluid; thus, the minus sign is not needed here. Similar remarks apply to the tangential force. The integral to find the velocity caused by the body force is

$$v_{x0}^w = \int_{-\infty}^x \frac{\hat{f}_x}{\rho_0} \frac{dx'}{V} \quad (8.13)$$

This is easily applied to Equation 8.11 with the result

$$v_{x0}^w = \frac{B}{2\pi z\rho_0\bar{V}} \int \hat{f}_x(\gamma_0) H(\Delta x) d\Gamma_0 \quad (8.14)$$

where the V has been brought outside the integral as \bar{V} for the same reasons presented after Equation 8.8. The same procedure applied to Equation 8.12 gives

$$v_{\phi 0} = \frac{B}{2\pi z\rho_0\bar{V}} \int \hat{f}_\phi(\gamma_0) H(\Delta x) d\Gamma_0 \quad (8.15)$$

This completes the derivation for the circumferentially averaged induction for steady loading. Tangential velocity is given by Equation 8.15. This simply states that $v_{\phi 0}$ is proportional to the tangential force integrated up to the axial field point x . The axial induction is the sum of the bound and wake terms

$$v_{x0} = v_{x0}^b + v_{x0}^w \quad (8.16)$$

where, as with the tangential component, the wake term is proportional to the integrated force up to the field point. The bound (or pressure) term in Equation 8.10 is in the form of a Fourier integral and contains the compressibility effect via the β in the arguments of the modified Bessel functions. The w integral could, perhaps, be evaluated in terms of elliptic integrals, but this doesn't appear to be particularly useful. A better approach is to move the Γ_0 integration to the inside and compute the Fourier integral of \hat{f}_x . In the discretization process described in Section 9, the loading is expressed as a series of shape function with unknown coefficients. The shapes are chosen such that their transforms can be computed analytically. This leaves only the w and z_0 integrals, which can be computed rapidly.

Actuator Disc Results

The propeller loading can be collapsed onto a zero thickness disc by setting the face alignment FA to 0 and replacing the force-per-unit-blade-area representation by thrust- and torque-per-unit-radius as follows

$$B\hat{f}_x(\gamma_0) = \frac{1}{r_T} \frac{dT}{dz_0} \delta(\gamma_0) \quad (8.17)$$

$$B\hat{f}_\phi(\gamma_0) = \frac{1}{z_0 r_T^2} \frac{dQ}{dz_0} \delta(\gamma_0) \quad (8.18)$$

Dealing first with the tangential velocity, we substitute Equation 8.18 for the load representation into Equation 8.15 and perform the Γ_0 integration. The result is simply

$$\hat{v}_{\phi_0} = \frac{1}{2\pi z^2 \rho_0 \bar{V} r_T^3} \frac{dQ}{dz} H(\Delta x) \quad (8.19)$$

where here the $\hat{}$ signifies actuator disc results. This shows, via the step function $H(\Delta x)$, that tangential velocity component jumps from zero ahead of the rotor to its final value immediately behind the rotor. The behavior is shown in the top sketch of Figure 11 and agrees with textbook treatment of propeller aerodynamics (ref.31).

For the axial induction, we substitute Equation 8.17 into Equation 8.10 and perform the Γ_0 integration with the following result for the bound or pressure term

$$\hat{v}_{x_0}^b = \frac{-1}{2\pi^2 \rho_0 \bar{V} r_T^2} \int_{z_h}^1 \frac{dT}{dz_0} \int_0^\infty w I_0(\beta z_0 w) K_0(\beta z_0 w) \sin(w \frac{x}{r_T}) dw dz_0 \quad (8.20)$$

And from Equation 8.14 the wake term is

$$\hat{v}_{x_0}^w = \frac{1}{2\pi z \rho_0 \bar{V} r_T^2} \frac{dT}{dz} H(\Delta x) \quad (8.21)$$

The total axial induction for the actuator disc approximation is the sum of these 2 terms

$$\hat{v}_{x0} = \hat{v}_{x0}^b + \hat{v}_{x0}^w \quad (8.22)$$

The wake term of the axial induction, shown in Figure 11b, jumps at the rotor disc in the same fashion as the tangential velocity. The bound term is odd in x and has the general behavior sketched in Figure 11c.

Since the bound term of the axial component also jumps at the disc plane, we will evaluate the magnitude of the jump to see how the 2 terms work in concert. Because the argument of the sine function in Equation 8.19 includes the product ωx , it is clear that the behavior near $x = 0$ is controlled by the behavior of the integrand at large ω . Thus, we can use the large argument asymptotic form for the Bessel functions to evaluate the inside integral in Equation 8.20.

$$I = \int_0^\infty \omega I_0(\beta \omega z_c) K_0(\beta \omega z_s) \sin(\omega \frac{x}{r_T}) d\omega \quad (8.23)$$

Upon substitution of asymptotic forms from Reference 25, this becomes

$$I = \frac{1}{2\beta \sqrt{zz_0}} \int_0^\infty e^{-\beta \omega |z-z_0|} \sin(\omega \frac{x}{r_T}) d\omega \quad (8.24)$$

which is given by a standard integral as follows

$$I = \frac{1}{2\beta \sqrt{zz_0}} \frac{\frac{x}{r_T}}{\left(\frac{x}{r_T}\right)^2 + \beta^2(z-z_0)^2} \quad (8.25)$$

Now, in the remaining z_0 integration, any section of the integration range not containing the field point z will produce 0 in the limit as $x \rightarrow 0$. However, we still must consider a small band centered on z to find any contribution from that point. Thus, we evaluate

$$\hat{v}_{x0}^b(0^+) = \frac{-1}{4\pi^2 \rho_0 \bar{v} \beta r_T^2 z} \frac{dT}{dz} \lim_{x \rightarrow 0} \left[\frac{x}{r_T} \int_{z-\Delta z}^{z+\Delta z} \frac{dz_0}{\left(\frac{x}{r_T}\right)^2 + \beta^2(z-z_0)^2} \right] \quad (8.26)$$

The term in square brackets is

$$[\] = \frac{1}{\beta} \tan^{-1} \left(\frac{\beta r_T}{x} z_0 \right) \Big|_{-\Delta z}^{\Delta z} \quad (8.27)$$

If Δz is held fixed and finite, the limit of this is π/β and the result for Equation 8.26 is

$$\hat{v}_{x_0}^b(0^+) = \frac{-1}{4\pi z \rho_0 \hat{v} \beta^2 r_T^2} \frac{dT}{dz} \quad (8.28)$$

and the jump in the bound term at $x=0$ is twice that or

$$\Delta \hat{v}_{x_0}^b = \frac{-1}{2\pi z \rho_0 \hat{v} \beta^2 r_T^2} \frac{dT}{dz} \quad (8.29)$$

The jumps in axial velocity from the bound term in Equation 8.29 and the wake term in Equation 8.21 can now be compared. For incompressible flow ($\beta=1$), the jumps exactly cancel so that the axial flow is smooth through the disc as in the classical propeller momentum theory (ref. 31) and sketched at the bottom in Figure 11d. However, for compressible flow, the jump in the bound term is larger so that the sum of the 2 terms is discontinuous as also shown in Figure 11d. The velocity jump is required for mass continuity because the density in front of the rotor is lower than that behind. This was recognized by Vogeley (ref. 32) but could not be included in his actuator disc analysis.

Sample Calculations

The discontinuous jumps in velocity found in the preceding section are, of course, artifacts of the actuator disc representation of the loading. With the more general "thick rotor" formulation above, the velocity variations are smooth but still influenced by compressibility. Here we present some sample calculations of axial induction for realistic rotor geometry and loading using Equations 8.10 and 8.14.

The study rotor is representative of the front rotor of a counter rotation Prop-Fan designed for a flight Mach number of 0.72 and an advance ratio of 2.94. Figure 12 at the bottom gives radial distributions of chord-to-diameter ratio and thrust coefficient. At each radial station the chordwise distribution of loading is assumed to be constant. The top of the figure shows the axial induction profiles at several axial stations. Note that behind the rotor the induction is forward outside the blade tips. This obviously could have a strong effect on a rear rotor if the streamline from the front rotor contracts inside the rear rotor tips. A trailing wing would also be affected.

Figure 13 plots the axial induced velocity normalized by the flight speed at radius ratio $z=0.78$ as a function of axial coordinate. Incompressible calculations for the same case are also shown. As described above, the effect of compressibility is to increase the induced velocity in front of the rotor and reduce it behind. There is little effect at blade mid-chord. The compressible actuator disc results above gave a discontinuous axial velocity whereas the thick rotor theory predicts a smooth distribution.

The compressibility effect just shown has an interesting influence on chordwise blade loading. Higher induction in front tends to unload the leading edge and lower induction behind tends to add loading to the trailing edge. This result could not be deduced from lifting line theory, which deals only with mid-chord induction values. The consequence is that compressibility produces the need for more camber in the blade sections. The effect is in addition to the aft movement of the loading on 2D airfoils caused by non-linear compressibility.

Comparison with Propeller Momentum Theory
and Effect of Non-linearity

Simple propeller theories require the axial induction at the blade midchord so that 2D airfoil data can be used. We will call this midchord value v_{xd} and note from the figures just discussed that it is 1/2 the ultimate wake value. In Weick's book (Reference 33), Newton's second law takes the following form.

$$dT = (dA * \rho_o \bar{V}) * (2v_{xd})$$

(mass/unit time) * (velocity increase)

(8.30)

where dA is an annular element of disc area and \bar{V} is the velocity through the disc. Thus, the velocity at the disc can be expressed

$$v_{xd} = \frac{1}{2\rho_o \bar{V}} \frac{dT}{dA}$$

(8.31)

To compare this with the theory of the present report, note that Equation 8.14 shows the wake velocity to be

$$2v_{xd} = \frac{1}{2\pi z \rho_o \bar{V} r_T^2} \frac{dT}{dz}$$

(8.32)

When it is recognized that the elemental area $dA = 2\pi z r_T^2 dz$, then it can be seen that the circumferentially averaged induction of the present theory is exactly the same as classical momentum theory provided that \bar{V} has the same meaning. This is discussed in the next paragraph.

In Equation 8.30, \bar{V} is related to the mass flux through the disc and must therefore include the flight speed plus the axial induction at the disc v_{xd} . Thus, we can write

$$v_{xd} = \frac{1}{2\rho_o (V_o + v_{xd})} \frac{dT}{dA}$$

(8.33)

This is the form of the induction equation shown in many textbooks. Since v_{xd} and thrust are not known a priori, loading is usually found by iteration. For completeness, note that these same procedures applied to Equation 8.19 lead to the standard relation between torque and tangential induced velocity

$$v_{\phi d} = \frac{1}{2\rho_o (V_o + v_{xd}) r} \frac{dQ}{dA}$$

(8.34)

In the original development of the author's helicoidal lifting surface theory (ref. 15), the derivation paralleled that for wing pressure potential theory. In

the wing problem, there is no axial induction and it is correct to set \bar{V} equal to the flight speed V_o . This same linearization works well for propellers in high speed flight; but, at takeoff conditions, V_o and v_{xd} can be about the same and the linearization gives poor results. For the static condition, it fails completely. Then Equation 8.33 must be iteratively solved with v_{xd} included on the right hand side of the equation.

Now that a means to deal with the axial induction non-linearity has been established for the circumferentially averaged flow, it still must be decided how to deal with that effect in the full lifting surface theory. The approach taken is that we force the non-linear momentum equation (Equation 8.31) be satisfied in the circumferential average sense at each radial station by iteration. This establishes the value of \bar{V} as a function of z . Blade-to-blade variations in induction and unsteady effects are calculated using equations in Section 7 with the flight speed set to \bar{V} . Effectively, the solution is then linearized about the non-linear momentum value at each radius. The iteration scheme is discussed at the end of Section 11.

SECTION 9

DISCRETIZATION OF INTEGRAL EQUATION

This section develops the method for computing blade loading from the downwash theory derived in Section 7. Blade loads are needed as input to the noise equations in Sections 4 and 5 and to the performance equations in Section 11. The downwash equation was given by Equation 7.33, which is repeated below.

$$\alpha = \iint \Delta C_p(\gamma_o, z_o) \bar{K} d\Gamma_o dz_o \quad (9.1)$$

This gives the downwash angle α as an integral over the blade surface of the coefficient of lift pressure times a kernel function. The kernel function is given by Equations 7.43 and 7.44. The difficulty with Equation 9.1 is, of course, that the unknown pressure is under the integral whereas α is known on the blade from geometry. Specifically, α is the angle the flow must be turned by the loading so as to be tangent to the camber surface. To solve Equation 9.1, it is inverted by discretizing the lift pressure (i.e. writing it in the form of a series of load elements with coefficients to be found), converting it to a matrix equation, and inverting the matrix. The procedure is similar to that described in Reference 16. The main difference is in the refinement of the loading elements from a quasi-vortex lattice representation to true lifting surface.

In the next paragraph, the general procedure is outlined. Then, the inversion scheme is worked out in detail.

General Form of Inversion Method

First, we write Equation 9.1 in generalized form as

$$\alpha = \int \Delta C_p K dA \quad (9.2)$$

where dA is an element of blade area. Flow tangency will be enforced at a number of control points on the blade surface counted by the index μ . The array of downwash angles at the control points forms the downwash vector W_μ so that Equation 9.2 becomes

$$W_\mu = \int \Delta C_p K_\mu dA \quad (9.3)$$

where the kernel function is now evaluated at the control points. Symbolically, the discrete form for the loading can be written

$$\Delta C_p = \sum_\nu L_\nu S_\nu \quad (9.4)$$

where the S_ν 's are a family of shape functions of unit amplitude and the L_ν 's are their coefficients which are to be found. Inserting this loading representation into Equation 9.3 gives

$$W_\mu = \int \sum_\nu L_\nu S_\nu K_\mu dA \quad (9.5)$$

Now the integral is moved inside the sum with the result

$$W_\mu = \sum_\nu L_\nu \int S_\nu K_\mu dA \quad (9.6)$$

The integral is a function of both indices and becomes the matrix element

$$K_{\mu\nu} = \int S_\nu K_\mu dA \quad (9.7)$$

Thus, by discretization, the integral equation has been converted to the matrix equation

$$W_\mu = \sum_\nu L_\nu K_{\mu\nu} \quad (9.8)$$

Its inverse is

$$L_\nu = \sum_\mu K_{\mu\nu}^{-1} W_\mu \quad (9.9)$$

With this system, the known downwash can be used to compute the coefficients L_ν and these can be used to construct the loading with Equation 9.4.

This has been a schematic description of the inversion process. The actual method described below for the propeller equation is more complex, but follows the same principles.

Inversion of Propeller Integral Equation

The field point in the kernel given by Equations 7.43 and 7.44 is given in cylindrical coordinates. In this section, the control point locations must be expressed in terms of blade surface coordinates so we switch x and $\hat{\phi}$ to helicoidal surface coordinates using the inverse of Equations 3.11 and 3.12, namely

$$x = \frac{V}{U}\gamma - \frac{\Omega r}{U}\xi = \frac{1}{\sigma}\gamma - \frac{az}{\sigma}\xi \quad (9.10)$$

$$r\hat{\phi}_1 = -\frac{\Omega r}{U}\gamma - \frac{V}{U}\xi = -\frac{az}{\sigma}\gamma - \frac{1}{\sigma}\xi \quad (9.11)$$

Note that the sign convention for x has been changed from that in the acoustics sections to positive downstream for the aerodynamic applications starting with Section 7. With this transformation, the angle between the source and control point helicoids becomes

$$\hat{\phi} = -\frac{\sigma}{Z} \frac{\xi}{\Gamma_T} - \frac{\sigma_o}{Z_o} \frac{FA}{\Gamma_T} \quad (9.12)$$

and the axial separation between source and control points becomes

$$\Delta x = \frac{\Gamma}{\sigma} - \frac{\Gamma_o}{\sigma_o} + \Delta x_\xi \quad (9.14)$$

where Δx_ξ is shorthand notation for

$$\Delta x_\xi = -\frac{az}{\sigma} \frac{\xi}{\Gamma_T} - \frac{az_o}{\sigma_o} \frac{FA}{\Gamma_T} \quad (9.15)$$

With these changes in notation, the appropriate expression for downwash is obtained by combining Equations 7.42, 7.43, 7.44, and 9.1

$$\begin{aligned}
\alpha = & \frac{B}{4\pi\sigma^2z} \int_{z_h}^1 \frac{\sigma_o}{z_o} \int_{-\infty}^{\infty} \Delta C_p(\gamma_o, z_o) e^{iqa(\frac{\Gamma}{\sigma} - \frac{\Gamma_o}{\sigma_o} + \Delta x_\xi)} H(\Delta x) d\Gamma_o \\
& \times \sum_{m=-\infty}^{\infty} e^{in\hat{\phi}_n} \bar{K}_{\xi 0} \bar{K}_\xi I_n(|n+q|az_o) K(|n+q|az_o) dz_o \\
= & \frac{B}{16\pi\sigma^2z} \int_{z_h}^1 \frac{\sigma_o}{z_o} \sum_{m=-\infty}^{\infty} e^{in\hat{\phi}_n} \int_{-\infty}^{\infty} \int_{-\infty}^{\infty} \Delta C_p(\gamma_o, z_o) e^{-ia(\omega-q)(\frac{\Gamma}{\sigma} - \frac{\Gamma_o}{\sigma_o} + \Delta x_\xi)} d\Gamma_o \\
& \times \frac{1}{\omega} [K_{\xi 0} K_\xi JH_n(\omega) - \bar{K}_{\xi 0} \bar{K}_\xi JH_n(0)] d\omega dz_o \tag{9.16}
\end{aligned}$$

The system for load paneling and control point locations is shown in Figure 14. It shows the blade divided into NCP spanwise panels which are tapered at constant percent chord. Control points, where flow tangency is enforced, are in chordwise arrays at radii z_i . The index system for the control points is the same as in Reference 16, namely that $i=1, 2, \dots$, NSM counts the radial locations and $\bar{m} = 1, 2, \dots$, NCP counts the chordwise positions. Downwash velocities are given by the vector W_μ whose index combines the chordwise and spanwise counters as follows

$$\mu = (i-1)NCP + \bar{m} \tag{9.17}$$

Downwash is not computed simply at the control points but rather is averaged over a small chordwise range by using the following operation

$$W_\mu = \int \alpha G(\Gamma - \Gamma_{\bar{m}}, z_i) d\Gamma \tag{9.18}$$

G is a weighting function that centers the averaging at the chordwise location $\Gamma_{\bar{m}}$ at radius z_i . This chordwise location is given by

$$\Gamma_{\bar{m}} = \frac{MCA}{r_T} - B_D + (\bar{m} - 1 + CP)\Delta_o \tag{9.19}$$

where MCA is the sweep defined by Figure 4, B_D is chord to diameter ratio, CP is the location of the control point within the panel (0.5 for the middle), and the panel width is

$$\Delta_o = \frac{2B_D}{NCP} \tag{9.20}$$

Various forms for G could be used but the best seems to be

$$G(\Gamma - \Gamma_{\bar{m}}, z_i) = \frac{2\sqrt{\ln 2}}{\Delta\sqrt{\pi}} \exp\left[-\frac{4}{\Delta^2} \ln 2 (\Gamma - \Gamma_{\bar{m}})^2\right] \tag{9.21}$$

This is a Gaussian function with unit area. Dependence on z_i comes in via Δ , the width of the Gaussian function at its half amplitude points. This is tied to the local panel width on the blade by the formula

$$\Delta = \frac{2B_D}{NCP} * CHW = \Delta_o * CHW \tag{9.22}$$

where B_D is chord-to-diameter ratio and CHW stands for control point 1/2 width. Δ is the width of the weighting function at its 1/2 amplitude points normalized by the width of a load panel. Averaging the downwash in this manner is reasonable from a physical point of view; however, the main reason for doing it, as will be seen, is that it damps the ω integrand at large values of ω and guarantees convergence of the integral. Furthermore, on blade sections with supersonic speed, the kernel

function has very strong gradients near Mach waves. When control points are near these Mach waves, results can be sensitive to the exact location of the control points if the kernel is not averaged.

The scheme for load elements is also shown in Figure 14. As mentioned above, the blade is divided into NCP spanwise panels of constant percent chord. Spanwise variation of loading within panels is given by a series of shape functions R_j as sketched at the upper right in the figure. Each of these has built into it an elliptic falloff at the tip since this is the correct behavior for wing tips. A few different families have been evaluated but the one currently used by default in the computer program is

$$R_j = z_o \sin[j \cos^{-1}(z_o)] \quad (9.23)$$

The first 7 of these functions are plotted in Figure 15. The family was adapted from one commonly used in wing methods by multiplying by z_o to drive the functions to 0 at $z_o = 0$. It can be seen that the functions vary most rapidly at the tip where pressure gradients are expected to be the greatest.

Chordwise variation of the load elements is also shown in Figure 14. A series of overlapping elements $C_{\bar{n}}$ is used with some special treatment at the leading and trailing edges as shown at the lower right in the figure. At the leading edge, the user of the computer program can choose the triangular element shown with the dashes or the preferred singular element shown by the solid curve. The latter element is formulated so that, with the adjacent triangular element, it gives the correct leading edge behavior for 2D cases. At the trailing edge, the basic element goes to 0 for subsonic trailing edges [$M_{rel} \cos(\text{trailing edge sweep angle}) < 1$] satisfying the Kutta condition. For supersonic edges, a finite jump is allowed since the Kutta condition doesn't apply. There is a blending at the sonic radius between the 2 types of element. Chordwise elements $C_{\bar{n}}$ are counted by \bar{n} which runs from 1 to NCP. The combined index for the spanwise and chordwise variation is

$$\nu = (j-1)NCP + \bar{n} \quad (9.24)$$

The associated loading can now be written

$$\Delta C_p(\gamma_o, z_o) = \frac{1}{\sigma_o} \sum_{j, \bar{n}} L_{\nu} R_j(z_o) C_{\bar{n}}(\Gamma_o, z_o) \quad (9.25)$$

Note that this distribution is continuous in the chordwise direction and continuous and smooth in the spanwise direction. This degree of smoothness is needed for supersonic flow because any artificial discontinuities in loading can cause Mach waves that lead to unstable solutions. If the method were only to be used for subsonic flow, it would be much less sensitive so that a crude load system could be used, perhaps even a system of constant pressure panels.

The load elements $C_{\bar{n}}$ are each different in the sense that they appear at various values of Γ_o , depending on blade geometry. By using a change of variable, they can be expressed in terms of 3 common functions as follows

$$C_{\bar{n}}(\Gamma_o, z_o) = F_{\Delta}(\Gamma_o - \Gamma_{o\bar{n}}) \quad (9.26)$$

$\Gamma_{o\bar{n}}$ is the helicoidal distance to the leading edge of element \bar{n} .

$$\Gamma_{o\bar{n}} = \frac{MCA}{r_T} - B_D + (\bar{m} - 1)\Delta_o \quad (9.27)$$

Figure 16 defines the 3 types of load element in terms of the panel width Δ_o .

We can now insert the discretized loading given by Equation 9.25 into the downwash equation (9.16) and perform the control point averaging indicated by Equation 9.18. The result is the desired matrix equation

$$W_\mu = \sum_\nu L_\nu K_{\mu\nu} \quad (9.28)$$

where the matrix elements are, using the crossed integral sign defined below,

$$K_{\mu\nu} = \int_{z_h}^1 R_j(z_o) K_{\bar{m}\bar{n}} dz_o \quad (9.29)$$

and the chordwise-integrated kernel is

$$\begin{aligned} K_{\bar{m}\bar{n}} = & \frac{B}{4\pi\sigma^2 z z_o} \int G(\Gamma - \Gamma_{\bar{m}}, z_i) \int F_\Delta(\Gamma_o - \Gamma_{o\bar{n}}) H(\Delta x) e^{iqa(\frac{\Gamma}{\sigma} - \frac{\Gamma_o}{\sigma_o} + \Delta x_\xi)} d\Gamma_o d\Gamma \\ & \times \sum_{m=-\infty}^{\infty} e^{in\hat{\phi}} \bar{K}_{\xi 0} \bar{K}_\xi I_n(|n+q|az_-) K_n(|n+q|az_+) \\ & - \frac{B}{16\pi\sigma^2 z z_o} \sum_{m=-\infty}^{\infty} e^{in\hat{\phi}} \left[\int G(\Gamma - \Gamma_{\bar{m}}, z_i) \int F_\Delta(\Gamma_o - \Gamma_{o\bar{n}}) e^{-ia(w-q)(\frac{\Gamma}{\sigma} - \frac{\Gamma_o}{\sigma_o} + \Delta x_\xi)} d\Gamma_o d\Gamma \right. \\ & \left. \times \frac{1}{w} [K_{\xi 0} K_\xi JH_n(w) - \bar{K}_{\xi 0} \bar{K}_\xi JH_n(0)] dw \right] \quad (9.30) \end{aligned}$$

In Equation 9.29 the significance of the crossed integral is that integration of z_o through the control point radius z_i does not exist in the ordinary sense. It must be interpreted as the "finite part of an infinite integral" or the Mangler principal value²⁷ because of the singularities discussed in Section 8.

If we now shift the integration variables with $\Gamma \rightarrow \Gamma - \Gamma_{\bar{m}}$ and $\Gamma_o \rightarrow \Gamma_o - \Gamma_{o\bar{n}}$, then the chordwise-integrated kernel becomes

$$\begin{aligned} K_{\bar{m}\bar{n}} = & \frac{B}{4\pi\sigma^2 z z_o} e^{iqa(\frac{\Gamma_{\bar{m}}}{\sigma} - \frac{\Gamma_{o\bar{n}}}{\sigma_o} + \Delta x_\xi)} I_{\bar{m}\bar{n}} \sum_{m=-\infty}^{\infty} e^{in\hat{\phi}} \bar{K}_{\xi 0} \bar{K}_\xi I_n(|n+q|az_-) K_n(|n+q|az_+) \\ & - \frac{B}{16\pi\sigma^2 z z_o} \sum_{m=-\infty}^{\infty} e^{in\hat{\phi}} \int \Pi_{\bar{m}\bar{n}} e^{-ia(w-q)(\frac{\Gamma_{\bar{m}}}{\sigma} - \frac{\Gamma_{o\bar{n}}}{\sigma_o} + \Delta x_\xi)} \frac{1}{w} [K_{\xi 0} K_\xi JH_n(w) - \bar{K}_{\xi 0} \bar{K}_\xi JH_n(0)] dw \quad (9.31) \end{aligned}$$

where the double chordwise integrals are

$$I_{\bar{m}\bar{n}} = \int G_{\bar{m}}(\Gamma) \int F_{\Delta}(\Gamma_o) H(\Delta x') e^{iaq(\frac{\Gamma}{\sigma} - \frac{\Gamma_o}{\sigma_o})} d\Gamma_o d\Gamma \quad (9.32)$$

and

$$\Pi_{\bar{m}\bar{n}} = \int G_{\bar{m}}(\Gamma) \int F_{\Delta}(\Gamma_o) e^{-ia(\omega-q)(\frac{\Gamma}{\sigma} - \frac{\Gamma_o}{\sigma_o})} d\Gamma_o d\Gamma \quad (9.33)$$

The argument of the step function is

$$\Delta x' = \left(\frac{\Gamma + \Gamma_{\bar{m}}}{\sigma} - az \frac{\xi}{\sigma r_T} \right) - \left(\frac{\Gamma_o + \Gamma_{o\bar{n}}}{\sigma_o} + az_o \frac{FA}{\sigma_o r_T} \right) \quad (9.34)$$

Finally, we can define the axial displacement between the control point and the load element as

$$x_{\mu\nu} = \left(\frac{az_o}{\sigma_o} FA + \frac{az}{\sigma} \frac{\xi}{r_T} \right) + \left(\frac{\Gamma_{o\bar{n}}}{\sigma_o} - \frac{\Gamma_{\bar{m}}}{\sigma} \right) \quad (9.35)$$

and arrive at the final form for the chordwise-integrated kernel

$$K_{\bar{m}\bar{n}} = \frac{B}{4\pi\sigma^2 z z_o} e^{-iqax_{\mu\nu}} I_{\bar{m}\bar{n}} \sum_{m=-\infty}^{\infty} e^{in\hat{\phi}} \bar{K}_{\xi_0} \bar{K}_{\xi} I_n(|n+q|az_{<}) K_n(|n+q|az_{>}) \\ - \frac{B}{16\pi\sigma^2 z z_o} e^{-iaqx_{\mu\nu}} \sum_{m=-\infty}^{\infty} e^{in\hat{\phi}} \int_{-\infty}^{\infty} \Pi_{\bar{m}\bar{n}} e^{ia\omega x_{\mu\nu}} \frac{1}{\omega} [K_{\xi_0} K_{\xi} J_n(\omega) - \bar{K}_{\xi_0} \bar{K}_{\xi} J_n(0)] d\omega \quad (9.36)$$

The first and second terms give the wake effect and the bound effect, respectively.

Major results of this derivation can be summarized as follows. The matrix form of the lifting surface integral equation is given by Equation 9.28. The kernel matrix is to be computed from Equations 9.29 and 9.36. The inverse equation (9.9) can be solved for the loading vector L_{ν} given the vector of downwash angles W_{μ} . The distribution of lift pressure over the blade surface can be constructed from Equations 9.25 and 9.26. Details for computing the downwash vector are given in Section 10.

Comments on Evaluation of Kernel Function

To evaluate $I_{\bar{m}\bar{n}}$, note that the integration ranges of Γ and Γ_o are very small because of the local nature of the G and F functions. Thus, the exponential can be set to 1 for q "not too large". This amounts to neglecting phase variations within one load element; phase variations from panel to panel are still included via the exponential containing $x_{\mu\nu}$. If this approximation is not satisfactory for a given set of panels, then the number of panels can be increased to make the G and F functions more local. Thus, for the integral in the wake term, we have

$$I_{\bar{m}\bar{n}} = \int G_{\bar{m}}(\Gamma) \int F_{\Delta}(\Gamma_o) H(\Delta x') d\Gamma_o d\Gamma \quad (9.37)$$

which is easily evaluated by numerical methods. It exhibits the wake behavior explicitly since it varies smoothly from 0 upstream of the rotor to 1 behind.

For evaluation of Π_{mn} , note that Equation 9.33 can be written as the product of 2 integrals

$$\Pi_{mn} = \bar{X} * \bar{X}_1 \quad (9.38)$$

The first,

$$\bar{X} = \int_{G_m}(\Gamma) e^{-ia(w-q)\frac{\Gamma}{\sigma}} d\Gamma \quad (9.39)$$

is the result of averaging over the control point range and can be evaluated analytically with the result

$$\bar{X} = \exp \left\{ - \left[\frac{(w-q)a\Delta}{4\sqrt{\ln 2} \sigma} \right]^2 \right\} \quad (9.40)$$

where Δ is defined by Equation 9.22. As mentioned above, this has the effect of damping the integrand in Equation 9.36 and guarantees convergence of the integral. The second of the 2 integrals in Equation 9.38 is

$$\bar{X}_1 = \int_{F_\Delta}(\Gamma_o) e^{ia(w-q)\frac{\Gamma_o}{\sigma_o}} d\Gamma_o \quad (9.41)$$

This is the Fourier integral of the load element shapes in Figure 16, which can also be evaluated analytically except for the singular leading edge element. For example, for the mid-chord elements

$$\bar{X}_1 = \frac{2 \left\{ 1 - \cos \left[(w-q)\frac{a\Delta_o}{\sigma_o} \right] \right\}}{\left[(w-q)\frac{a\Delta_o}{\sigma_o} \right]^2} \quad (9.42)$$

This is pure real because F_Δ is an even function. The leading edge element must be integrated numerically. This is done once during a computer run and stored as an array for later interpolation. The cost is negligible.

In Equation 9.36, the integral over w is also a Fourier transform. Since it is needed at several values of the variable $x_{\mu\nu}$, it is best evaluated by fast Fourier transform (FFT) methods. The integrand is conditioned for good behavior at the origin and the infinite limits cause no problem because of the damping provided by the \bar{X} function.

Finally, some remarks are needed on the radial integration denoted by Equation 9.29. As was mentioned above, the double bars through the integral sign signify special treatment as the load point passes through the control point, i.e. near $z_o=z_i$. The wake term and the bound term are integrated separately to keep control over their singular behavior. For the wake term, the radial integration is divided into 3 ranges: a narrow range centered on the singular point and 2 outer (non-singular) ranges covering the remainder of the blade. The non-singular ranges are done with a direct integration of the first term of Equation 9.36. In the singular range, the integrand is reformulated using integration by parts as described in Section 7. This exposes singularities of order $(z_i-z_o)^{-2}$, $(z_i-z_o)^{-1}$, and $\log|z_i-z_o|$ which can be integrated analytically because the mode functions R_j and their derivatives are given in analytic form.

Radial integration of the bound term in Equation 9.36 is also divided into a singular range and 2 non-singular ranges. In the non-singular ranges the second term is integrated directly. For the singular range, the order of the singularity

had to be established. This was first accomplished by some very tedious series expansions of the integrand using asymptotic forms of Bessel functions to expose a logarithmic singularity. The result was confirmed by analysis of the bound term of the steady wing kernel in Equation 7.39. It was found that, when this is integrated in the chordwise direction first, as we have for the propeller kernel, the remaining spanwise behavior is logarithmic at chordwise locations within the load element. In fact, strength of the singularity is proportional to the chordwise derivative of the load function. Since the behaviors of wing kernels and propeller kernels are expected to be the same near the singularities, it was decided to patch to a wing formula in the singular region. Unfortunately, Equation 7.39 applies only to steady loading and the published unsteady formulas are unwieldy. A suitable form of wing theory was derived by applying the methods of Sections 3 and 7 to translating sources, including the procedure of separating the wake and bound terms. The result is again a Fourier integral involving a Bessel function but without the infinite sum that appears in the rotating case. It was verified by numerical experimentation that this form of the bound wing kernel matches the propeller kernel close to the singularity. Because of its simple form, the bound wing kernel can be computed with good enough accuracy to integrate it by numerical curve fitting. This is the scheme used in the computer program.

SECTION 10

BOUNDARY CONDITIONS AND INVERSION OF INTEGRAL EQUATION

In the preceding section the lifting surface integral equation that was derived in Section 7 was discretized for conversion to a matrix equation as follows.

$$W_\mu = \sum_\nu K_{\mu\nu} L_\nu \quad (10.1)$$

W_μ is the vector of downwash angles on the blade surface at control points which are counted, as shown in Figure 14, by the index μ . L_ν is the vector of loading coefficients whose index ν corresponds to members of a family of loading element shape functions. $K_{\mu\nu}$ is the matrix of influence coefficients giving the downwash at control point μ due to a unit load from element ν . Equation 10.1 is to be solved by matrix inversion

$$L_\nu = \sum_{\mu\nu} K_{\mu\nu}^{-1} W_\mu \quad (10.2)$$

giving the loading vector for specified downwash angles at the control points.

Note that Equation 10.1 gives the flow deflection due only to the blade loading. There are other deflections, due to blade thickness and nacelle blockage, that must be accounted for before the matrix equation can be applied. The "air angle accounting" system is the subject of this report section.

Boundary Conditions

Definitions of the angles to be used are given in Figure 17. The basic requirement for flow tangency is that the air angles must match the hardware angles at the control points. As shown in Figure 14, control points are placed at radius ratios z_i , where the radius index i runs from 1 to NSM, and are placed one per panel across the chord with the index \bar{m} . The combined index for matrix rows is

$$\mu = (i-1) * NCP + \bar{m} \quad (10.3)$$

Hardware angles are shown in the figure at the upper left. These are specified in terms of a blade angle (or twist angle) θ_b and camber angle θ_{cam} . As described in conjunction with Figure 4, the angles are measured in the cylindrical surface, $z_i = \text{constant}$. Thus, to construct the hardware angles the blade is "cut" by the cylindrical surfaces z_i and rolled out flat before the angles are determined. Blade angle is a function of index i only. It is determined by constructing the chord line and measuring its angle from the plane of rotation. Camber angle is a function of both the i and \bar{m} indices. It is computed according to the sketch at the bottom of Figure 17 from

$$\theta_{cam} = - \frac{dh}{dX} \quad (10.4)$$

at chordwise positions

$$X_{\bar{m}} = \frac{\bar{m} - 1 + CP}{NCP} \quad (10.5)$$

where CP is the non-dimensional position of the control point within the panel. The panel midpoint corresponds to CP=0.5. In Equation 10.4, the small disturbance assumption was invoked to approximate the tangent of the camber angle by the angle itself.

Flow angles are defined by the velocity triangles in Figure 17. Forward flight speed is V_o and the rotational speed at radius ratio z_i is πNDz_i . Thus, the section advance angle at radius z_i is

$$\tan \phi_o = \frac{V_o}{\pi NDz_i} = \frac{\text{advance ratio}}{\pi z_i} = \frac{1}{az_i} \quad (10.6)$$

For the blockage, a separate calculation is performed with any appropriate axisymmetric flow program to represent the effect of the nacelle, hub, and spinner. Axial velocity components are stored on a grid that encompasses the propeller position and then interpolated to the blade control points to find the blockage angle from

$$\phi_{\text{block}} = \tan^{-1}\left(\frac{1}{az} \frac{V}{V_o}\right) - \phi_o \quad (10.7)$$

as a function of both indices i and \bar{m} . Finally, the thickness effect is computed from the theory in Section 3 with details given at the end of this section.

Using the notation of Figure 17, the match of the hardware angles to the flow angles can be expressed for each control point by

$$\alpha_L + \alpha_T + \phi_o + \phi_{\text{block}} = \theta_B + \theta_{\text{cam}} \quad (10.8)$$

or, in terms of the unknown angle,

$$\alpha_L = \theta_B + \theta_{\text{cam}} - \phi_o - \phi_{\text{block}} - \alpha_T \quad (10.9)$$

Sign conventions for the induction in Section 7 are opposite that in Figure 17, requiring the new notation

$$\alpha_L = -W_\mu \quad \text{and} \quad \alpha_T = -[W_T]_\mu \quad (10.10)$$

so that the downwash vector is computed from

$$W_\mu = -[\theta_B]_\mu - [\theta_{\text{cam}}]_\mu + [\phi_o]_\mu + [\phi_{\text{block}}]_\mu - [W_T]_\mu \quad (10.11)$$

A table in the computer printout lists the air angle accounting in these terms with one entry for each control point.

There are other boundaries in the problem that should be mentioned at this point. The boundary at infinite radius has been taken care of in Section 3 by allowing only outgoing waves in the solution. Thus, we are guaranteed no reflections or interference from any artificial outer boundary. Also in the wake as $x \rightarrow \infty$ only convected vortex sheets appear with no possibility for reflected waves or influence back at the rotor. However, the boundary condition at the nacelle center body has been neglected for the current solution. Since the primary motivation for this work was to develop a noise prediction method, it was felt that errors in blade loading in the root area would not have an important influence on radiation predictions. Furthermore, blade root flow is usually dominated by transonic non-linear and viscous effects not covered by the present linear theory.

Induction Caused by Thickness

In lifting surface theory for isolated wings, the flow field induced by the thickness effect can be ignored from symmetry considerations. For propellers, however, this symmetry no longer applies because of multiple blades and twist. Thickness at one radius can induce angle of attack at another radius. The pressure field for this effect was derived in Section 3 and can be converted into velocity potential and downwash following the procedures used in Section 7 for the loading effect. The derivation was given in Reference 15 in a slightly different notation and is so similar to the loading derivation of this report that it is not given here. Results can be written down almost by inspection.

It turns out that the thickness effect is fairly weak, typically inducing flow angles of a degree or less. Thus, blade sections do not need to be represented very accurately. For expediency, we approximate all blade sections using a parabolic thickness distribution

$$H(X) = 1 - (2X)^2 \quad (10.12)$$

and a thickness to chord ratio at each radius given by

$$t_b = \frac{\text{max thickness}}{\text{chord}} \quad (10.13)$$

The transform of this source is required by Equation 3.66

$$\Psi_V(k_x) = \int_{-1/2}^{1/2} H(X) e^{ik_x X} dX \quad (10.14)$$

where the wavenumber

$$k_x = \frac{2\omega a}{\sigma_0} B_D \quad (10.15)$$

The integral can be performed analytically with the result

$$\Psi_V(k_x) = 2 \left[\frac{\sin(k_x/2)}{(k_x/2)^3} - \frac{\cos(k_x/2)}{(k_x/2)^2} \right] \quad (10.16)$$

The corresponding induced angle at the control points is

$$[W_T]_\mu = \frac{-ia^2 B}{2\pi\sigma^2 z} \sum_{m=-\infty}^{\infty} \int_{z_h}^1 e^{in\phi_n} B_D^2 t_b \int_{-\infty}^{\infty} e^{i\omega a x_{\mu\nu}} \bar{X} \Psi_V(k_x) \omega K_\xi JH_n(\omega) d\omega dz_o \quad (10.17)$$

This is in a form very much like the results of Equation 9.28, 9.29, and 9.36 for the loading induction and, regarding its evaluation, many of the remarks given in Section 9 apply. \bar{X} arises from averaging over a small region near the control points and has the same meaning as in Equation 9.40 with $q=0$. It can be seen that the source transform for loading, given by \bar{X}_1 in Equation 9.42, is replaced by Ψ_V .

As a final remark, we point out that the parabolic thickness approximation used in this section for airload prediction is not used for noise calculations, where thickness may be the dominant effect.

SECTION 11

AERODYNAMIC PERFORMANCE

Propeller performance is measured in terms of thrust, power, and efficiency. In general, efficiency is power output divided by power input or

$$\eta = \frac{\text{THRUST} * \text{VELOCITY}}{\text{SHAFT POWER}} \quad (11.1)$$

Shaft power is an unambiguous quantity for this application but thrust is more complicated because of nacelle blockage effects. Apparent thrust relates to blade forces only whereas net thrust includes the penalty for nacelle forces associated with the propeller slipstream. Because this report deals only with blade forces, the efficiency computed herein is what the industry knows as "apparent efficiency". Thrust and power are used in coefficient form

$$C_T = \frac{\text{THRUST}}{\rho_o N^2 D^4}, \quad \text{Thrust coefficient} \quad (11.2)$$

and

$$C_P = \frac{\text{POWER}}{\rho_o N^3 D^5}, \quad \text{Power coefficient} \quad (11.3)$$

Combination of these 3 equations leads to

$$\eta = J \frac{C_T}{C_P} \quad (11.4)$$

In previous sections treating blade forces, only lift has been considered. Lift, in the lifting surface context, is that force component perpendicular to the local direction of advance at any blade radius. If this were the only force acting, then the propeller would have unit efficiency because there would be no force component in the direction of motion. Drag is considered to have 3 components which can be discussed with reference to Figure 9. Wave drag is related to energy radiating through the surface S_2 and was treated in Section 6 via a sound power analysis. Vortex drag is related to the energy left in the wake and passing through S_3 . This can be computed via an integral over the vortex sheets. Finally, viscous drag at the blade surfaces is treated in strip fashion by the use of 2D airfoil tables. In the paragraphs below it is shown how thrust and power are related to lift and drag, how vortex drag is computed, how performance is computed on a linear basis, and then how this is corrected for non-linearity associated with finite axial induction.

Force Resolution

The relation between thrust and torque components and lift and drag components can be deduced from the velocity triangles in Figure 18. The thrust force per unit radius is dT/Dr and the tangential force per unit radius is rdQ/dr where Q is torque. The corresponding lift and drag forces per unit radius are $(1/2)\rho_o U_o^2 b C_L$ and $(1/2)\rho_o U_o^2 b C_D$. From consideration of similar triangles it can be found immediately that

$$\frac{dT}{dr} = \frac{1}{2}\rho_o U^2 b \left[C_L \frac{az}{\sigma} - C_D \frac{1}{\sigma} \right] \quad (11.5)$$

and

$$r \frac{dQ}{dr} = \frac{1}{2}\rho_o U^2 b \left[C_L \frac{1}{\sigma} + C_D \frac{az}{\sigma} \right] \quad (11.6)$$

In terms of the coefficients defined above these become

$$\frac{dC_T}{dz} = \frac{\pi^2 B \sigma B_D}{4a^2} (az C_L - C_D) \quad (11.7)$$

and

$$\frac{dC_P}{dz} = \frac{\pi^3 B \sigma B_D}{4a^3} (C_L + az C_D) \quad (11.8)$$

No physics has yet entered the analysis; the above expressions simply represent a rotation of coordinates according to Figure 18. The components of C_D are discussed below.

Vortex Drag

Two dimensional airfoils in steady, subsonic, inviscid flow have no drag and trail no vortex systems. However, in 3D flow, lift falls off at the tips and a vortex system results. The drag associated with the energy of the vortices is known as vortex drag. Other names for the same phenomenon are induced drag and drag due to lift. Our analysis of vortex drag is an extension of the far wake method applied to wings in the book by Ashley and Landahl (ref. 27). This method is attractive because it applies equally to subsonic and supersonic blade section speeds and deals only with wake formulas, which are incompressible. In Figure 9, which was adapted from Reference 27, the flow through S_3 has a kinetic energy that, in principle, could be computed from the volume integral of the kinetic energy density. However, in the reference it is shown how to convert this volume integral to an integral over the surface of the vortex sheets

$$K.E. = - \frac{\rho_o}{2} \iint \Delta\phi w dS \quad (11.9)$$

where the jump in potential $\Delta\phi$ is equal to the circulation at corresponding spanwise location on the lifting surface and w is the induced downwash. The element of surface area in the notation of Section 7 is $drd\gamma$ where γ is the surface coordinate in the advance direction in Figure 4 (not circulation). The energy per unit area of the vortex sheet can then be written

$$\frac{d[d(K.E.)/d\gamma]}{d\gamma} = - \frac{\rho_o}{2} \Delta\phi w \quad (11.10)$$

To relate this to force on the local blade sections, note that an increment of kinetic energy can be related to an increment of work by the drag force as follows

$$d(K.E.) = dF_D d\gamma \quad (11.11)$$

or in per unit span terms

$$\frac{d(K.E.)}{dr} = \frac{dF_D}{dr} d\gamma \quad (11.12)$$

Thus, we have

$$\frac{dF_D}{dr} = - \frac{\rho_o}{2} \Delta\phi w \quad (11.13)$$

This can be expressed in terms of the coefficient of vortex drag via

$$\frac{dF_D}{dr} = C_D \frac{1}{2} \rho_o U^2 b \quad (11.14)$$

When these formulas are combined with the expression for section circulation

$$\Delta\phi = \frac{bUC_L}{2} \quad (11.15)$$

the result is

$$\left(\frac{C_D}{C_L} \right)_{VD} = - \frac{1}{2} \left(\frac{w}{U} \right)_{\text{far wake}} \quad (11.16)$$

This is exactly the same expression that is well known in wing theory. It was rederived here to illustrate its origin and to demonstrate that it retains its form in the propeller context.

An expression for the far wake downwash has already been derived in Section 7 and will be adapted for vortex drag calculation. Equation 7.57 evaluated on the vortex sheets is

$$\left(\frac{w}{U} \right)_{\text{far wake}} = \frac{B}{2\pi z} \int_{z_h}^1 \frac{\sigma_o^2}{z_o} S(z_o) \sum_{m=1}^{\infty} I_n(naz_<) K_n(naz_>) dz_o \quad (11.17)$$

with $n=mB$. In the far wake, the source term is

$$S(z_o) = \sigma_o \int \Delta C_P(\gamma_o, z_o) \frac{d\gamma_o}{r_T} \quad (11.18)$$

which integrates to

$$S(z_o) = 2B_D \sigma_o C_L \quad (11.19)$$

Combination of these expressions leads to the working equation for the coefficient of vortex drag

$$\left(\frac{C_D}{C_L} \right)_{VD} = \frac{-B}{2\pi z} \int_{z_h}^1 \frac{\sigma_o^3}{z_o} B_D C_L \sum_{m=1}^{\infty} I_n(naz_<) K_n(naz_>) dz_o \quad (11.20)$$

The double bar on the integral sign signifies the finite part of an infinite integral or the Mangler principal value (ref. 27). Methods to deal with this were discussed in Section 7.

Performance Calculation

All of the necessary ingredients for computation of performance on a linear basis have now been developed. The procedure works as follows. The blade pressure distribution is calculated using the inversion method described in Section 10. Pressure distributions are integrated chordwise to find the spanwise distributions of lift coefficient. The C_L 's are then used with the above formulas to find vortex drag. C_L 's are also used with 2D airfoil tables to look up viscous (or profile) drag coefficients. This is done for the proper camber, thickness, and Mach number with corrections based on simple sweep theory. These 2 components of drag are used with Equations 11.7 and 11.8 to find the radial thrust and power distributions which, in turn, are integrated to determine the overall thrust and power coefficients from

$$C_T = \int_{z_h}^1 \frac{dC_T}{dz_o} dz_o \quad \text{and} \quad C_P = \int_{z_h}^1 \frac{dC_P}{dz_o} dz_o \quad (11.21)$$

Then apparent efficiency is computed from Equation 11.4. If Mach number is high enough, the coefficient of sound power is computed using the formula in Section 6 and added to the denominator in Equation 11.4 to account for the associated efficiency loss.

A correction scheme has been developed to deal with the non-linearity caused by finite axial induction and is described in the remainder of this section. This aspect of non-linearity was discussed at the end of Section 8 and was shown to be related to the mass flux through the propeller disc. Evaluation of the circumferentially averaged flow showed that the relation between thrust and axial induced velocity did not satisfy the momentum equation. However, by adding the induction to the flight speed, momentum could be satisfied in the average sense. The problem was that the axial induction is not known a priori so that an iteration procedure must be used. The key to the method is to recall that in Section 7 the factor $1/V$ was moved outside an integral, recognizing that a correction would have to be made later. V is the velocity that determines the mass flux and is easy to correct because it appears in a simple factor outside the integral representing the kernel function.

The iteration procedure is illustrated schematically in Figure 19. It is based on satisfying the momentum relation given by Equation 8.32 which can be cast in terms of radial distribution of thrust coefficient as follows

$$\frac{v_x}{V_o} = \frac{a^2}{\pi^3 z (1 + v_x/V_o)} \frac{dC_T}{dz} \quad (11.22)$$

v_x is the axial induced velocity at the propeller disc. The kernel function matrix is first computed at the actual propeller advance ratio so that the corresponding \tilde{V} is the flight speed V_o . Then performance is computed using the scheme just described. Part of the performance calculation is to determine the thrust distribution dC_T/dz . This is used to find the momentum related induction from Equation 11.22 as a function of radius but on a circumferentially averaged basis. The induction is used to correct the kernel matrix in blocks at each control point radius by multiplying by the factor $V_o/(V_o + v_{xd})$ where v_{xd} is the axial induction at the mid-load point of the disc. The corrected matrix is inverted again and the loop is repeated until convergence is achieved.

This procedure makes a great improvement in power prediction at takeoff speeds and powers. At very high loading, it overpredicts power and needs to be refined by recognizing the effect of increased dynamic pressure in producing blade forces and in including the loading associated with vortex flow in the momentum balance.

SECTION 12

FORMULAS FOR WAKE PREDICTIONS

This section presents formulas that have been programmed for the 3 components of the velocity disturbance caused by blade thickness and steady loading. Since the velocity potential was derived in Section 7, all that remains are some straightforward manipulations to arrive at the working formulas, which are listed below. Volume III of this report presents sample calculations and comparisons with test data.

In Section 7, we not only derived the velocity potential, Equation 7.26, but differentiated it in the axial and tangential directions to find the corresponding velocity components. These were used with Equation 7.28, which is repeated here to find the downwash component

$$\frac{w}{U} = \frac{1}{U} \frac{\partial \Phi}{\partial \xi} = \frac{1}{U} \left[\frac{\partial \Phi}{\partial x} \frac{\partial x}{\partial \xi} + \frac{\partial \Phi}{\partial \phi} \frac{\partial \phi}{\partial \xi} \right] \quad (12.1)$$

normalized by the local section speed. The corresponding formula for the component parallel to the advance direction is

$$\frac{u}{U} = \frac{1}{U} \frac{\partial \Phi}{\partial \gamma} = \frac{1}{U} \left[\frac{\partial \Phi}{\partial x} \frac{\partial x}{\partial \gamma} + \frac{\partial \Phi}{\partial \phi} \frac{\partial \phi}{\partial \gamma} \right] \quad (12.2)$$

and the radial component is simply

$$\frac{v}{V} = \frac{1}{V} \frac{\partial \Phi}{\partial r} \quad (12.3)$$

where this is normalized by the flight speed. The partial derivatives for the chain rule can be obtained directly from Equations 3.11a and 3.12a, after recalling the change in sign convention for x from positive in the flight direction in Section 3 to positive downstream in this section.

When the indicated manipulations have been performed, we arrive at the following formulas.

$$\left(\frac{w}{U} \right)_{\mu} = \alpha^{sw} + w_o + \sum_{m=1}^{\infty} \text{Re} \left(2w_m e^{imB\phi} \right) \quad (12.4)$$

$$\left(\frac{u}{U} \right)_{\mu} = u_o + \sum_{m=1}^{\infty} \text{Re} \left(2u_m e^{imB\phi} \right) \quad (12.5)$$

$$\left(\frac{v}{U} \right)_{\mu} = \left(\frac{v}{V} \right)^{sw} + v_o + \sum_{m=1}^{\infty} \text{Re} \left(2v_m e^{imB\phi} \right) \quad (12.6)$$

Where α^{sw} is the steady wake term discussed at some length in Section 7 and $(v/V)^{sw}$ is the corresponding wake term for the radial velocity. Note that there is no wake term in the u component. In applying these formulas, the program recognizes that the 2 wake terms exist only downstream of the rotor inside $z=1$. Elsewhere, they are equal to 0.

The nearfield wake harmonic components are given by

$$2w_m = \int_{z_h}^1 \text{Re} \int_{-\infty}^{\infty} e^{iawx\mu} \bar{X} e^{i\phi_{os}} \frac{B}{\pi\sigma^2 Z} \left\{ -a^2 B_D^2 t_b \Psi_v i\omega K_{\xi} J_n(\omega) \right. \\ \left. - \frac{1}{8Z_0} \Psi_L \frac{1}{\omega} [K_{\xi} K_{\xi 0} J_n(\omega) - n^2 \sigma_0^2 \sigma^2 J_n(0)] \right\} d\omega dz_0 \quad (12.7)$$

$$2u_m = \int_{z_h}^1 \text{Re} \int_{-\infty}^{\infty} e^{iawx\mu} \bar{X} e^{i\phi_{os}} \frac{aB}{\pi\sigma^2} \left[a^2 B_D^2 t_b i\omega^2 \Psi_v + \frac{1}{8Z_0} K_{\xi 0} \Psi_L \right] J_n(\omega) d\omega dz_0 \quad (12.8)$$

$$2v_m = \int_{z_h}^1 \text{Re} \int_{-\infty}^{\infty} e^{iawx\mu} \bar{X} e^{i\phi_{os}} \frac{B}{\pi} \left[-a^2 B_D^2 t_b \omega \Psi_v \frac{\partial}{\partial Z} J_n(\omega) \right. \\ \left. + \frac{1}{8Z_0} \Psi_L \frac{1}{\omega} \left[K_{\xi 0} \frac{\partial}{\partial Z} J_n(\omega) + n\sigma_0^2 \frac{\partial}{\partial Z} J_n(0) \right] \right] d\omega dz_0 \quad (12.9)$$

The notation in these formulas has the same meaning as in Section 7 with the exception that \bar{X} results from a Gaussian average over the field point in the axial direction rather than in the chordwise direction. It is given by

$$\bar{X} = \exp \left[- \left(\frac{\omega a \Delta}{4 \sqrt{1+n^2}} \right)^2 \right] \quad (12.10)$$

where Δ represents the width of the Gaussian function at its 1/2 amplitude points normalized by r_T .

The thickness and loading sources are represented by their transforms Ψ_v and Ψ_L as defined in Section 3. In the current version of the program, the section thickness distribution is approximated with a biconvex parabolic shape, whose transform was given in Section 10 as Equation 10.16. The loading transform is defined as follows

$$\Psi_L(k_x) = \int_{-1/2}^{1/2} \Delta C_P(X) e^{ik_x X} dX \quad (12.11)$$

This is similar to the definition used in the noise formulas in Section 3 except that Equation 3.74 was the transform of the loading shape only whereas Equation 12.11 includes the lift coefficient. In the program, Ψ_L is obtained by operating on the loading vector L_v that results from a performance calculation.

The nearfield wake harmonics given by Equations 12.7 to 12.9 are non-singular upstream of the blade leading edges and downstream of the trailing edges. Therefore, the radial integrals do not have to be divided into singular and non-singular ranges as they did for kernel function calculations.

SECTION 13

STUDIES WITH 3D UNSTEADY LIFT RESPONSE THEORY

In Sections 3 and 7 above, the unsteady lifting surface integral equation was derived relating fluctuating downwash at the blades to unsteady lift pressure. Section 9 explained the system for discretizing the equation and Section 10 showed how to invert it. This capability has been coded and delivered to NASA. Input to the program is described in Volume IV of this report and some applications to real geometry are given in Volume III. In this section, we show the results of some cases that were run to verify correct behavior of the theory by comparison with well-known 2D theories and then to explore how 2D and 3D results differ. The cases run are intentionally academic (constant chord blades) so as to concentrate on 3 dimensional and compressibility effects.

The following paragraphs describe the program's capability and limitations and interpretation of the input and output. Then cases for response to gusts and blade plunging motion in incompressible flow are compared with the Sears and Theodorsen 2D theories. Finally, a 10 per revolution frequency case is studied for effects of compressibility, sweep, and comparison with Amiet's 2D compressible gust response theory (ref. 34).

Program Capability and Limitations

As currently programmed, the code can deal rigorously with the following variations in geometry and operating conditions.

- The program predicts the unsteady lift pressure distribution caused by either non-uniform inflow, blade vibration, or any combination of the two. Any harmonic motion involving twist, camber and bending oscillation can be treated.
- The program deals with one frequency at a time. The user specifies the frequency in terms of P order (integer or fractional). Any physically permissible interblade phase angle can be run (input is in terms of number of nodal diameters).
- The theory is 3 dimensional with unshrouded blade tips and deals rigorously with blade interference, sweep, taper, and Mach number variations along the span (including supersonic tips).
- Bow and trailing shocks and their interaction with adjacent blades are represented as in linear supersonic wing theory.

There are some limitations to the code in its present configuration and also some limitations to the basic theory that should be noted.

- The theory is strictly linear. This means that the unsteady disturbances are not coupled to the steady induction except possibly in the circumferentially averaged sense by running at an adjusted advance ratio. Moment oscillations caused by a mid-chord oscillating shock would not be represented.

- The unsteady portion of the program does not deal with vortex loading. This may be a significant shortcoming because the small extra load due to a tip edge vortex could cause significant bending moments at the root.
- Frequencies are limited to about 20P (20 times the propeller rotation frequency) for the cases examined so far. This is not an intrinsic limitation and can probably be extended without much effort.

General Input/Output

Input falls into the categories of blade geometry, mean operating conditions, calculation parameters, and unsteady boundary conditions. This last category is treated in more detail under the subsection on Details of Panels and Input/Output and in the sections showing sample calculations. The major input items are

- Geometry
 - *Number of blades
 - *Radial distributions of Mid-Chord Alignment, Face Alignment Diameter, Hub/tip ratio, and Chord/diameter
- Operating Conditions:
 - *Advance ratio
 - *Flight Mach number
- Calculation Parameters:
 - *Number and location of control points
- Boundary Conditions:
 - *P order (frequency/prop rotation freq), q
 - *Number of nodal diameters
 - *Unsteady downwash velocity vectors (complex) at each control point

The program prints out the complex pressure coefficient ΔC_p , the centers of pressure for the real and imaginary parts of ΔC_p , and lift coefficient C_L . To recover a dimensional lift pressure, note that

$$\Delta P = \frac{1}{2} \rho_o U^2 \Delta C_p \quad (13.1)$$

where ρ_o is the ambient density and U is the section relative velocity such that

$$U^2 = V_x^2 + z^2 V_T^2 \quad (13.2)$$

V_x and V_T are the flight speed and tip rotational speed and z is radius ratio. The actual program representation is

$$U^2 = M_x^2 c_o^2 [1 + a^2 z^2] \quad (13.3)$$

where M_x is the flight Mach number, c_o is the ambient speed of sound, and $a = \pi/J$. Similarly, lift per unit span is

$$L = \frac{1}{2} \rho_o U^2 b C_L \quad (13.4)$$

where b is section chord.

Details on Panels and Input/Output

Figure 14 shows the load paneling system. The blade is divided into spanwise panels which are tapered at constant percent chord. The number of panels is specified by the variable NCP. The control points, where the flow tangency boundary condition is enforced, are at the midpoint of the panels in chordwise arrays at radii z_i . The index system for the control points is the same as in reference 2, namely that $i=1,2, \dots$ NSM counts the radial locations and $\bar{m} = 1,2, \dots$ NCP counts the chordwise positions. The current limits on NSM and NCP are 10 and 20, respectively. The downwash velocities are input as the vector W_μ where

$$\mu = (i-1)NCP + \bar{m} \quad (13.5)$$

and the velocities are normalized by the local section speed U.

The loading elements have spanwise and chordwise variations as follows. In the spanwise direction the variation is given by a series of shape functions or spanwise modes R_j as shown at the top right in Figure 14. For the chordwise variation, a series of overlapping triangular elements is used with some special treatment at the leading and trailing edges as shown at the lower right in Figure 14. At the leading edge, the user can choose the triangular element shown with the dashes (NBAROPT=1) or the preferred singular element (NBAROPT=2) shown by the solid line. The latter element is rigged so that, with the adjacent triangular element, it gives the correct leading edge behavior for 2D cases. At the trailing edge the basic element goes to 0 for subsonic trailing edges [$M_{re1} \cos(\text{trailing edge sweep angle}) < 0$] satisfying the Kutta condition. For supersonic edges a finite jump is allowed since the Kutta condition doesn't apply. There is a blending at the sonic radius between the 2 types of element.

The loading elements are simply shape functions. To find the actual loading they are multiplied by coefficients L_ν which must be determined by matrix inversion so as to satisfy the boundary conditions. The index ν is defined by

$$\nu = (j-1)NCP + \bar{n} \quad (13.6)$$

The associated loading is given by

$$\Delta C_p = \frac{1}{\sigma} \sum_{j, \bar{n}} L_\nu R_j(z) C_{\bar{n}}(X) \quad (13.7)$$

which is continuous in the chordwise direction and continuous and smooth in the spanwise direction. ΔC_p is printed and plotted with the computer run and is sent as a table to the noise program for unsteady loading input.

The loading ΔC_p and disturbance vector W are complex quantities. To interpret them as physical quantities, note that the downwash at any control point can be written

$$\frac{w}{U} = W e^{-iq\Omega t} = (w_r + iw_i) e^{-iq\Omega t} \quad (13.8)$$

where q is the P order (i.e. frequency normalized by the shaft rotation frequency).

The physical quantity is the real part of this, namely,

$$w_r \cos(q\Omega t) + w_i \sin(q\Omega t) \quad (13.9)$$

Similarly, the physical pressure coefficient and lift coefficient are the real parts of ΔC_p and C_L . For example, for the pressure the real part is

$$\Delta C_{p_{\text{real}}} \cos(q\Omega t) + \Delta C_{p_{\text{imag}}} \sin(q\Omega t) \quad (13.10)$$

Verification of Correct Response to Gusts and Plunging Motion

The first step in verification of the new blade pressure response theory is to compare predictions with results from well-known 2D lift response functions. This serves to check for any coding errors as well as to establish how the 3D flow differs from 2D strip behavior. The classic 2D unsteady lift response theories are Sears', in which the airfoil is rigid and the inflow contains a sinusoidal upwash gust field, and Theodorsen's, in which the inflow is steady and the airfoil executes a sinusoidal plunging motion. Both theories apply to linear, incompressible flow about zero thickness flat plate airfoils with no mean loading coupling. The text by Bisplinghoff, Ashley, and Halfman (Ref. 3) provides good background on the derivation and use of these theories. In each of the following 2 subsections, the results of the 2D theories are summarized first and then compared with 3D predictions.

Comparison with Sears Lift Response Function - Sears' results are outlined in Figure 20. The airfoil with chord b is fixed at the origin in a flow field with mean velocity U . Superimposed on U , and convected with it, is the upwash gust w described by

$$w = w_0 e^{i\omega(t - x/U)} \quad (13.11)$$

where the frequency f is $\omega/2\pi$. Here we use Sears' original convention with a + sign for time in the exponential ($+i\omega t$). Because $x = Ut$ is a constant phase point, it is clear the equation 13.11 represents a gust convected with the free stream.

The standard reduced frequency parameter is based on semi-chord

$$k_0 = \frac{\omega b/2}{U} \quad (13.12)$$

Since wavelength $\lambda = U/f$ and $\omega = 2\pi f$, the reduced frequency can also be interpreted in terms of chord to wavelength ratio:

$$k_0 = \frac{\pi b}{\lambda} \quad (13.13)$$

For a small steady upwash w_0 , the incidence angle is $\alpha = w_0/U$ and the lift coefficient is $C_L = 2\pi\alpha$. Sears' result for the unsteady case with $\alpha = w/U$ is

$$C_L = 2\pi\alpha S(k_0) \quad (13.14)$$

where $S(k_o)$ is the Sears function which describes the deviation in amplitude and phase from the steady theory. This is plotted in Figure 20 with reduced frequency as the parameter. It can be seen that the function goes to 1 at 0 frequency, as required, and diminishes in amplitude at higher frequencies. The phase first leads the input then lags as frequency is increased.

Input for the gust cases was prepared as follows. With the $-i\omega t$ sign convention used for the 3D analysis, a sinusoidal gust is described by

$$w = w_o e^{i\omega(\gamma/U - t)} \quad (13.15)$$

where γ is a streamwise coordinate measured in the helicoidal advance surface at constant radius. γ corresponds to x in the 2D discussion above. The input vector W is obtained by dropping the $\exp(-i\omega t)$ and normalizing by the local section speed U to get the upwash angle:

$$W = \frac{w}{U} = \frac{w_o}{U} e^{i\omega\gamma/U} \quad (13.16)$$

w_o/U was set to 1 for a 1° gust amplitude. We substitute $\omega = q\Omega$, $x = bX_{\bar{n}}$, $b = 2r_T B_D$, $\Omega r_T/V = a$, and $U/V = \sigma$ with the result

$$W = \cos\left(\frac{2qaB_D}{\sigma} X_{\bar{n}}\right) + i \sin\left(\frac{2qaB_D}{\sigma} X_{\bar{n}}\right) \quad (13.17)$$

which is to be evaluated at the non-dimensional chordwise locations

$$X_{\bar{n}} = -0.5 + (\bar{n} - 0.5)/NCP \quad (13.18)$$

where \bar{n} runs from 1 to NCP. 10 control points were arrayed across the 0.7 radius line so that $NCP = 10$ and $NSM = 1$. Cases for the geometry shown in Figure 21 were calculated for P orders from 0 to 20 with the results shown in comparison with the Sears function. To interpret the P order in terms of reduced frequency, the same substitutions used for Equation 13.17 can be used with the definition of k_o with the result

$$k_o = \frac{qaB_D}{\sigma} \quad (13.19)$$

For plotting on Figure 21, the lift output from the 3D lifting surface program was normalized by $2\pi\alpha$, which amounts to dividing by 0.1097 after converting to radians. Furthermore, the complex conjugate is plotted because of the difference in conventions on the sign of $i\omega t$ in the exponentials of Equations 13.8 and 13.11.

The comparison of 2D and 3D results in Figure 21 can be interpreted as follows. In the limit as frequency goes to 0, the steady result for a twisted flat plate blade is reached. The lift is about 1/2 of the 2D result because of the 3D induction. This lift reduction corresponds to the aspect ratio effect, well known in steady wing theory. At the high end of the frequency range, $20P$, the 3D lift approaches the 2D value (at least away from the ends of the blade). This effect is also well known in unsteady wing theory (Ref. 35) and is a very satisfying check of the 3D theory.

Since the high and low frequency ends of the 3D curve in Figure 21 could have been predicted a priori, the valuable part of the result is in the detail of the transition from steady 3D behavior at low frequencies to unsteady 2D behavior at high frequencies. The surprise was that at 1P there is almost no effect of unsteadiness. Thus, for this incompressible, unswept case, the 3D lifting surface theory gives results which should depart only minutely from a quasi-steady lifting line calculation. This is an important discovery and answers questions regarding unsteady lift response effects in 1P calculations that have been raised over the past 30 years. In the past at Hamilton Standard, various analysts have attempted to account for unsteadiness by doing a multi-azimuth steady lifting line calculation and then adjusting the amplitude and phase in a strip-wise sense by using the Sears function. Figure 21 shows clearly that this is not correct and that, fortuitously, the quasi-steady calculations should be adequate for 1P and 2P, at least for this unswept case.

This conclusion regarding unsteady effects can at this point only be applied rigorously to the cases run so far and shown in Figure 21. However, based on other experience, we would expect it to apply also up to high subsonic tip speeds for straight blades. It is recommended, however, that this be explored further by trying more cases so that rules of thumb can be developed on the limits where quasi-steady multi-azimuth calculations can be considered accurate.

The final portion of the Sears function check is a comparison of 2D results with 3D unsteady pressure distributions calculated by the program. Sears' theory modifies the flat plate steady results in amplitude and phase only. The shape of the pressure distribution stays the same:

$$\Delta C_p = 4\alpha \sqrt{\frac{1-x}{x}} S(k_0) \quad (13.20)$$

Comparisons are given in Figure 22. As might be expected, the 2D and 3D pressure agree closely at the high frequencies (20P) where the lift coefficients matched. This applies to both the real and imaginary parts (in phase and out of phase) and to the detailed behavior near the leading edge. At lower frequencies the pressures depart from the 2D results in a way that is consistent with the lift predictions.

The distributions at the upper right in Figure 22 have the shape given by the radical in Equation 13.20 with the characteristic square root singularity at the leading edge and the zero (Kutta condition) at the trailing edge. Later in this section, distributions with these characteristics are referred to as "flat plate like."

Comparison with Theodorsen Theory for Plunging Airfoils - Results of Theodorsen's theory for the plunging airfoil problem are outlined in Figure 23, which includes several parameters defined in the Sears discussion above. Here the upstream airflow is steady and the airfoil is executing an oscillating vertical motion given by

$$h = h_0 e^{i\omega t} \quad (13.21)$$

The effective unsteady angle of attack caused by this motion is

$$\alpha = \dot{h}/U \quad (13.22)$$

Theodorsen's theory deals with various kinds of motion, but his result for unsteady lift in the plunging problem is

$$C_L = 2\pi\alpha[C(k_0) + ik_0/2] \quad (13.23)$$

where $C(k_0)$ is the Theodorsen function as given in Ref. 3. $C_L/2\pi\alpha$ is plotted in Figure 23 with reduced frequency k_0 as the parameter. At the low frequency end of the curve, the value is 1, corresponding to steady, 2D airfoil lift. For increasing frequency, the lift first leads the motion and then lags. At high frequency the lift continues to increase because of the inertial mass effect.

For verification of the 3D theory, the same propeller and same mean conditions were used as with the Sears theory above. Since the motion is constant along the chord, the input unsteady boundary condition for the program is simply 1's at all 10 chordwise control points corresponding to a 1° effective angle of attack due to the airfoil motion. Again, for comparison with Figure 24, the output lift coefficient from the program is divided by 0.1093 to normalize by $2\pi\alpha$ and the complex conjugate is taken. As with the Sears theory, the 3D results exhibit an aspect ratio effect at low frequency and approach the 2D curve at high frequency. This general behavior is to be expected from wing experience (Ref. 35).

Theodorsen's unsteady pressure distribution for the plunging problem can be deduced from Reference 3:

$$\Delta C_p = 4\alpha \left[\sqrt{\frac{1-x}{x}} C(k_0) + i 2k_0 \sqrt{x(1-x)} \right] \quad (13.24)$$

Figure 25 shows the comparison between 2D unsteady pressure predictions from Equation 13.24 and predictions from the 3D unsteady theory. As with the Sears' theory, 3D results approach the 2D unsteady theory at high frequency and differ significantly at low frequency.

10P Cases for Noise Analysis at Takeoff Conditions

The test cases presented above for checkout against 2D incompressible theory were run with control points at only one radial station. We now examine a series of 3 cases run with 10 control points across the chord at each of 7 radii to find how the 3D flow compares with the 2D strip theory currently in use for noise predictions. These cases include compressibility at Mach numbers and advance ratios typical of takeoff. To minimize the number of effects in the study, the blade again has constant chord as shown in Figure 26. There are 5 blades and the interblade phase angle is 0 as would be the case for a 5x5 CRP. The frequency is 10P, which is the fundamental interaction frequency for counter-rotation interaction. Flight Mach number is 0.26 and the gust amplitude is 1° from root to tip in all cases.

The 10P series is shown in Figures 26 to 29. Figure 26 is a base case with no sweep and a J for a low tip relative speed (0.64 Mach). The shape of the pressure distribution follows the typical flat plate behavior expected for low Mach number and frequency. Amplitude and phase effects will be examined shortly.

The next case considered is for swept blades. To evaluate the boundary conditions for program input, we consider the same gust given by Equation 13.15. With the blade swept back in the gust field by an amount MCA, the blade sees the gust at

a time lagged by $\Delta t = MCA/U$. Thus, t in Equation 13.15 can be replaced by $t - \Delta t$. The associated phase lag is $\omega\Delta t$, or in non-dimensional terms

$$\Delta\phi = \frac{2qa}{\sigma} \frac{MCA}{D} \quad (13.25)$$

which changes the input vector from Equation 13.17 to

$$W = W_0 \left[\cos \left(\frac{2qaB_D}{\sigma} X_n + \frac{2qa}{\sigma} \frac{MCA}{D} \right) + i \sin \left(\frac{2qaB_D}{\sigma} X_n + \frac{2qa}{\sigma} \frac{MCA}{D} \right) \right] \quad (13.26)$$

Figure 27 shows results for a uniform 45° sweep. There are rapid phase variations along the span; however, both the in phase and out of phase distributions have flat plate like behavior. At radii where the pressure is in transition from positive to negative, the unusual shapes are probably simply an indication that the pressure doesn't change sign simultaneously along the chord.

Results from the previous 2 figures are summarized in terms of lift amplitude and phase in Figure 28. At the top, the reduced frequency and section relative Mach number distributions with radius are shown for reference. The middle panel shows the magnitude of the lift coefficient compared with Amiet's compressible lift response function (Ref. 34) used in a strip sense. It can be seen that the strip method is a good approximation for the straight blade over all of the span except for the tip where some 3D relief is found. The results for the swept case show some lift reduction in the mid-blade area, which, of course, is a benefit for noise. The phase comparison is given at the bottom of Figure 28. For the swept blade comparison, Amiet's phase is lagged by an amount corresponding to how far the blade sections are moved back in the gust field. For both the straight and swept cases, Amiet's theory used in strip fashion agrees well with the 3D theory in the mid-blade area but deteriorates toward the tip.

Figure 29 shows results for a straight blade at higher tip Mach number. Here the pressure distributions depart significantly from the simple Sears shape. At the tip, there are some oscillations along the chord, which also occur in the 2D compressible theory although no quantitative comparisons have yet been made. In the root area there are also some unusual shapes, presumably caused by cascade effects.

The conclusion from these 3 cases is that the Hamilton Standard strip methods could be adequate at the 10P frequency for low tip Mach number. Higher frequencies and Mach numbers need further exploration.

SECTION 14

CONCLUDING REMARKS

Theoretical equations have been developed for computation of noise and aerodynamics of propellers associated with blade loading and thickness. Derivations were based on the acoustic analogy and the acceleration potential method and therefore are basically linear. However, in the case of propeller steady performance, non-linearity associated with the axial mass flux is crucial and a correction method was presented. This essentially linearizes the induced velocity about a mean flow through the rotor that satisfies the axial momentum equation on a circumferentially averaged basis.

To a large extent this volume extends and formalizes theory for aerodynamics and noise that has been presented by the author in various technical papers. Wherever possible, the relationship between formulas developed herein and previously published work is shown. In some cases, the formulas are equivalent but with a different notation; in other cases, the formulas presented herein are more general than those in previously published work but reduce to the earlier theories when the correct restrictions are applied.

This volume is mainly theoretical and presents little in the way of computed results. However, Section 13 does show some calculations verifying correct behavior of the 3D unsteady lift theory in comparison with traditional 2D methods. Verification of the theory by comparison with test data is the subject of Volume III of this report. Volume IV is a user's manual for the computer code.

SECTION 15

REFERENCES

1. Clark, B. J. and Scott, J. R., "Coupled Aerodynamic and Acoustical Predictions for Turboprops", NASA Technical Memorandum 87094, 1984.
2. Korkan, K. D. and Forsyth, D. W., "Numerical Analysis of Propeller Noise in the Near and Far Field", AIAA Paper No. 86-1875, Presented at AIAA 10th Aeroacoustics Conference, Seattle, Washington, July 9-11, 1986.
3. Bisplinghoff, R. L., Ashley, H., and Halfman, R. L., Aeroelasticity, Addison-Wesley Publishing Company, Reading, Massachusetts, 1955.
4. Bisplinghoff, R. L. and Ashley, H., Aeroelasticity, Wiley, 1962.
5. Landahl, M. T., and Stark, V. J. E., "Numerical Lifting Surface Theory - Problems and Progress, AIAA Journal, Vol. 6, No. 11, November, 1968.
6. Namba, M., "Lifting Surface Theory for a Rotating Subsonic or Transonic Blade Row", Aeronautical Research Council Reports and Memoranda, R&M 3740, Her Majesty's Stationery Office, London, 1974.
7. Lordi, J. A. and Homicz, G. F., "Linearized Analysis of the Three-Dimensional Compressible Flow through a Rotating Annular Blade Row," Journal of Fluid Mechanics, Vol 103, Feb. 1981, pp. 413-442.
8. Kondo, K., "On the Potential-Theoretical Fundamentals of the Aerodynamics of Screw Propellers at High Speed," Journal of the Faculty of Engineering, University of Tokyo, Vol. 25, 1957.
9. Tsakonas, S., "Propeller Blade Pressure Distribution due to Loading and Thickness Effects," Journal of Ship Research, Vol. 23, June 1979, pp. 89-107.
10. Hanson, D. B., "Near Field Noise of High Tip Speed Propellers in Forward Flight", AIAA Paper 76-565, 1976.
11. Hanson, D. B., "Helicoidal Surface Theory for Harmonic Noise of Propellers in the Far Field", AIAA Journal, Vol. 18, No. 10, October 1980, pp. 1213-1220.
12. Hanson, D. B., "Influence of Propeller Design Parameters on Far-Field Harmonic Noise in Forward Flight", AIAA Journal, Vol. 18, No. 11, November 1980, pp. 1313-1319.
13. Hanson, D. B., "Near-field Frequency Domain Theory for Propeller Noise", AIAA Journal, Vol. 23, No. 4, April 1985, pp.499-504.
14. Hanson, D. B., "Noise of Counter-Rotation Propellers", Journal of Aircraft, Vol. 22, No. 7, July 1985, pp.609-617.
15. Hanson, D. B., "Compressible Helicoidal Surface Theory for Propeller Aerodynamics and Noise," AIAA Journal, Vol. 21, No. 6, June 1983, pp. 881-889.
16. Hanson, D. B., "Compressible Lifting Surface Theory for Propeller Performance Calculation," Journal of Aircraft, Vol. 22, No. 1, January 1985, pp. 19-27.

17. Kerwin, J. E., "Marine Propellers", Annual Reviews of Fluid Mechanics - 1986, Vol. 18, Annual Reviews, Inc., 1986.
18. Yuasa, H. and Ishii, N., "Leading Edge Separating Vortex and Pressure Distributions on Propeller Blades," Proceedings of the Second International Symposium on Flow Visualization, Bochum, West Germany, Sept. 1980, p. 256, Hemisphere Publishing Corp. New York, 1982.
19. Vaczy, C. M. and McCormick, D. C., "A Study of the Leading Edge Vortex and Tip Vortex on Prop-Fan Blades," ASME Journal of Turbomachinery, Vol. 109, July 1987, pp. 325-331.
20. Stefko, G. L., Rose, G. E., and Podboy, G. G., "Wind Tunnel Performance Results of an Aeroelastically Scaled 2/9 Model of the PTA Flight Test Prop-Fan," AIAA Paper Number 87-1893, 1987.
21. Polhamus, E. C., "A Concept of the Vortex Lift of Sharp-Edge Delta Wings Based on a Leading-Edge-Suction Analogy", NASA TN D-3767, 1966.
22. Lamar, J. E., "Prediction of Vortex Flow Characteristics of Subsonic and Supersonic Speeds," J. Aircraft, Vol. 13, No. 7, p. 490, 1976.
23. Goldstein, M. E., Aeroacoustics, McGraw-Hill Book Co., New York, 1976.
24. Magnus, W. and Oberhettinger, F., and Pal Soni, R., Formulas and Theorems for the Special Functions of Mathematical Physics, 3rd Edition, Springer-Verlag, New York, 1966.
25. Handbook of Mathematical Functions With Formulas, Graphs, and Mathematical Tables, Abramowitz, M. and Stegun, I. A., Editors, U.S. Department of Commerce-National Bureau of Standards Applied Mathematics Series 55, 1964.
26. Hanson, D. B., "Propeller Noise Caused by Blade Tip Radial Forces", AIAA Paper No. 86-1892, presented at AIAA 10th Aeroacoustics Conference, July 9-11, 1986, Seattle, Washington.
27. Ashley, H. and Landahl, M. T., Aerodynamics of Wings and Bodies, Addison-Wesley, Reading, Massachusetts, 1965.
28. Morse, P. M. and Ingard, K. U., Theoretical Acoustics, McGraw-Hill Book Co., New York, 1968.
29. Champeney, D.C., Fourier Transforms and their Physical Applications, Academic Press, 1965.
30. Goodman, T. R., "Comments on Jacobs and Tsakonas: 'Propeller Loading-Induced Velocity Field by Means of Unsteady Lifting Surface Theory'", Journal of Ship Research, Vol. 26, No.4, December, 1982, pp. 266-268.
31. McCormick, B. W., Aerodynamics of V/STOL Flight, Academic Press, New York, 1967.
32. Vogeley, A. W., "Axial-Momentum Theory for Propellers in Compressible Flow", NACA Tech Note 2164, 1951.

33. Weick, F. E., Aircraft Propeller Design, McGraw-Hill, New York, 1930.
34. Amiet, R. K., "Computer Programs for Calculation of the Forces on and Sound Produced by an Airfoil in a Turbulent Flow", UTRC Report # R76-111204-1, June 1976.
35. Jordan, P. F., "Reliable Lifting Surface Solutions for Unsteady Flow", AIAA Paper Number 78-228, AIAA 16th Aerospace Sciences Meeting, Huntsville, Alabama, January 1978.

SECTION 16

LIST OF SYMBOLS

There are a few symbols not included in this list that are used only within a page or so of the point where they are defined.

- a = tip rotational speed/flight speed = π/J
- b = blade section chord measured at constant radius - see Figure 3.1
- c_o = ambient speed of sound
- \underline{f} = body force in wave equation
- f_j = j^{th} component of force/unit volume on fluid
- \hat{f}_j = j^{th} component of force/unit area on blade
- h = section thickness distribution in Section 3, camber distribution in Section 10; section vertical displacement in Section 13
- i = $\sqrt{-1}$, also index for control points in radial direction when used as a subscript
- j = index for radial mode shapes, R_j
- k = number of nodal diameters in unsteady loading pattern - related to interblade phase angle - see discussion with Equation 3.80
- k_o = reduced frequency - Equation 13.12ff
- k_x = normalized axial wavenumber - Equation 3.102
- k_y = wavenumber for sound calculation - defined in various contexts in Sections 4 and 5
- k_γ = chordwise wavenumber - Equation 3.9
- m = harmonic index, nB for steady loading, nB-k for unsteady loading
- p = disturbance pressure
- p_2 = pressure field of rear rotor
- q = source(monopole) strength in Section 3, unsteady loading order elsewhere. Loading frequency is $q\Omega/2\pi$
- r = radius in cylindrical coordinates, radiation distance in Sections 5 and 6 only
- r_T = tip radius
- t = time

t_b = ratio of section max thickness to chord
 u = component of disturbance velocity parallel to the local section advance direction
 v = component of disturbance velocity in radial direction
 w = component of disturbance velocity normal to advance direction - the downwash (negative down)
 x = distance forward of pitch change axis in acoustic sections (Sections 3 - 6), distance downstream of pitch change axis in aerodynamic sections (Sections 7 - 12)
 $x_{\mu\nu}$ = x coordinate for evaluating kernel function elements
 Δx = axial distance between load panel and field point
 y = spanwise distance in wing discussions, sideline distance to field point in noise formulas
 z = radius ratio for field point or observer position
 z_o = radius ratio for source integration
 B = number of blades
 B_D = b/D , chord to diameter ratio
 C_L = section lift coefficient
 C_D = section drag coefficient
 C_R = coefficient of radial tip force - Equation 5.44ff
 $C_{\bar{n}}$ = load element shape functions - see Figure 9.1
 ΔC_p = coefficient of lift pressure
 D = propeller diameter
 E = various exponentials - defined locally
 F = body force in momentum equation
 FA = face alignment measured at constant radius - see Figure 3.1
 G = Gaussian averaging function for control points - Equation 9.21
 H = Heavyside or unit step function - 0 for argument < 0 , 1 for argument > 0 . Also, normalized section chordwise thickness distribution - see Figure 3.3
 $H_n^{(1)}$ = $J_n + iY_n$, Hankel function of first kind
 $H_n^{(2)}$ = $J_n - iY_n$, Hankel function of second kind

I_n = modified Bessel function of first kind.
 J = advance ratio, $V/[(\text{revs/unit time}) * D]$
 J_n = ordinary Bessel function of first kind
 $JH_n(\omega)$ = Bessel function product defined in Equation 7.27
 K = normalized radial wavenumber - Equation 3.55
 K_n = modified Bessel function of second kind - Equation 3.17
 K_r = radial wavenumber - Equation 3.36
 K_x = σk_γ , axial wavenumber
 K_ξ , etc. = wavenumbers defined in Equations 7.17 - 7.20
 $K_{\mu\nu}$ = kernel function elements
 L_ν = loading coefficient - see Equation 9.25
 M_x = flight Mach number
 M_r = σM_x , section helical Mach number
 M_t = $\Omega r_t / c_o$, tip rotational Mach number
MCA = mid-chord alignment or sweep of section - see Figure 3.1
NCP = number of loading panels
NSM = number of spanwise mode shape functions
 Q = torque in performance section
 R = source to observer distance in Green's function
 R_o = see Equation 3.34
 S = source strength - see Equation 3.2.
 T = Thrust
 U = blade section relative speed, = σV
 V = flight speed
 \bar{V} = mean flow speed through propeller disc - a function of radius ratio
 W_μ = vector of downwash angles at control points
 X = normalized chordwise distance, zero at mid-chord
 Y_n = ordinary Bessel function of second kind

- α = induced flow angle - relative to section advance direction
 β = $\sqrt{1 - M_x^2}$
 γ = coordinate at constant radius in section advance direction-see Figure 3.1
 δ = Dirac delta function (impulse function)
 δ_{mn} = Kroneker delta, 1 for equal subscripts, 0 for unequal
 ϕ = angle in cylindrical coordinates to field point
 ϕ_o = angle in cylindrical coordinates to source point in translating, but not rotating, system
 ϕ_1 = angle to field point in blade-fixed system
 ϕ_{FA} = phase angle associated with face alignment - Equation 3.104
 ϕ_s = phase angle associated with sweep - Equation 3.62
 ϕ_x = phase angle associated with axial position of field point - Equation 3.78
 ϕ_{os} = $\phi_{FA} + \phi_s$
 ϕ_{osx} = $\phi_{FA} + \phi_s + \phi_x$
 $\hat{\phi}$ = see Equation 7.31
 μ = index for control points - see Equation 9.17
 ν = index for load elements - see Equation 9.24
 θ = angle from flight direction for acoustic equations
 ρ_o = ambient density
 η = apparent efficiency in propeller performance
 σ = $\sqrt{1+a^2z^2}$, ratio of local blade section speed to flight speed at field point radius
 σ_o = $\sqrt{1+a^2z_o^2}$, ratio of local blade section speed to flight speed at source point radius
 w = wavenumber integration variable for axial direction
 w_o = (unsteady loading frequency) times 2π
 ξ = distance normal to local section advance direction measured at constant radius - see Figure 3.1
 ψ = source transforms defined in Section 3, with various subscripts
 τ = source time integration variable in Green's function

- Φ = velocity potential
- Γ = γ/r_t
- Γ_o = γ_o/r_t
- Π = sound power in Section 6
- Ω = propeller angular speed, 2π x shaft rotation frequency
- Ψ = normalized versions of ψ
- Ψ_F = loading source transform - Equations 3.72 and 3.69
- Ψ_n = combined loading and thickness transform - Equation 3.69

UNDERBAR

denotes vector quantity as in \underline{F}

OVERBAR

denotes average quantity

SUBSCRIPTS

- i = index for radial position of control points
- k = k^{th} loading harmonic
- n = n^{th} sound harmonic
- o = denotes source coordinate or properties
- T = denotes tip position
- h = denotes hub position
- $<$ = smaller of r, r_o or z, z_o
- $>$ = larger of r, r_o or z, z_o

INTEGRALS

- \oint = denotes Mangler principal value for integral

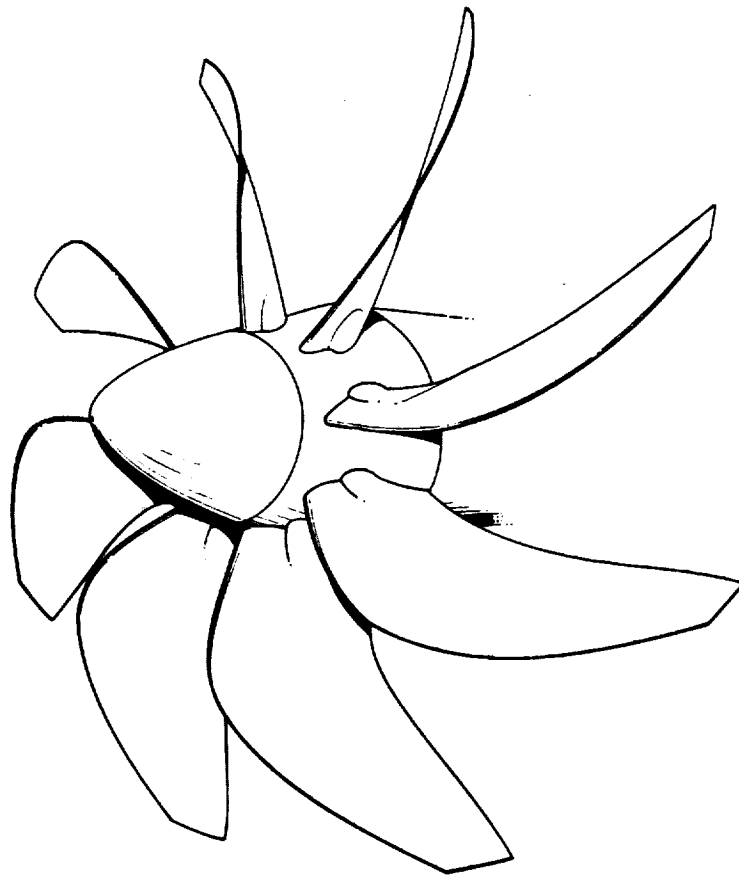


Figure 1. Prop-Fan model SR3.

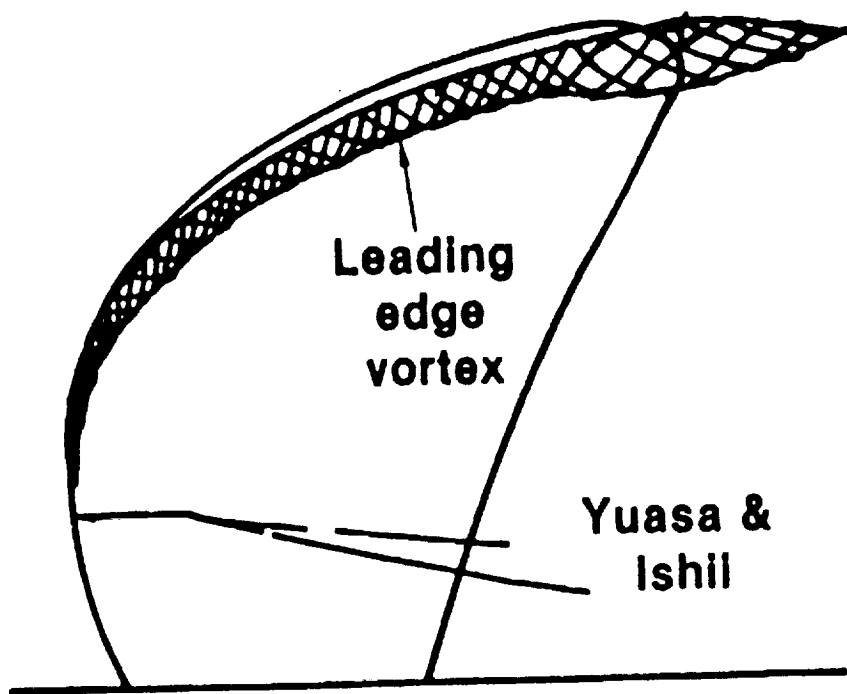


Figure 2. Vortex flow visualization on a simulated marine propeller in a water tunnel. (from Reference 18)

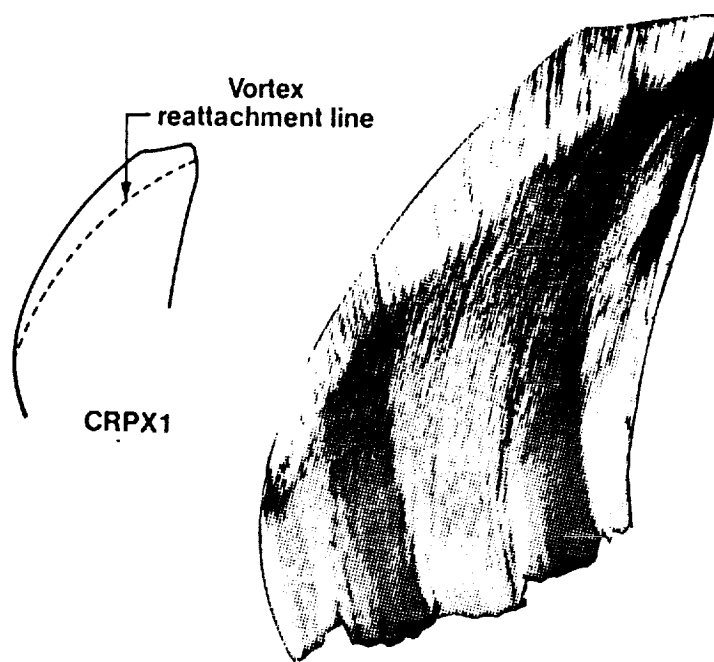


Figure 3. Flow visualization results for CRPX1 at take off condition. Change in streak direction indicates vortex reattachment line.

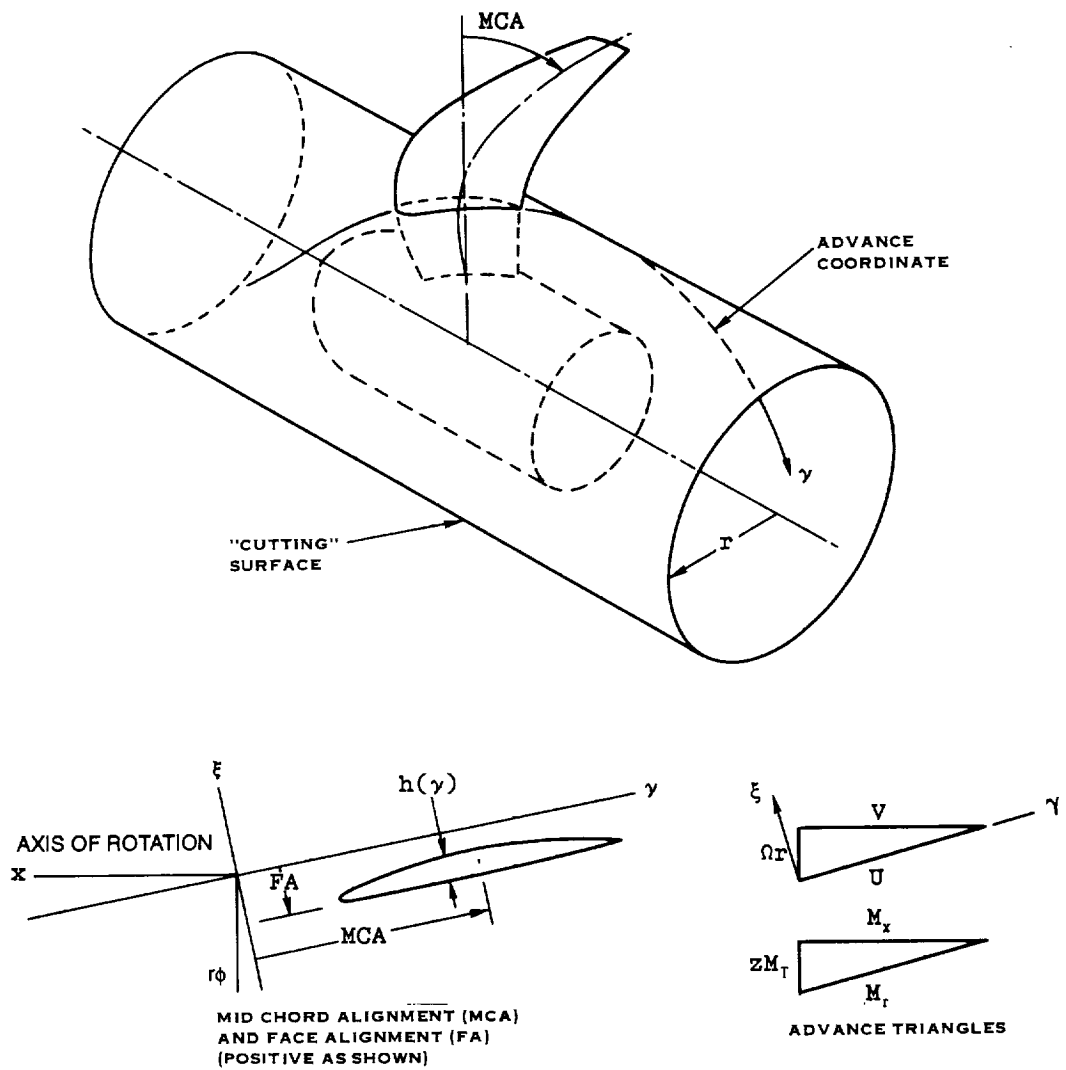


Figure 4. Cylindrical "cutting" surface for blade section definition and for definition of advance coordinate γ .

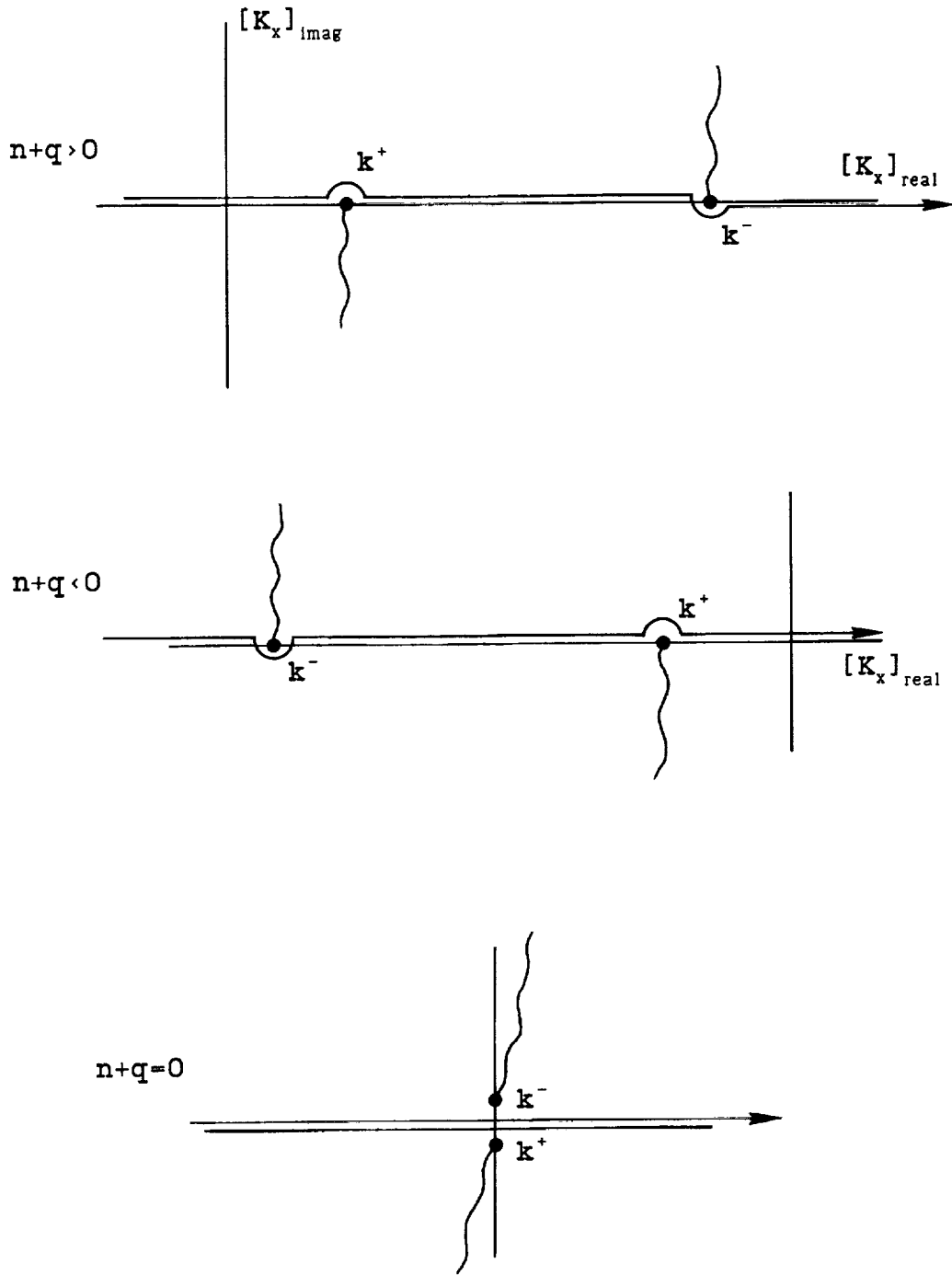


Figure 5. Branch cuts of radial wavenumber $K_r = \sqrt{K_x^2 M_x^2 - [K_x - (n+q)\frac{\Omega}{V}]^2}$ and integration path for axial wavenumber K_x .

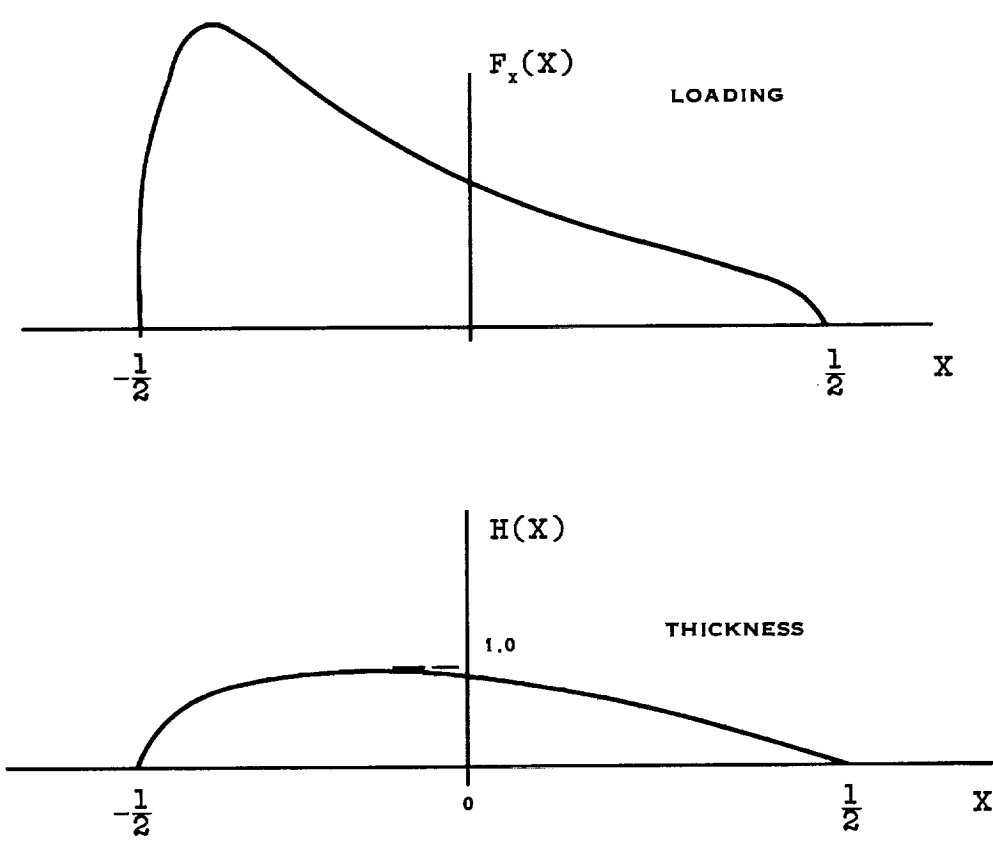


Figure 6. Normalized section loading and thickness distribution functions, $F_x(X)$ and $H(X)$.

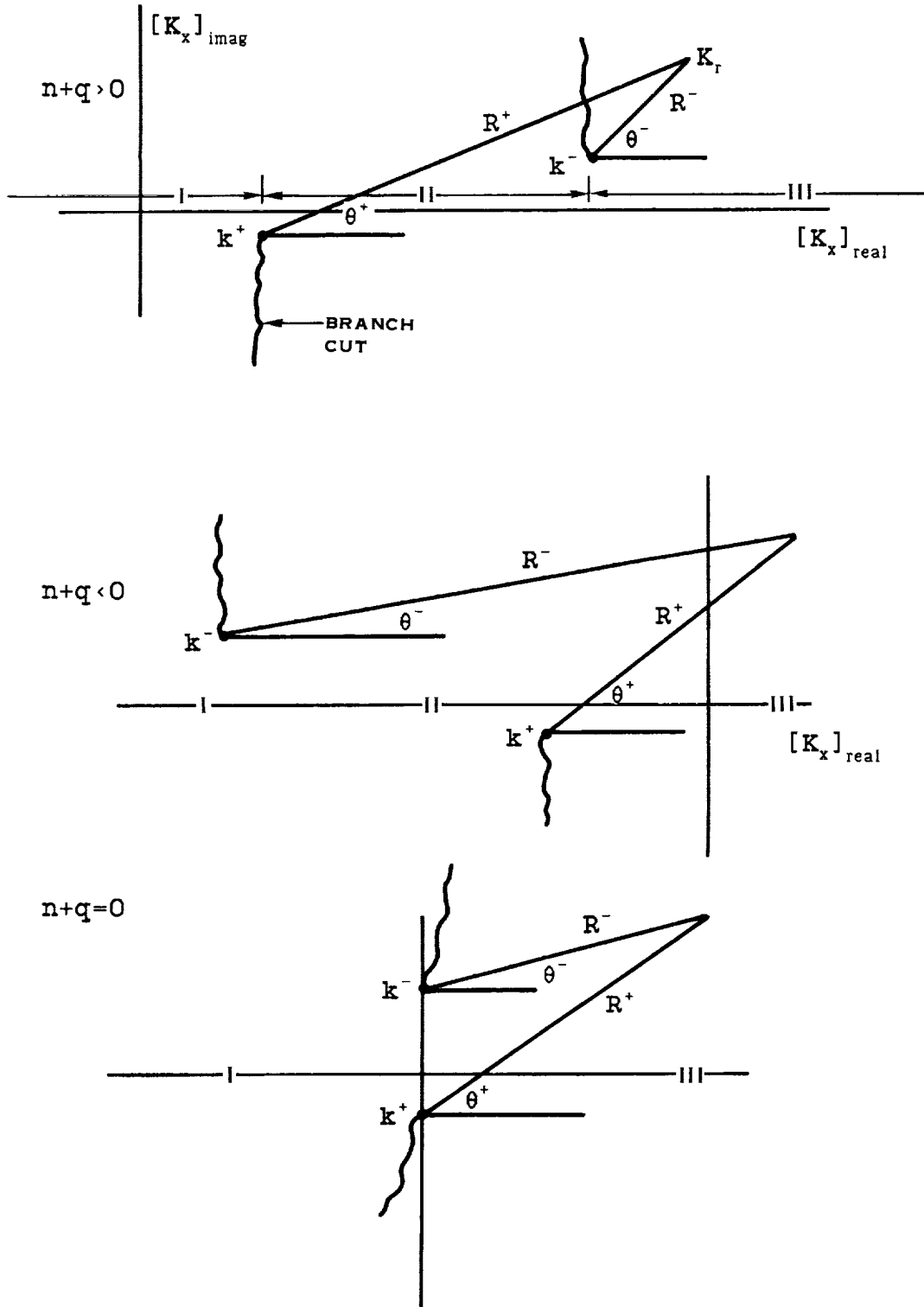


Figure 7. Branches of square root in radial wavenumbers K_r and K .

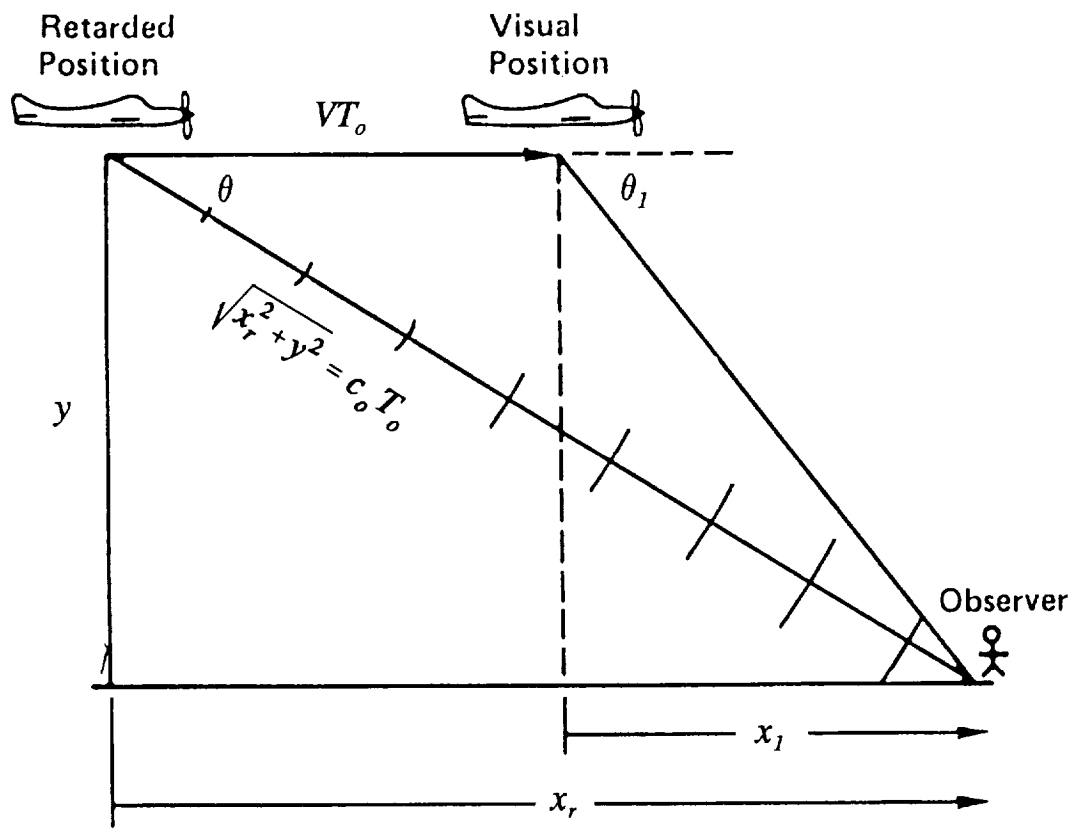


Figure 8. Retarded and visual coordinates.

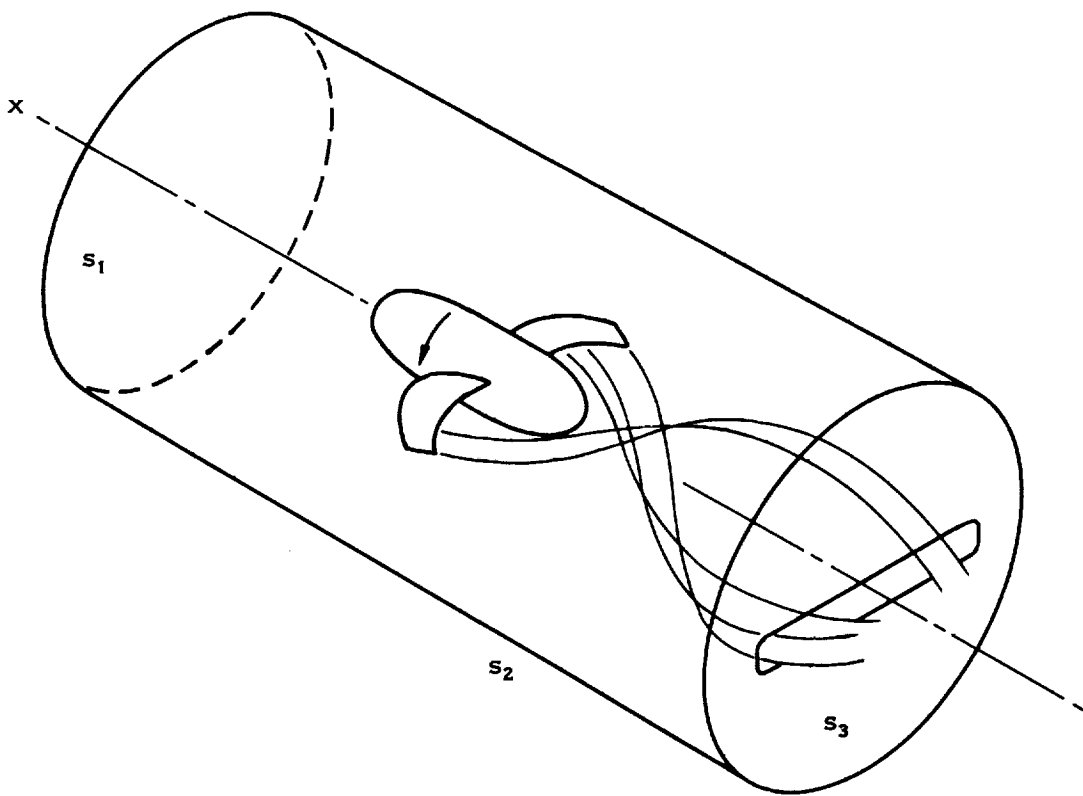


Figure 9. Control surface for wave drag and vortex drag theory.

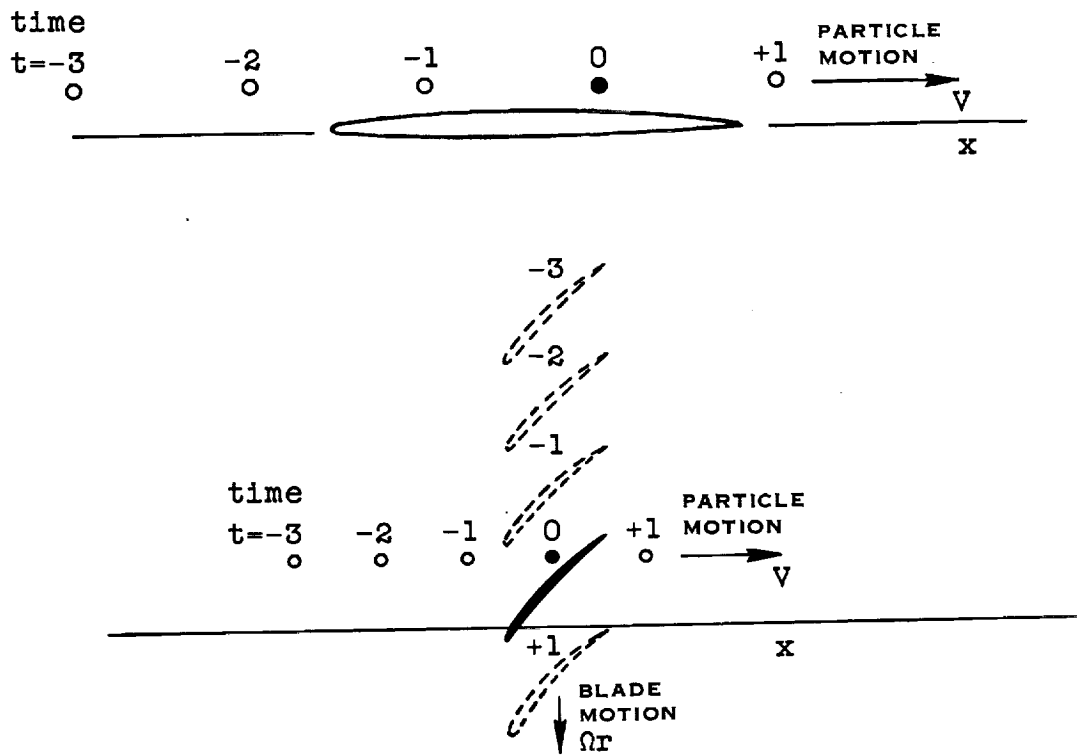


Figure 10. Passage of fluid particle past fixed wing and through rotating rotor. Particle misses airfoil in both cases. Particle path not deflected in linear theory.

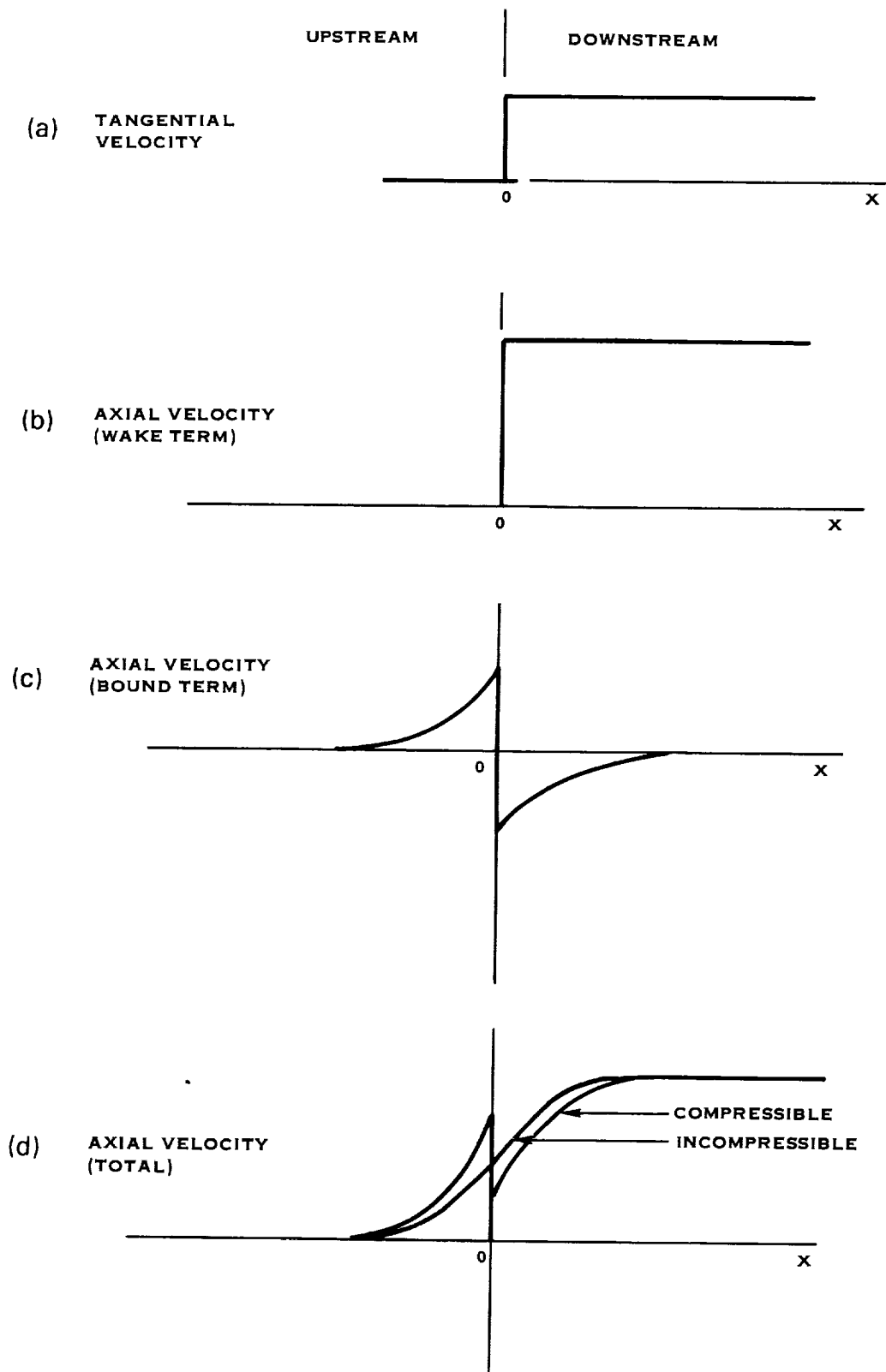


Figure 11. Actuator disc induction velocity components.

AXIAL INDUCED VELOCITY v/V_0

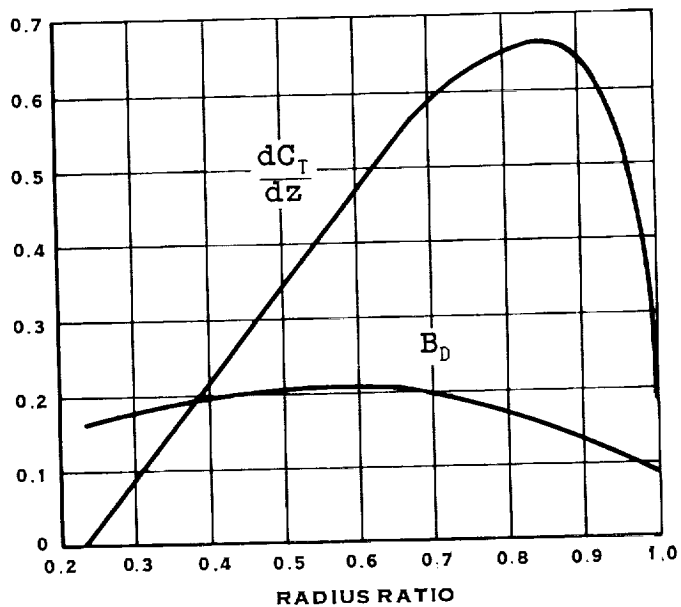
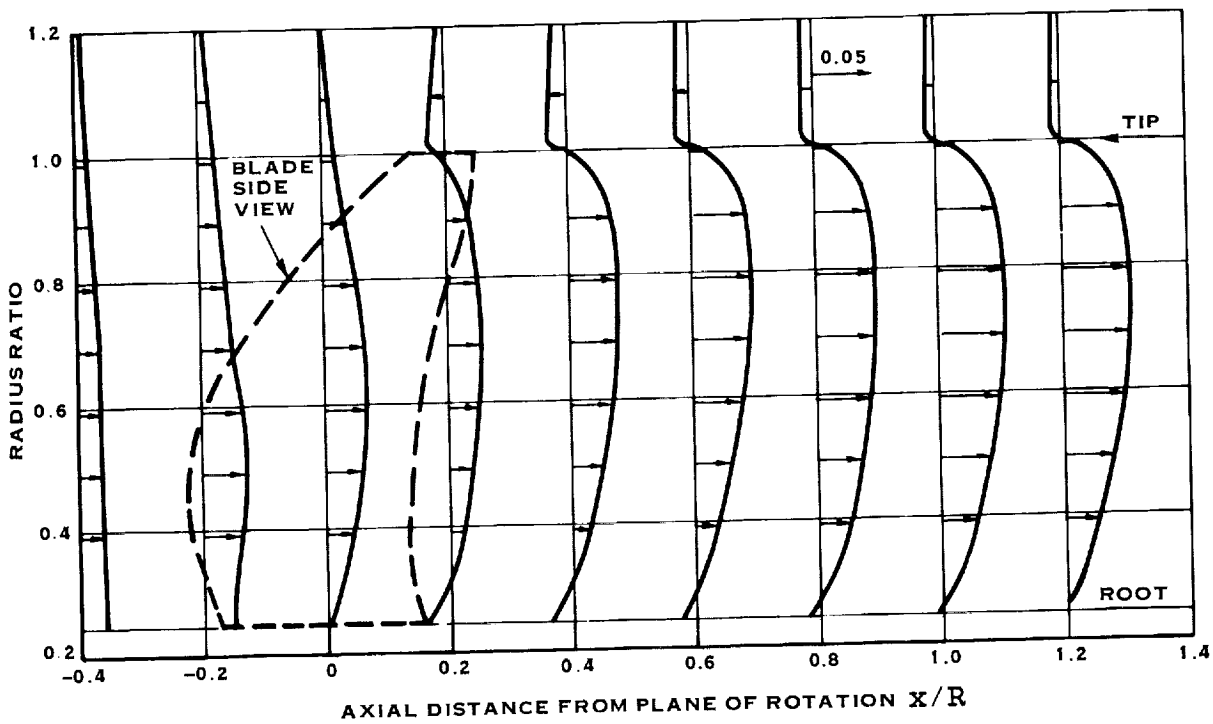


Figure 12. Sample calculation of axial induced velocity for typical Prop-Fan geometry. Note developing jet and forward induction outside the tip radius.

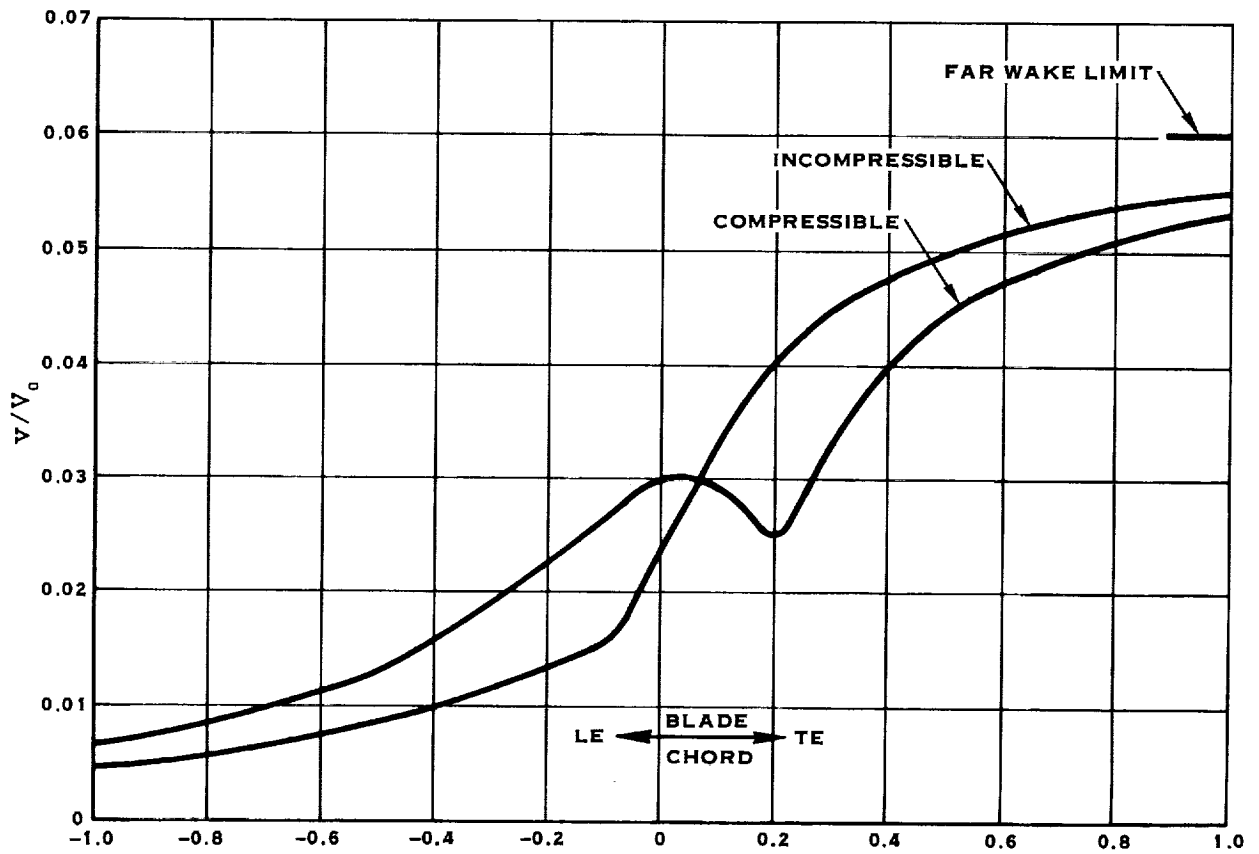


Figure 13. Axial induced velocity distribution for rotor from previous figure at radius ratio $z = 0.78$. Flight Mach number = 0.72.

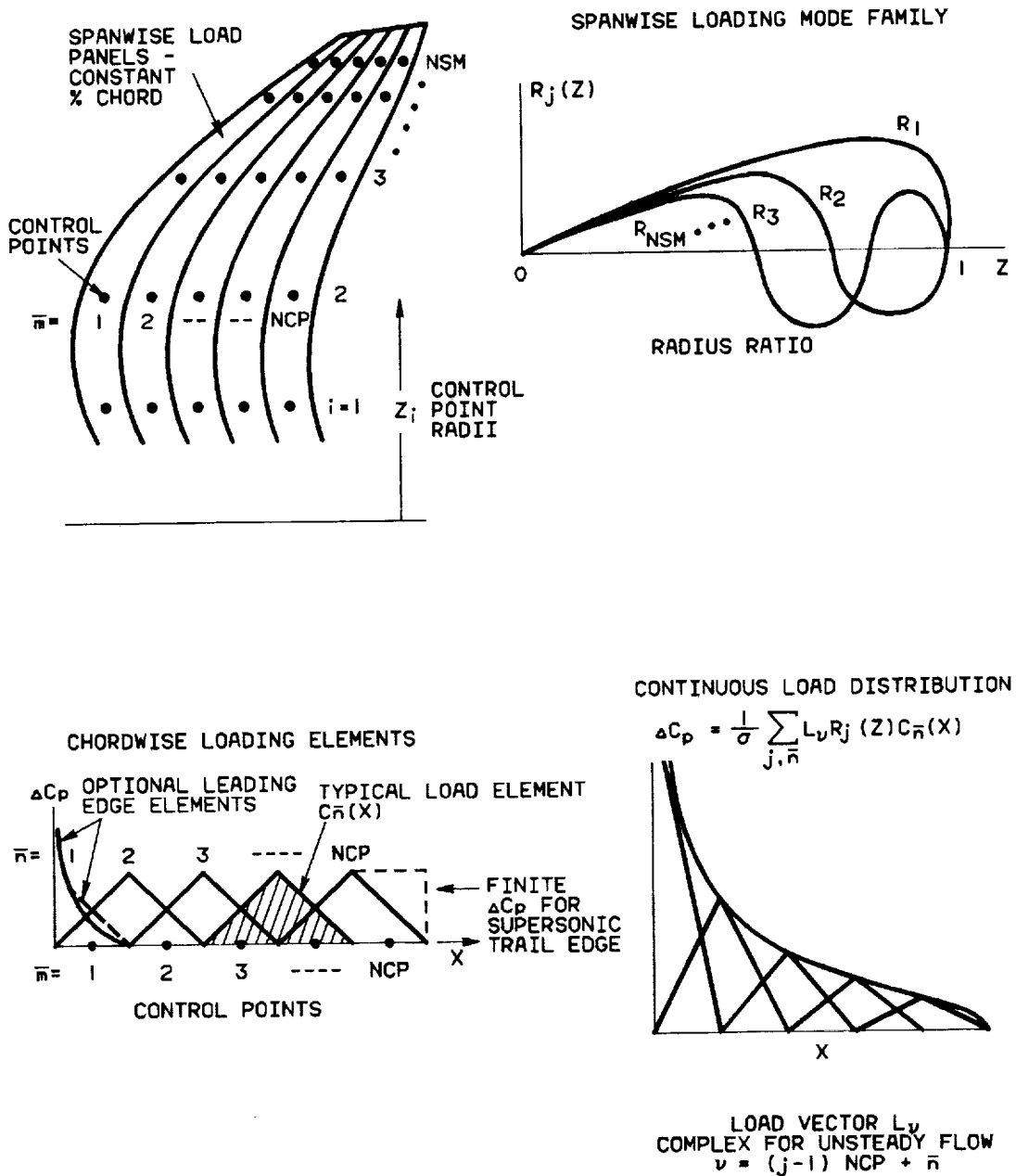


Figure 14. Load paneling system.

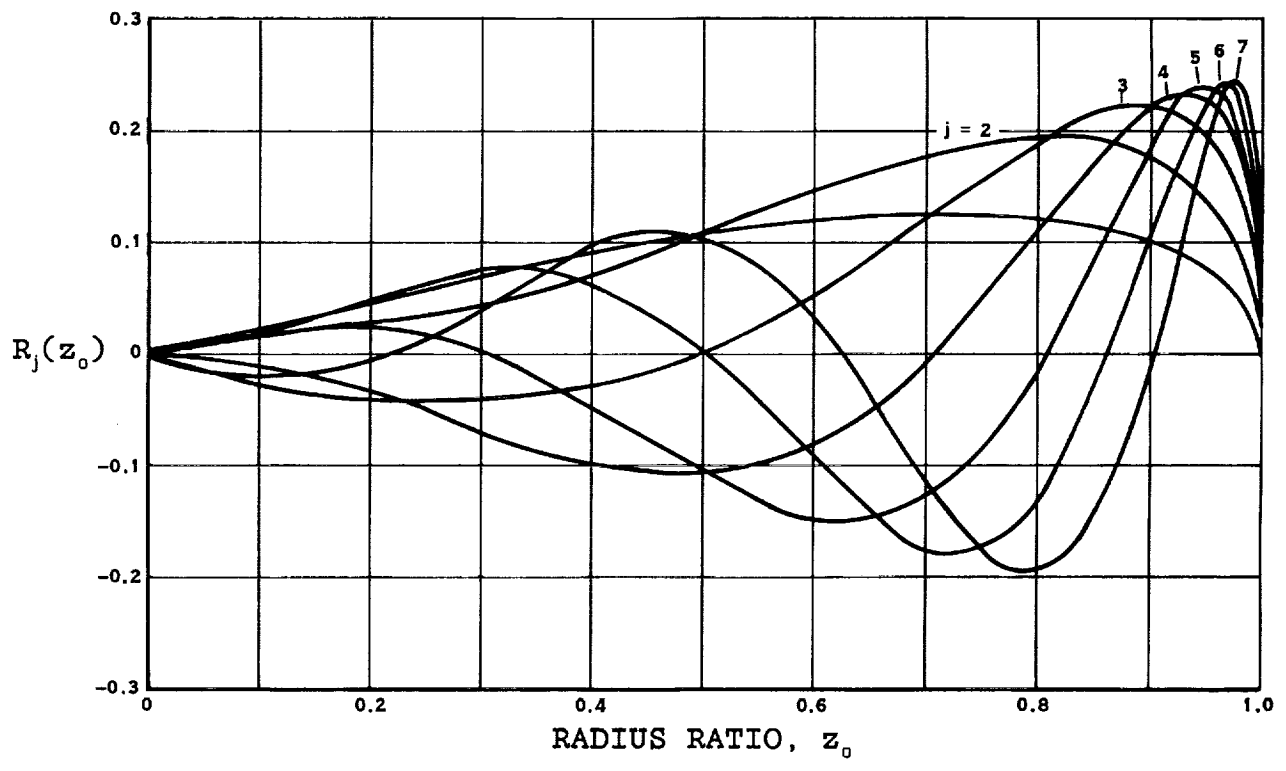


Figure 15. A family of spanwise load distribution functions. $R_j = z_0 \sin[j \cos^{-1}(z_0)]$.

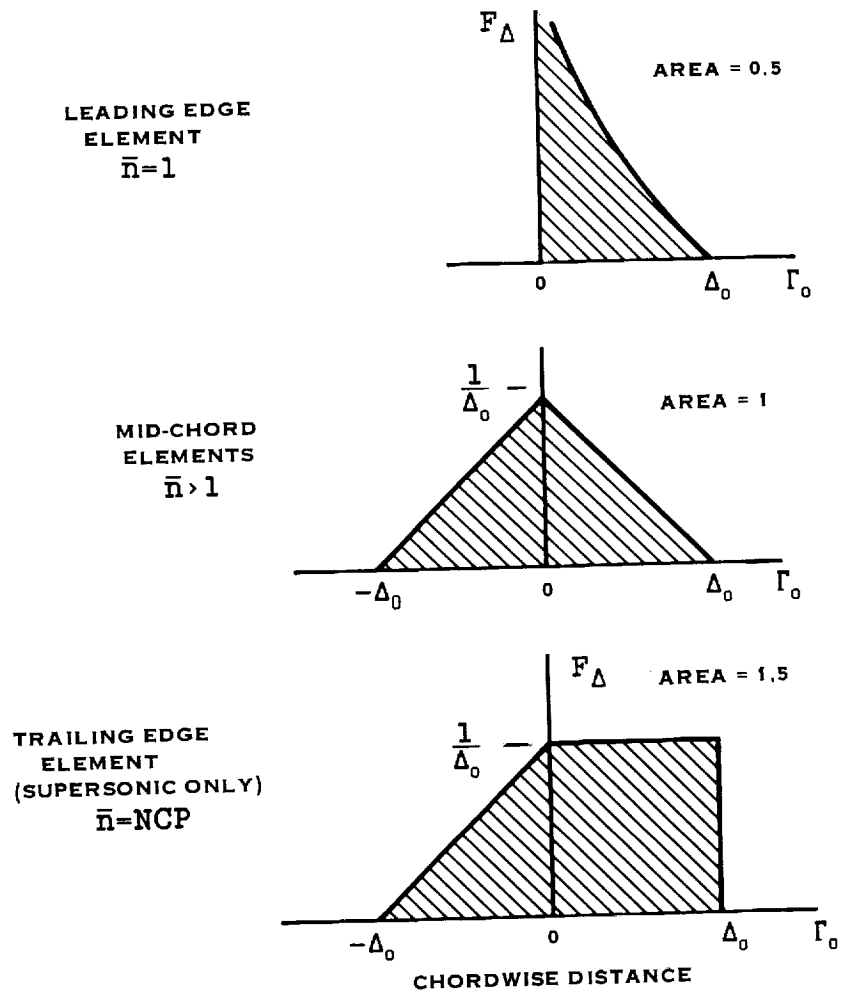


Figure 16. The 3 types of load panel.

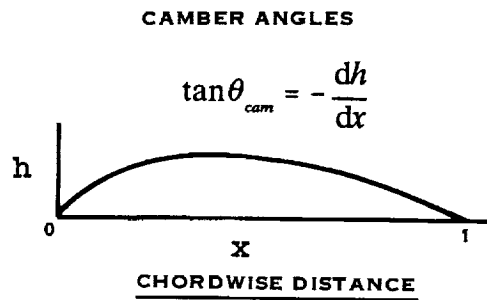
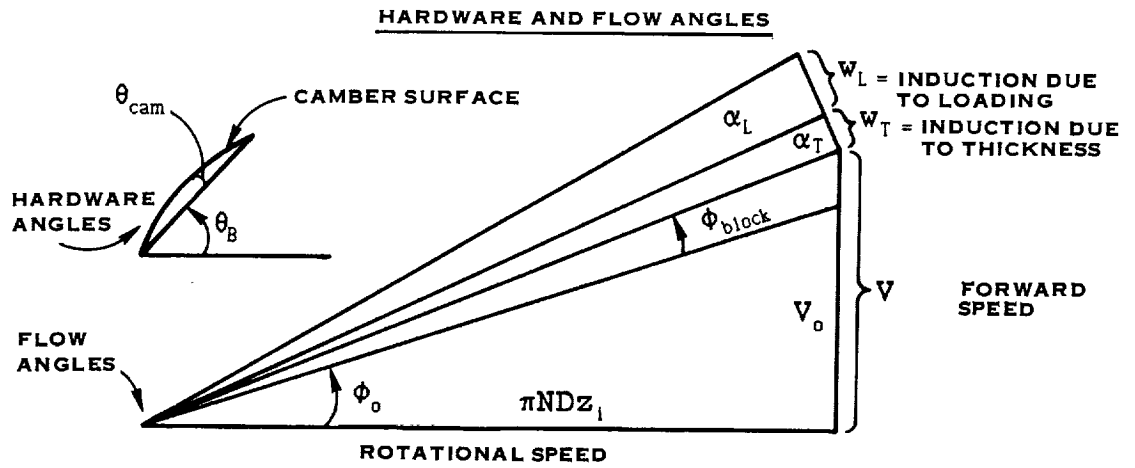


Figure 17. Angles used to define boundary conditions.

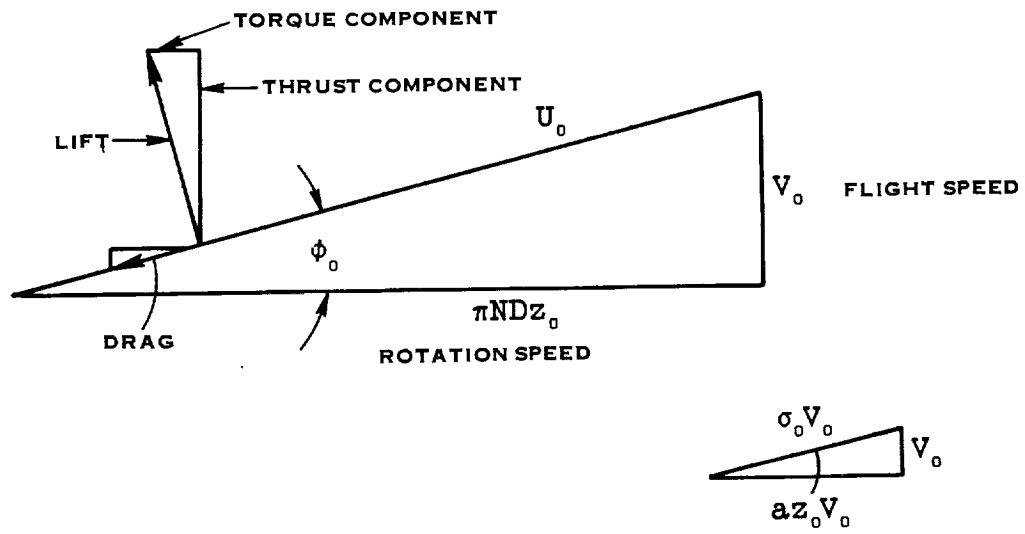


Figure 18. Resolution of forces for calculation of performance.

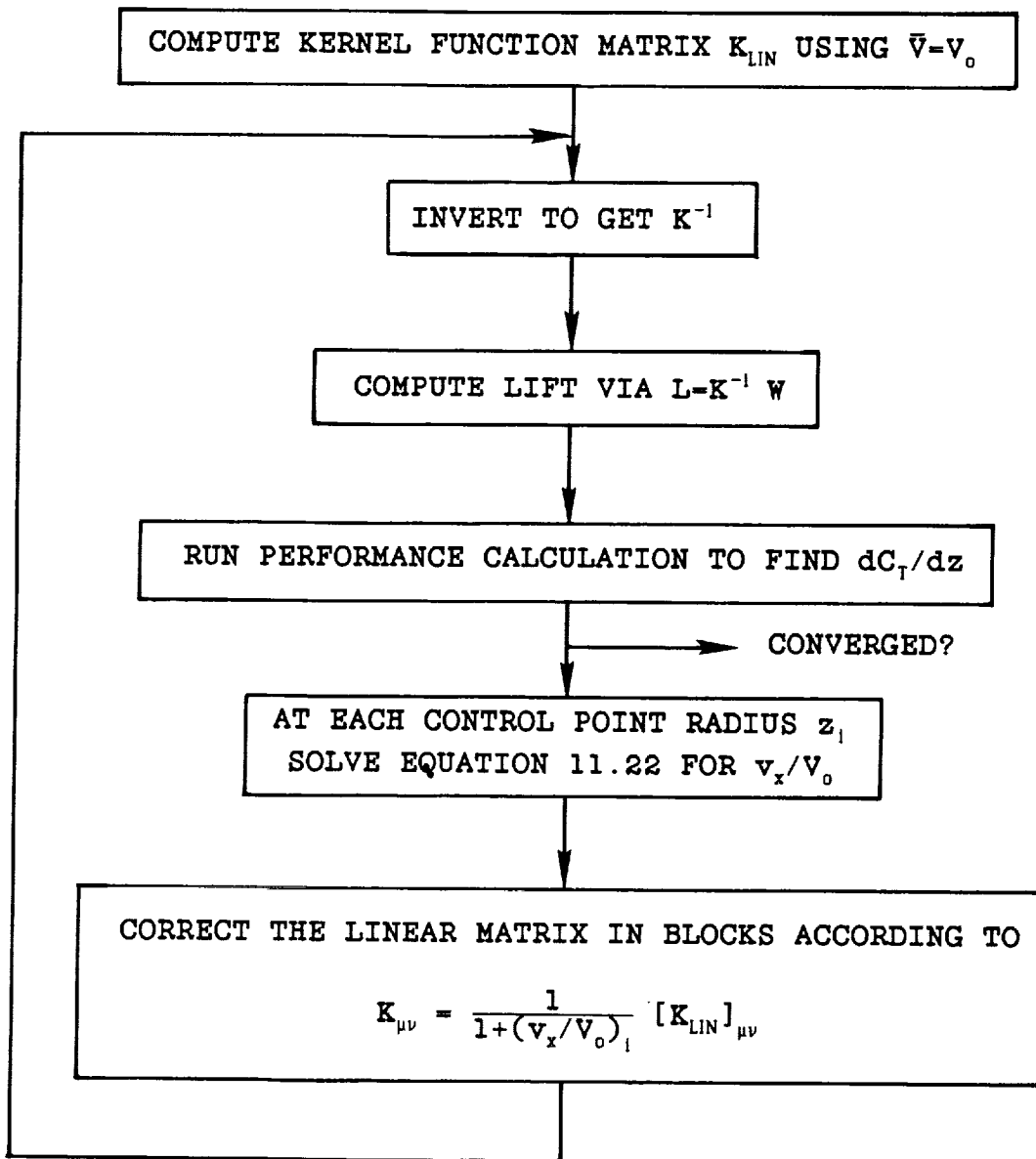
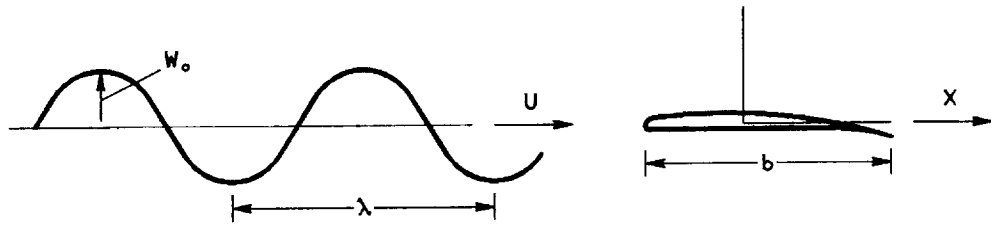


Figure 19. Iteration scheme for non-linearity associated with finite axial induction.



GUST: $W = W_0 e^{i\omega(t-x/U)}$

REDUCED FREQUENCY: $k_0 = \frac{\omega b/2}{U} = \pi \frac{b}{\lambda}$

ANGLE OF ATTACK: $\alpha = W_0/U$

UNSTEADY LIFT COEFFICIENT: $C_L = 2\pi\alpha S(k_0)$

SEARS FUNCTION: $S(k_0)$

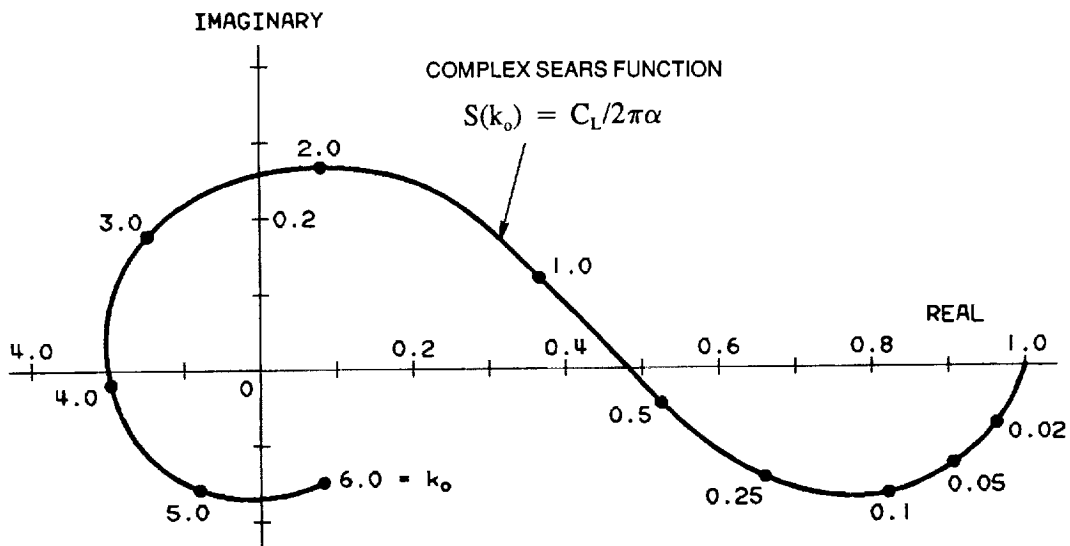


Figure 20. Airfoil/gust interaction problem for Sears Theory. 2D, Incompressible.

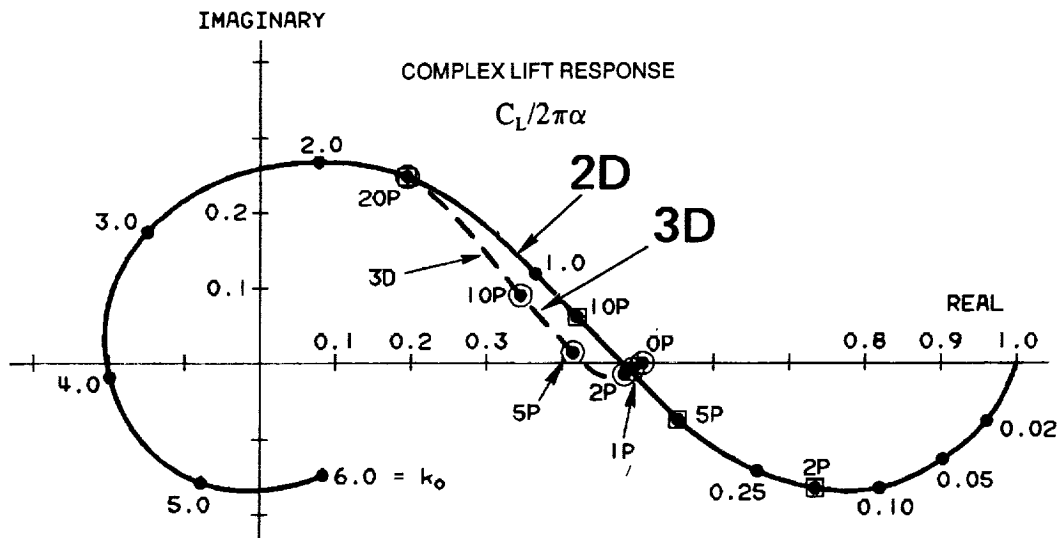
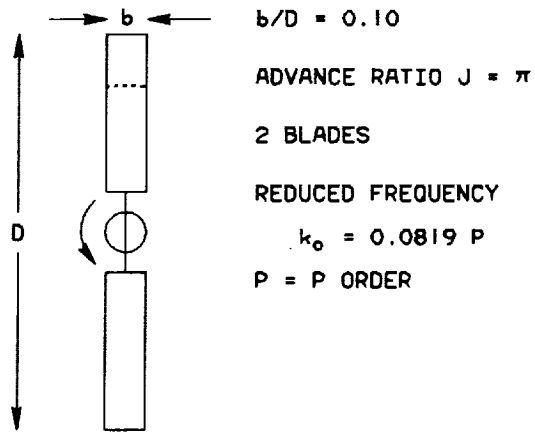


Figure 21. Propeller blade/gust interaction problem for 3D analysis. Incompressible.

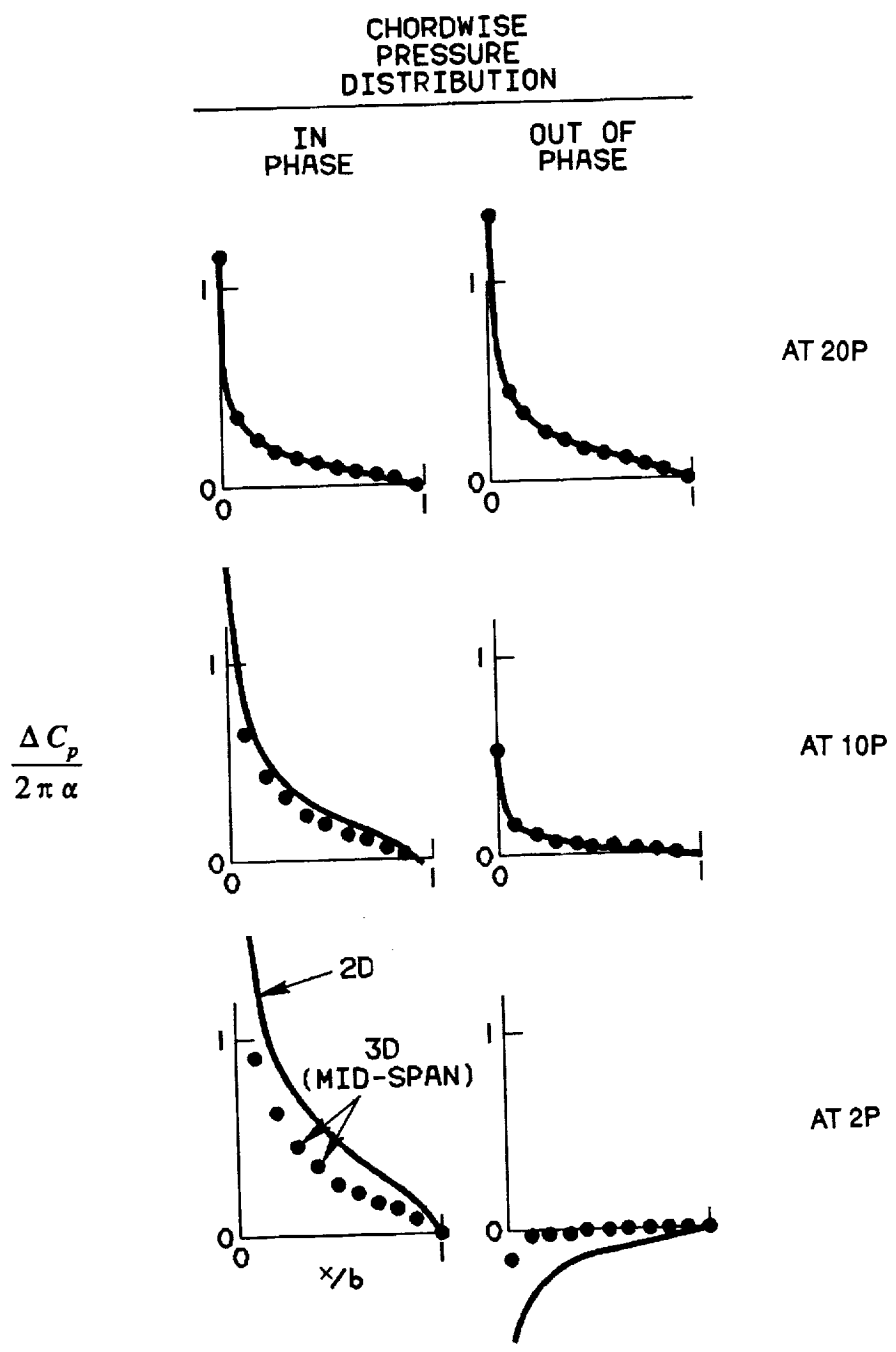


Figure 22. Unsteady pressure coefficients. 3D versus 2D.

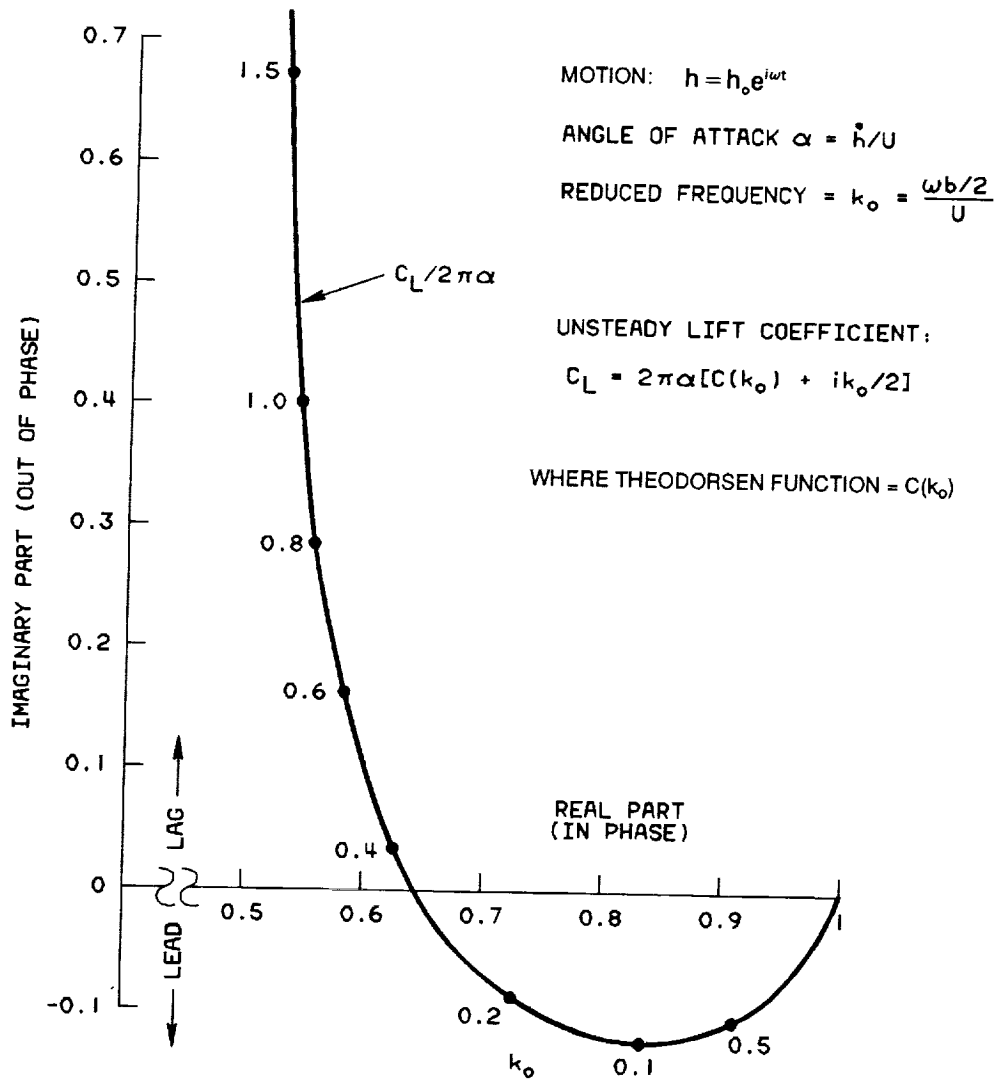
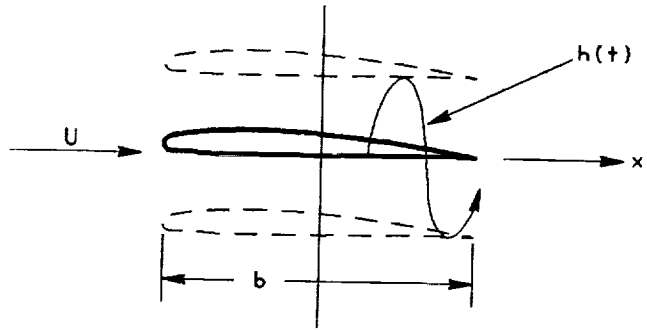


Figure 23. Plunging airfoil problem. 2D, incompressible.

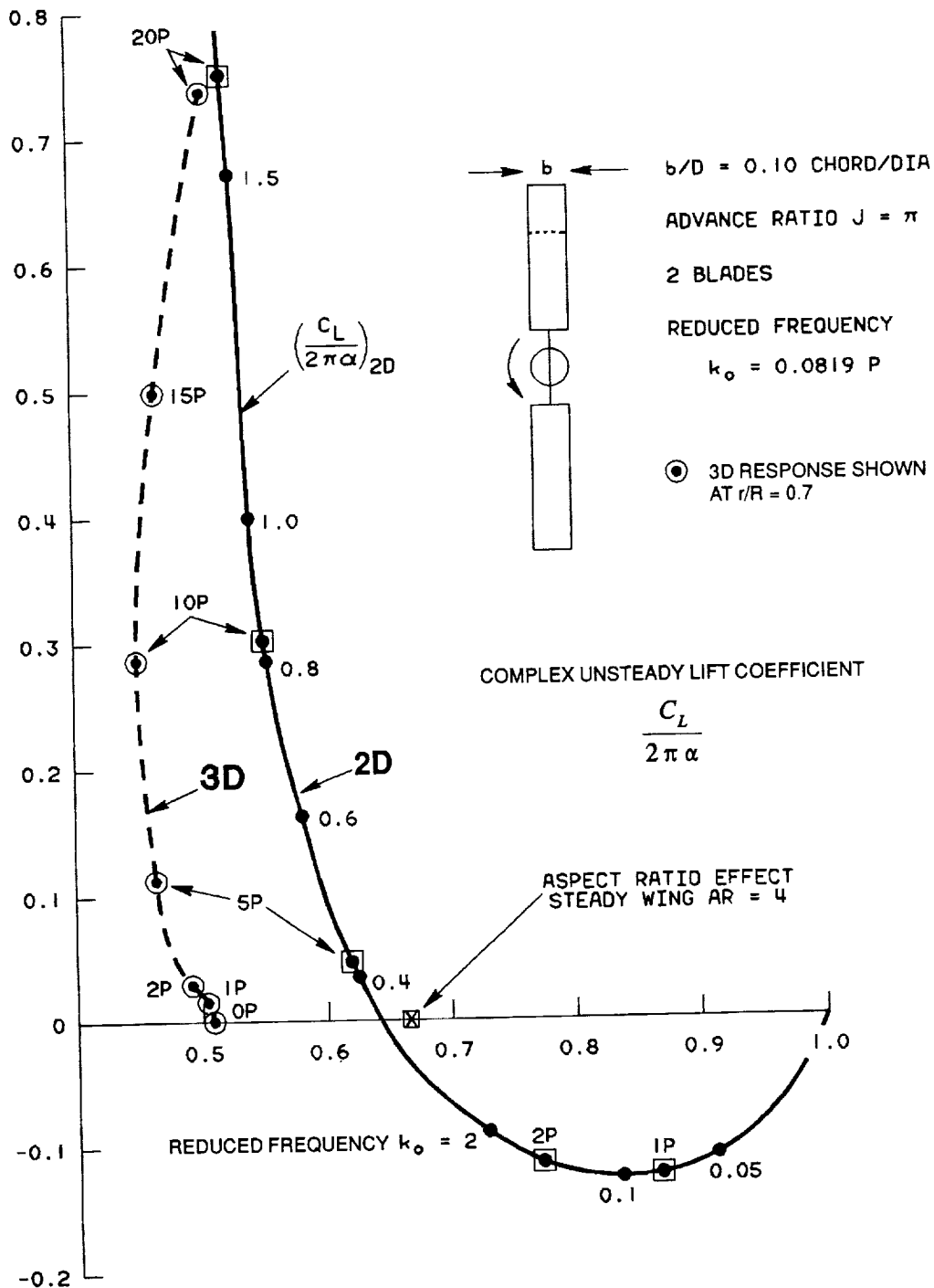


Figure 24. Plunging blade problem. Comparison with 2D theory.

CHORDWISE PRESSURE DISTRIBUTION

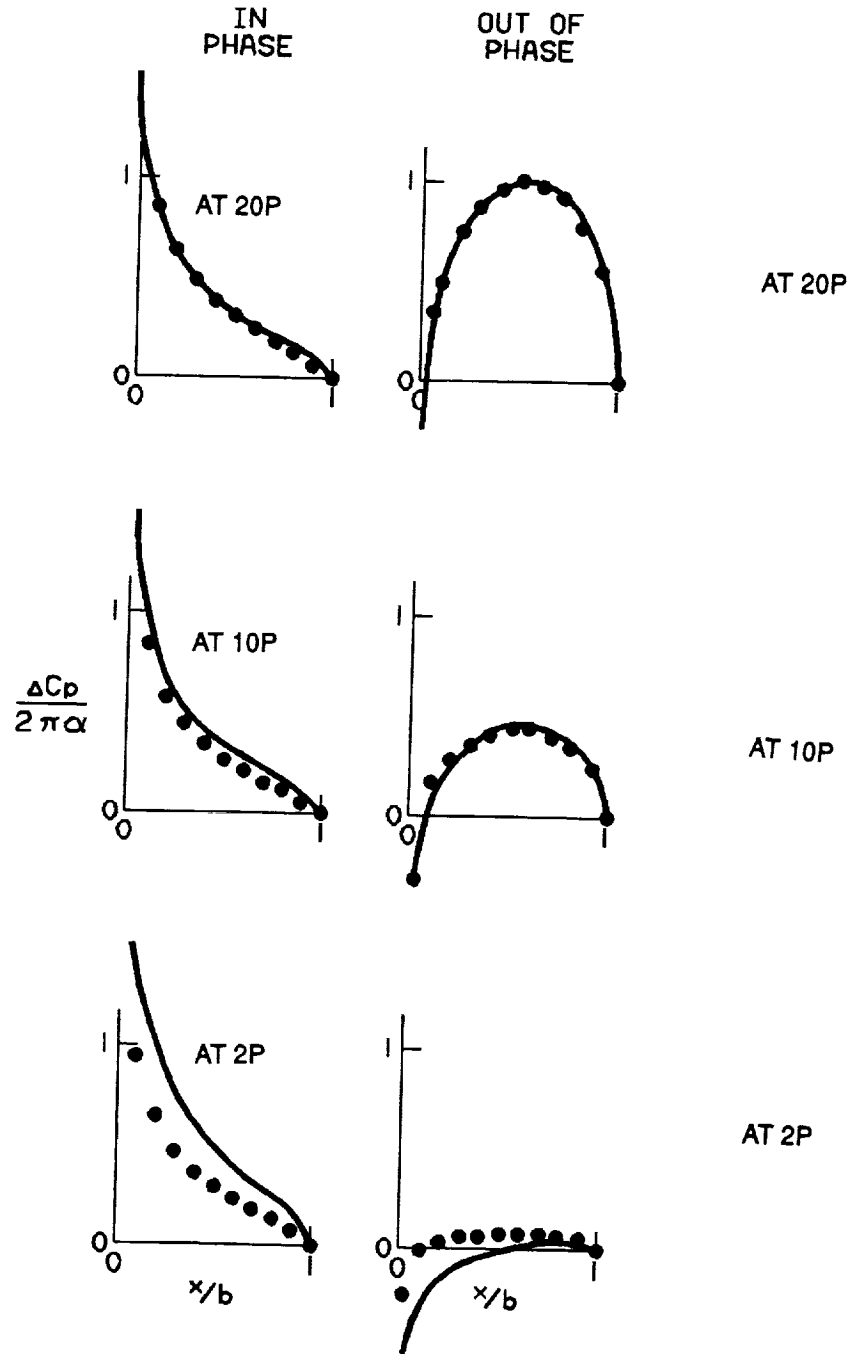


Figure 25. Unsteady pressure coefficients. 2D versus 3D.

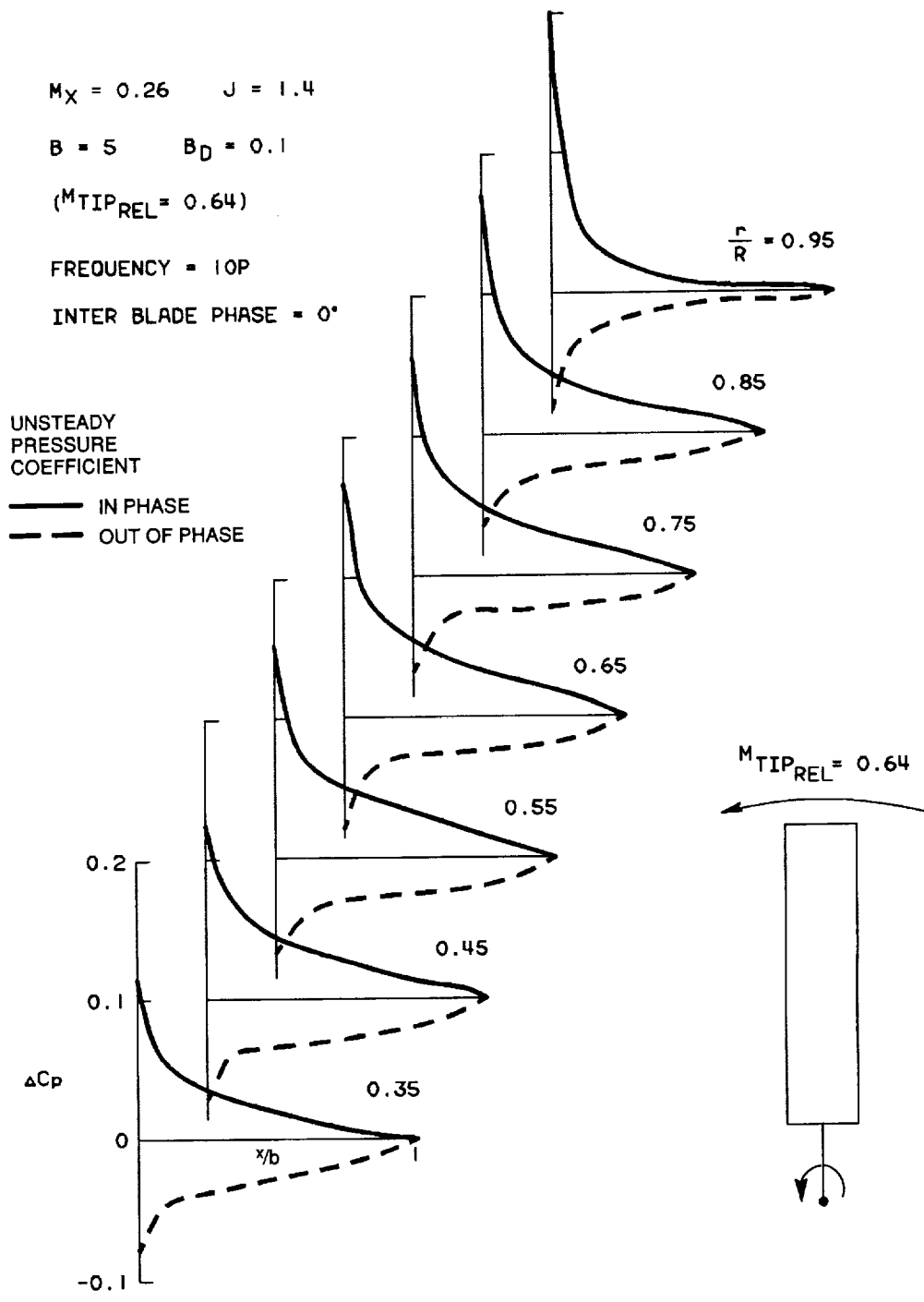


Figure 26. Gust interaction at 10P. Base case with no sweep.

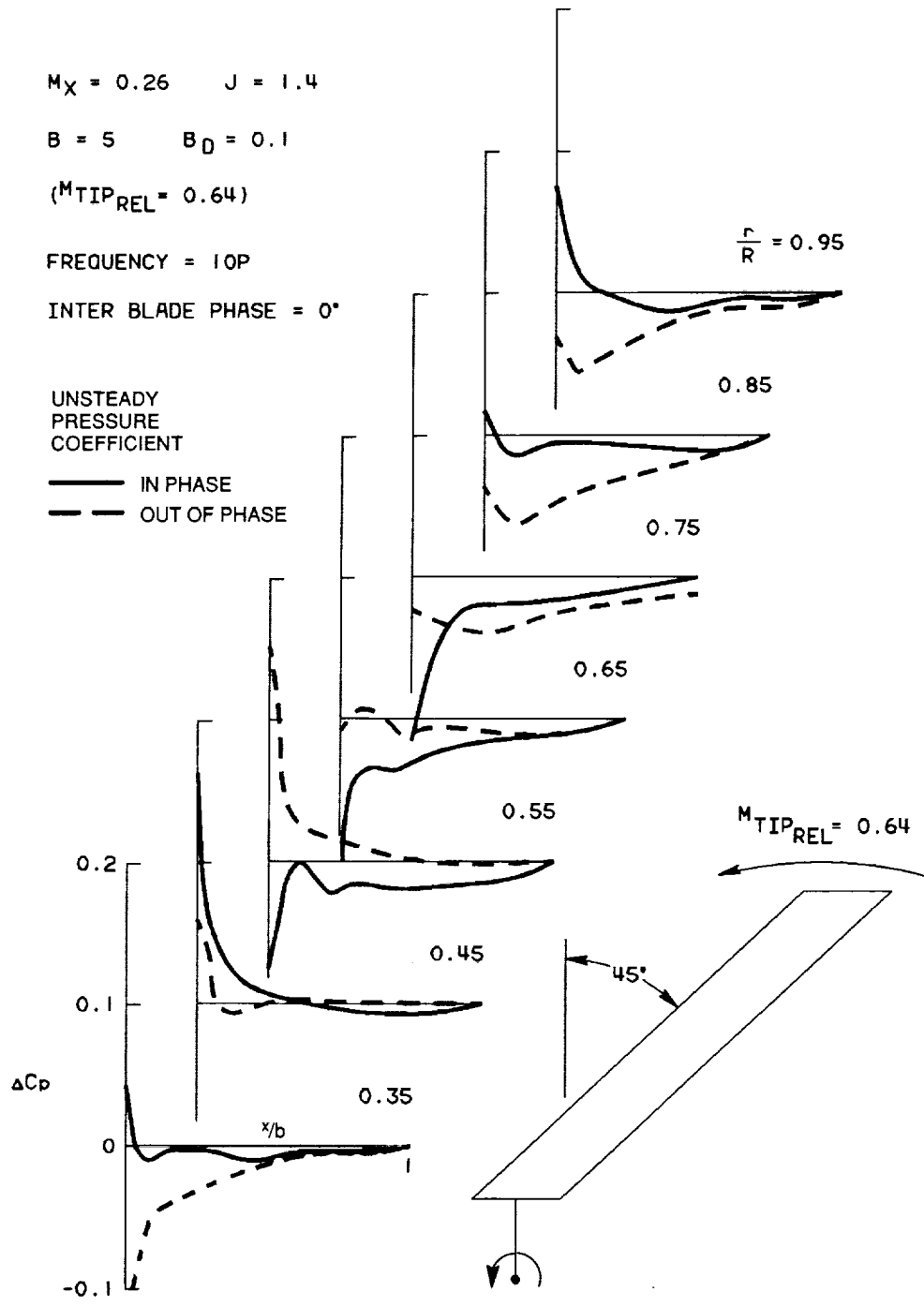


Figure 27. Gust interaction at 10P. 45 degree sweep.

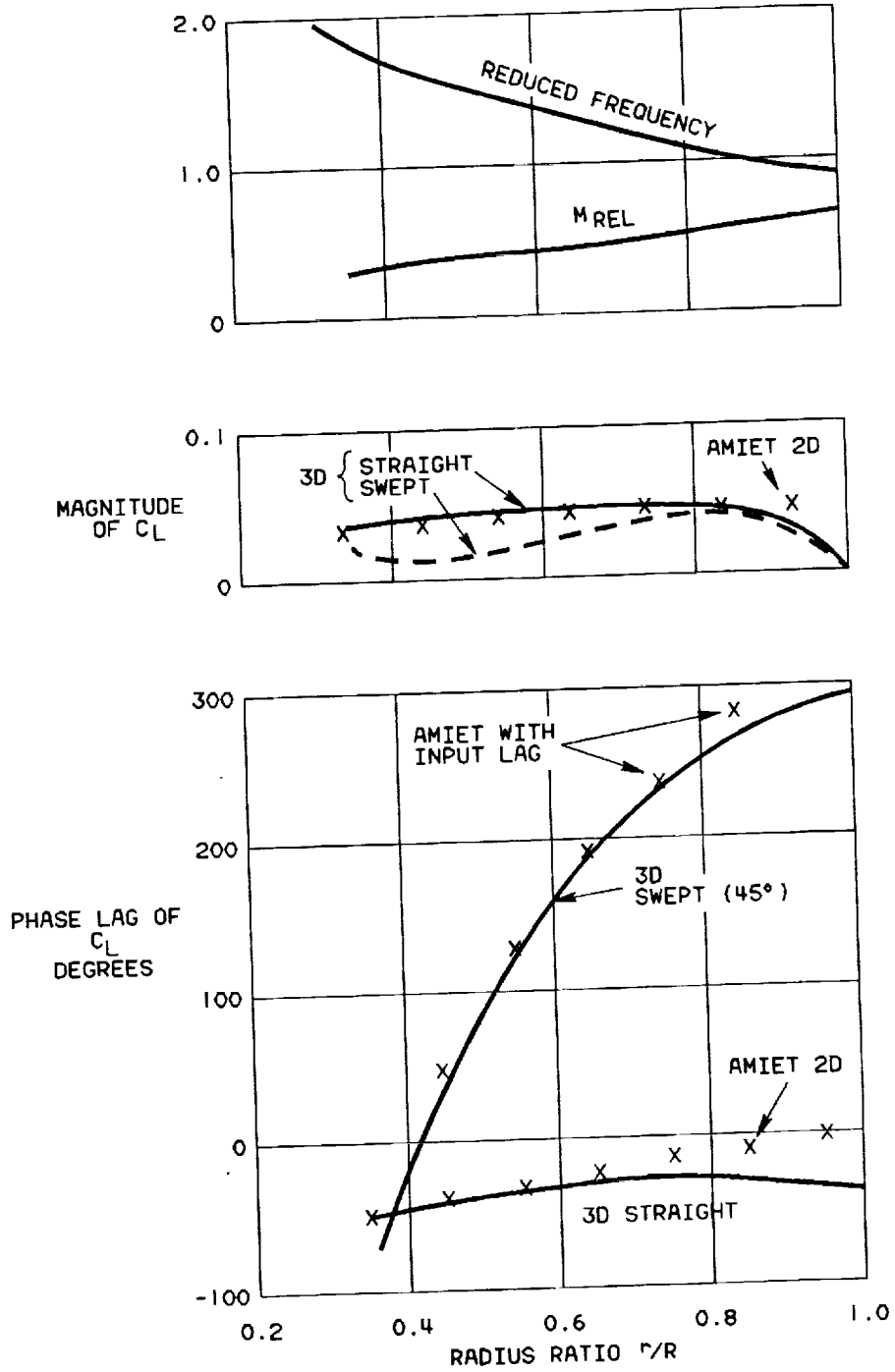


Figure 28. Lift magnitude and phase for previous figures.
 $M_x=0.26$, $J=1.4$, frequency = 10P.

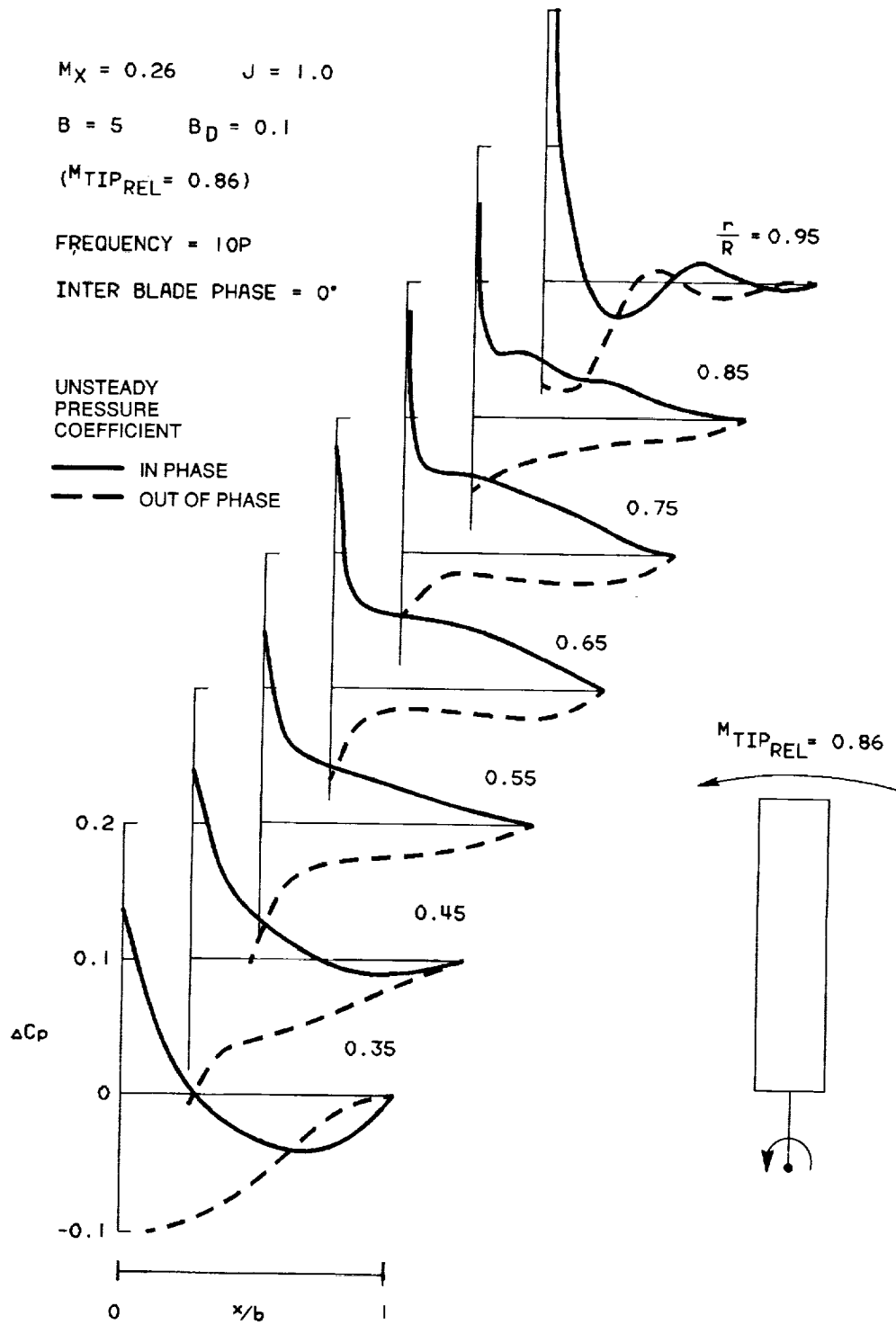


Figure 29. Gust interaction at 10P. Higher Mach number.

1. Report No. NASA CR-4329		2. Government Accession No.		3. Recipient's Catalog No.	
4. Title and Subtitle Unified Aeroacoustics Analysis for High Speed Turboprop Aerodynamics and Noise Volume I--Development of Theory for Blade Loading, Wakes, and Noise				5. Report Date March 1991	
				6. Performing Organization Code	
7. Author(s) D.B. Hanson				8. Performing Organization Report No. None (E-6021)	
				10. Work Unit No. 505-62-4D	
9. Performing Organization Name and Address United Technologies Corporation Hamilton Standard Division P.O. Box 1000 Windsor Locks, Connecticut 06096				11. Contract or Grant No. NAS3-23720	
				13. Type of Report and Period Covered Contractor Report Final	
12. Sponsoring Agency Name and Address National Aeronautics and Space Administration Lewis Research Center Cleveland, Ohio 44135-3191				14. Sponsoring Agency Code	
				15. Supplementary Notes Project Manager, Bruce J. Clark, Propulsion Systems Division, NASA Lewis Research Center, (216) 433-3952.	
16. Abstract <p>This report presents a unified theory for aerodynamics and noise of advanced turboprops. Aerodynamic topics include calculation of performance, blade load distribution, and non-uniform wake flow fields. Blade loading can be steady or unsteady due to fixed distortion, counter-rotating wakes, or blade vibration. The aerodynamic theory is based on the pressure potential method and is therefore basically linear. However, non-linear effects associated with finite axial induction and blade vortex flow are included via approximate methods. Acoustic topics include radiation of noise caused by blade thickness, steady loading (including vortex lift), and unsteady loading. Shielding of the fuselage by its boundary layer and the wing are treated in separate analyses that are compatible but not integrated with the aeroacoustic theory for rotating blades. The report is in 5 volumes with titles and contractor report numbers as follows.</p> <p>Volume I. "Development of Theory for Blade Loading, Wakes, and Noise", (CR-4329) Volume II. "Development of Theory for Wing Shielding", (CR-185192) Volume III. "Application of Theory for Blade Loading, Wakes, Noise, and Wing Shielding", (CR-185193) Volume IV. "Computer User's Manual for UAAP Turboprop Aeroacoustic Code" (CR-185194) Volume V. "Propagation of Propeller Tone Noise Through a Fuselage Boundary Layer", (CR-185195)</p>					
17. Key Words (Suggested by Author(s)) Propfan; High speed turboprop; Aerodynamics; Noise; Blades; Prediction; Acoustic shielding; Vortex lift; Unsteady lift; Wakes			18. Distribution Statement Unclassified - Unlimited Subject Category 02		
19. Security Classif. (of this report) Unclassified		20. Security Classif. (of this page) Unclassified		21. No. of pages 136	22. Price* A07

